2019

High Voltage Insulation Systems for Gas-Cooled Superconducting Power Devices

Aws Habeeb Mohammed Al-Taie

FLORIDA STATE UNIVERSITY

FAMU-FSU COLLEGE OF ENGINEERING

HIGH VOLTAGE INSULATION SYSTEMS FOR GAS-COOLED SUPERCONDUCTING POWER DEVICES

By

AWS AL-TAIE

A Dissertation submitted to the
Department of Electrical and Computer Engineering
in partial fulfillment of the
requirements for the degree of
Doctor of Philosophy

2019

Aws Al-Taie defended this dissertation on June 28, 2019.
The members of the supervisory committee were:

Sastry Pamidi
Professor Directing Dissertation

Juan Ordonez
University Representative

Simon Foo
Committee Member

Lukas Graber
Committee Member

Olugbenga Moses Anubi
Committee Member

The Graduate School has verified and approved the above-named committee members, and certifies that the dissertation has been approved in accordance with university requirements.

To my dear wife *Noora* and beloved kids *Yousif* and *Yarub*.

ACKNOWLEDGMENTS

Firstly, I would like to thank my country for giving me the opportunity to study abroad in one of the most prestigious universities in the United States of America, Florida State University (FSU), and thanks go to the Iraqi Ministry of Higher Education and Scientific Research (MoHESR). I would also like to thank the Bureau of Scholarships and Cultural Affairs for financially supporting my Ph.D. In addition, my appreciation goes for my home university in Iraq, University of Technology (UoT) and the Department of Electrical Engineering, UoT, for nominating me for the scholarship and for supporting me during my Ph.D. study. I would like to thank all the Iraqi Cultural Attachés and Iraqi Cultural Office staff representing MoHESR in the United States of America during the period of my study (2013-2019) for their support.

Second, I express my sincere gratitude to my major advisor, Professor Sastry Pamidi, for the continuous support during my Ph.D. study and related research, for his patience, motivation, and immense knowledge. I have been inspired by him on many different levels, even on personal level. His guidance helped me all the time of research, writing of research papers, and writing this dissertation. He provided me with the high and prestigious level of education that I was dreaming of. I would have never achieved the quality of research work that has been done and I would not finish my Ph.D., without his continuous guidance. I cannot imagine having a better advisor and mentor for my Ph.D. study. Thank you, Professor Pamidi, for everything. I have not met such a wonderful person that helped and supported me ever in my life like you. Thank you for being in my life. I am so thankful and honored to be a member of your research group and to be your student.

I also would like to express my special appreciation and thanks to Dr. Peter Cheetham. He has been a great mentor for me. I would like to thank him for all the help, support and advice that he offered along my Ph.D. journey. I learned a lot from him on theoretical aspects, and I gained even more on the experimental side of my research. I am also grateful for the uncountable things with respect to practical experience that he taught me. It would not have been possible to complete this research without him. I am really thankful that I have him by my side all the time during my research. I am also thankful for him for the wonderful review work for research papers and this dissertation. Thank you, Dr. Cheetham, for everything. I am really honored to work under your supervision and to be a teammate and a friend.

My sincere thanks also go to Dr. Chul Kim for his help and guidance through my research and my Ph.D. study. He has been a valuable reference to me during my work in the laboratory. I learned a lot from him regarding the experimental work, and he taught me how to tackle and solve practical problems. I also would like to thank him for the indispensable experience that I gained from working with him. He has been another great source of knowledge and support throughout my Ph.D. research work. Thank you, Dr. Kim, for everything, including providing answers for all my questions, and I was really honored to work under your supervision.

Special thanks also go to Professor Lukas Graber. He has been to me like a co-advisor for most of the parts in my research work even though he is in another institution. I was fascinated by the fruitful collaboration with his research group at Georgia Institute of Technology. Furthermore, I would like to express my appreciation for him for introducing me to new research areas that I have

not explored before, encouraging my research and helping me to grow as a research scientist. His massive knowledge and deep insight on my research topic have been priceless. I learned a lot from him, from essentials to the tiny details. Thank you, Professor Graber, for everything, and I was really honored to work with a brilliant scientist like yourself.

I would also like to express my gratitude and appreciation to Dr. Chanyeop Park from Georgia Institute of Technology. I am grateful for him for offering and providing help, support and knowledge throughout my research work and Ph.D. study. I would like also to thank him for providing ideas and hardware towards our collaborative research work. In addition, I learned some practical details from him when he came to work on a research project to the Center for Advanced Power System (CAPS). Moreover, I enjoyed and learned from our work together that we published in scientific journals and conference proceedings. Thank you, Dr. Park, for everything, and I was really honored to work with a promising bright scientist as you are and to be your friend.

I also would like to thank Dr. Juan Ordonez, who has been a committee member for my preliminary, prospectus and my dissertation. Thank you, Dr. Ordonez. I was honored to have you in my supervisory committee.

Additionally, I would like to thank Dr. Simon Foo, who has been a committee member for my prospectus and my dissertation, for his great support. Dr. Foo always meets me with his pleasant demeanor, and he always encouraged me. In addition, Dr. Foo was one of the reasons that I joined FSU transferring from University of Central Florida. Thank you, Dr. Foo, for everything, and I was honored to have you in my supervisory committee.

Furthermore, I would like to thank Dr. Olugbenga Moses Anubi, who was a committee member for my dissertation, for his very nice cooperative attitude. Thank you, Dr. Anubi, and I was honored to have you in my supervisory committee.

I would like also to express my special thanks to graduate and undergraduate students in our research group who have helped throughout my research work with preparing and performing experiments.

It is also important to acknowledge the efforts of the CAPS facilities and front office personnel who have helped in procurement and development of the various experiments I have undertaken. Particular thanks need to go to Nancy Rainey and General Gaskin. Special thanks goes to Michael Coleman due to his wonderful help in practical, technical and logistic issues regarding research.

Another sincere appreciation goes to Mr. Jerry Horne at the High-Performance Materials Institute for his great help in cutting different materials that served my experimental research work with the water-jet.

It is also important to acknowledge the efforts of the staff and faculty of Electrical and Computer Engineering Department, FAMU-FSU College of engineering. Accordingly, special thanks goes for Ms. Melissa Jackson for her help and support, guidance and care along my Ph.D. study. Ms. Jackson was another reason for me to join FSU.

I would also like to thank the friends who have overwhelmed me and my family with love and support during my study. Thank you all for being in our life.

Deep appreciation goes for my parents in law, Mr. Jamal Al-Saad and Mrs. Ferial Al-Azzawi, for their unconditional support during the years of my Ph.D. study.

Last but for the most, to my wife Noora, words cannot express how grateful I am to you for all of the sacrifices that you have made on my behalf. Your prayers for me were what sustained me thus far. Thanks for the unlimited love and support that incented me to strive towards my goal. Thanks for taking the burden of the family and kids on your shoulders while I was dedicated to my Ph.D work. You spent many sleepless nights supporting me in the moments when there was no one else to help. Thanks for believing in me and encouraging me for the whole way. I could not have done it without you.

TABLE OF CONTENTS

LIST OF TABLES

LIST OF FIGURES

ABSTRACT

Demand for electrical power is increasing around the globe to keep up with the ever-increasing annual load growth, which in turn requires new power sources to be installed. As a society, there is a greater emphasis for power sources to be environmentally friendly, such as wind and solar. For large-scale wind and solar power sources, electric utilities need to install them in the optimal regions which are generally far away from the load centers. Hence, efficient and high capacity power transmission solutions are required to integrate these energy sources into the power grid. Another new trend of electrifying the transportation sector with electric ships and aircrafts requires compact electric power devices with high volumetric and gravimetric power densities. Therefore, electric utilities and the transportation sector have been exploring innovative solutions for energy efficient and high-power density technology options, which include utilizing superconducting power devices. High temperature superconducting (HTS) power cables and other devices have been developed and installed in several countries around the world to achieve more efficient and significantly compact devices compared to their copper counterparts. A long-term vision for the future power transmission is a cross-country multi-terminal DC HTS cable transmission system.

Gas-cooled HTS power cables are being explored for electric transportation applications, including aircrafts and ships, due to asphyxiation risks associated with liquid nitrogen. Use of a gas as the cryogen instead of a liquid, however, poses technical challenges resulting from the reduced heat capacity and lower dielectric strength which could affect the overall performance of HTS cables.

When helium gas is used as the cryogen in HTS power devices, the electrical insulation method and materials utilized for liquid nitrogen cooled HTS cables are not applicable. For liquid nitrogen cooled HTS power cables for electric utility applications, lapped tape insulation has been used to achieve operating voltages in excess of 100 kV. When this same design is utilized for electrical insulation system of helium gas cooled HTS cables, partial discharge (PD) occurs at voltages <10 kV, limiting the operational voltages. The butt gaps within the lapped tape insulation layers trap helium gas and cause the associated field enhancements leading to low partial discharge inception voltages.

The research described in this dissertation focused on extending the understanding the technology challenges associated with the use of gas media as part of the electrical insulation system at cryogenic temperatures. The emphasis was on the development of the concept of superconducting

gas insulated line (S-GIL) as an alternative to lapped tape electrical insulation system to HTS power cables to enable higher operating voltages for helium gas cooled HTS power cables. The S-GIL, which is similar to the Gas Insulated Line (GIL), was conceptualized recently at Florida State University's Center for Advanced Power Systems (FSU-CAPS). The S-GIL utilizes the flow of pressurized cryogenic gas instead of stagnant room temperature gas for GIL. The S-GIL addresses the challenge of low partial discharge inception voltages (PDIV) in lapped tape insulated, gas cooled HTS cables by eliminating the need for solid insulation layers on the cable. However, the need to maintain the cable on the axis of the cryostat imposes the requirement of insulator spacers. This work explored bundled tubular spacers for S-GIL as an option for spacers and 1-m long prototype cables were fabricated and characterized in gaseous helium and helium-based gas mixtures. Surface flashover along the surface of the spacers is expected to be one of the design factors which influences the voltage rating for S-GIL. The designs considered different tube materials and gases and a variety of experiments were conducted at room temperature and at cryogenic temperatures to gain a thorough understanding of the S-GIL design limitations.

To gain further understanding of the limits of the S-GIL concept, the design was tested with liquid nitrogen as the insulation medium to decipher the role of the intrinsic dielectric strength of the insulation medium. Besides providing additional insights into S-GIL concept, the liquid cooled alternative will have applications in terrestrial power systems and transportation sector where higher operating voltages and efficient thermal designs are needed.

The research also focused on investigating the surface flashover phenomenon in GHe environment. This included investigating the triple point where the conductor, solid insulation material, and gas insulation media meet. Surface flashover measurements were performed with varying gas density, temperature, gas composition, solid insulation material, applied voltage waveform, and electric field strength and distribution.

CHAPTER 1

INTRODUCTION

The research undertaken for this dissertation is aimed at understanding and advancing the electrical insulation materials and system designs for gas cooled superconducting electrical power devices. Currently, the lack of choice of electrical insulation materials and designs compatible with the cryogenic operational environment of superconducting technology is one of the limitations for the development of superconducting power devices. Effective electrical insulation systems are essential for the resilience of superconducting power devices. The development of electrical insulation systems is particularly difficult for gas cooled superconducting systems because of the weak dielectric strength of gases.

The appeal of superconducting technology is the ability of superconductors to carry significantly higher current than conventional conductors and with zero resistance, which allows for significantly higher power density and higher efficiency [1]. Higher current densities in superconducting devices allow their operation at lower voltages than conventional technology to achieve the same power density. There is the potential for superconducting devices to be incorporated into several applications which will be discussed in greater detail in Section 1.1 and 1.2.

For a superconductor to carry high current, it must operate within its superconducting region. The basic principles of superconductivity and their relationships for electrical power devices will be discussed in Section 1.3. One of the boundaries of the superconducting region is critical temperature, and for all superconductors that currently exist, this temperature is in the cryogenic temperature range. The required cryogenic operating temperature of superconductors poses two distinct challenges. Firstly, there is limited choice of cryogens which are capable of providing these temperatures. Secondly, the electrical insulation materials and designs must be compatible to cryogenic conditions. Both these aspects will be discussed in in Section 1.5.

Currently, superconducting technology is being developed for operating from low voltages to high voltages up to several hundred kV, depending on the application. The voltage rating of a power device influences the designs significantly. This includes the steady-state conditions as well as the associated transient conditions the superconducting power device will be exposed to. The expected lifetime of power devices is typically > 30 years and during this time the electrical

insulation system will be subjected to electrical, thermal, and mechanical stresses. Section 1.4 provides an overview of the properties of interest for electrical insulation systems and the methods used for selection of insulation materials and optimization of system designs.

From the literature review in Sections 1.1-1.5, focus areas for this research have been identified. Section 1.6 provides an overview of the research undertaken for this dissertation.

1.1 Current Status and Future Directions of Electrical Power Networks

Electrical power networks exist in different sizes from micro grids to large power grids. Currently, power grids are facing many challenges including the need for providing a cost-effective solution to efficiently match the ever-changing load demands with the generation. There is also the need to accommodate the integration of renewable and distributed energy sources into the grid [2].

One of the methods to develop a more efficient power grid is to reduce the losses within the system. Transmission and distribution (T&D) losses represent a significant portion of the total generated energy. Table 1 shows the amount of the generation, retail sales (in MWh), and the percentage and cost of the T&D losses in the power grid of the United States. The efficiency of the transmission and distribution in the grid is approximately 92%, according to the Energy Information Administration (EIA) [3]. Higher efficiency levels cannot be achieved with the conventional technology. Thus, the power sector is looking for new and innovative solutions to improve the T&D losses. Superconducting technology provides a solution as it is able to distribute power with significantly reduced losses. For superconducting technology, the inefficiency is a result of the required cryogenic system. It is expected that the losses from the cryogenic system will be lower than the T&D losses experienced today by the electrical power grid. The use of superconductors within the power grid could also reduce the number of transformers required in the T&D systems which also adds to the overall savings in the system [2]. The incorporation of superconducting power cables into the power grid and potential configuration changes to the power grid to allow for greater efficiencies to be achieved will be discussed in Chapter 2.

Annual load growth is another challenge that the electric utility sector is facing. The continuous annual load growth around the globe has been motivating the power sector to look for new and innovative solutions to meet the increasing load demands. The projected load growth in the United States is approximately 20% between 2017 to 2035 [4]. The load growth is a

conservative estimate and a greater penetration of electric transportation may result in even higher load demands. It is also of importance to see where this load growth is expected to occur. Majority of the growth is expected to occur in already developed urban areas which will strain the existing electric power infrastructure. The existing infrastructure is not capable of supporting the expected increase in load demands resulting in "urban power bottlenecks." In some urban areas, it may not be easy to install new infrastructure due to space, easement, and siting restrictions. Therefore, replacing the existing technology with new technologies with higher power density is a potential solution. Superconducting power cables are a potential solution as they offer power densities in excess of 5 times of conventional technology [1].

Table 1: T & D losses percentage of the total net energy generation and the financial loss for the years (2012 -2014), depending on the data from EIA [3]

Year	Average Retail Price (Cents/kWh)	Net Generation (MWh)	Total Retail Sales (MWh)	T & D Losses (% of Total)	T & D Losses (Billion Dollars)
2014	10.44	4,093,606,005	3,764,700,267	8.0346	34.338
2013	10.1	4,065,964,067	3,725,063,721	8.3842	34.431
2012	9.84	4,047,765,259	3,694,649,786	8.7237	34.747

Another challenge that the electric utility sector is facing is the societal and governmental pressure to generate electricity from renewable energy sources. Society's concerns for global warming, climate change, and depletion of the planet's natural fossil fuel reserves have led to the trend of incorporating more renewable energy sources into the power grid. The current trend of relying on renewables is followed by many countries around the globe, and the published literature predicts that renewable energies alone, with sufficient energy storage, will be able to supply the world energy demand by 2030 [5]. Thus, increasing the power transmission capacity is another necessity for the utilities.

Increasing electrification of transportation (electric trains, ships, aircraft) poses another challenge for the power grid. Transportation electrification trend has come along with considerations to the climate and resources depletion [6]. Airbus Group, NASA, US Navy and

other commercial transportation companies have been considering superconducting power cables, motors, and generators in the power systems [7]–[10].

1.2 Superconducting Technology Solutions for Various Power Applications

Superconducting technology offers solutions for most of the challenges previously listed. Higher efficiency can be achieved using superconducting power cables since they eliminate the resistivity loss, which is the main source of losses. On the other hand, much higher current levels in superconducting cables eliminate the need for some voltage level conversions, which is the second source of losses and additionally reduces footprint of the power system in urban areas [11], [12]. Accordingly, as shown in Figure 1, the challenges of load growth and the urban power bottlenecks can be addressed with superconducting cables. Other benefits of superconducting technology are low thermal and electromagnetic interference to the environment, and underground HTS cable installations address the vulnerability of power grid to hurricanes and natural disasters. Furthermore, with the higher power density, compared to the conventional conductor technology, superconducting technology provides solutions for enabling integration of the renewable energy sources and improving system stability [13].

Superconducting technology offers solutions for the required high-power density for transportation sector as superconducting devices are lighter and smaller than equivalently rated conventional devices. Superconducting machines possess higher torque density (up to three times that of conventional machines) and meet the requirements for commercial and the US Navy ships [10]. In addition, the Navy has been considering several superconducting power components including superconducting cables to support the medium voltage DC (MVDC) bus for 100 MW warships instead of the conventional cross-linked polyethylene (XLPE) cables [9]. The Navy has developed superconducting degaussing systems with 75% lower overall system weight compared to conventional copper cables [14], [15], as shown in Figure 2.

For aviation applications, National Aeronautics and Space Administration (NASA) has been considering superconducting technology and is developing N3-X experimental all-electric aircraft. The N3-X is exploiting weight reduction using all superconducting power components [8]. Figure 3 shows the unique design of the N3-X aircraft [16]. The weight and space savings, by utilizing superconducting devices, enable the optimal location for generators and motors which results in a more aerodynamically efficient design and in turn fuel savings. Airbus Group is investigating a high

temperature superconducting (HTS) Roebel cable to support future fully-electric aircrafts with power ratings of few MW to few tens of MW [7]. The megawatt-range superconducting power cables allow decreasing fuel consumption due to the lightweight with their high current-carrying capacity to meet the low voltage limitations. Thus, superconducting cables are the key enabling technology for the fully-electric aviation applications.

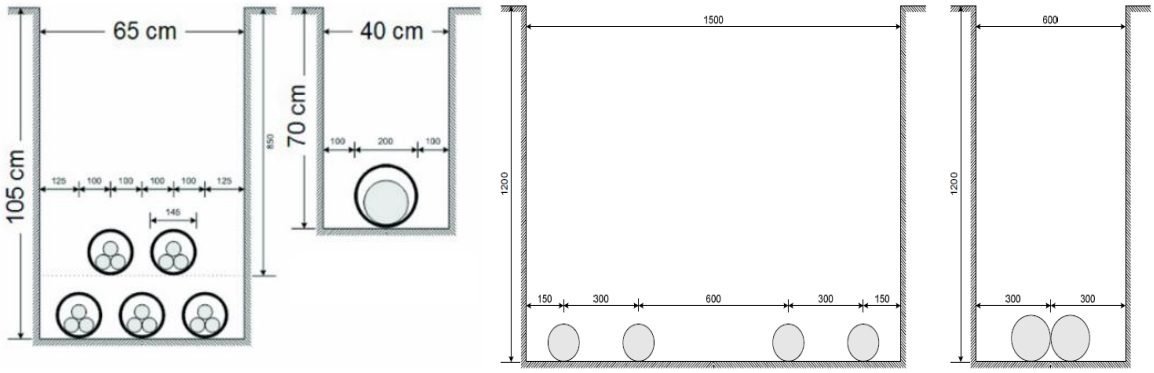

(a) (b)

Figure 1: For the same amount of the transmitted power capacity (a) the required space for conventional 3-phase AC cables (left) compared to the superconducting cable (right) [11] (b) the required space for conventional DC cables (left) compared to superconducting DC cables (right) [12]

Electric power systems require fault tolerant solutions. With properly designed fault current limiting (FCL) superconducting cables, electrical faults can be handled effectively. The FCL cable technology was already developed for the power grid to increase stability and power system protection [2].

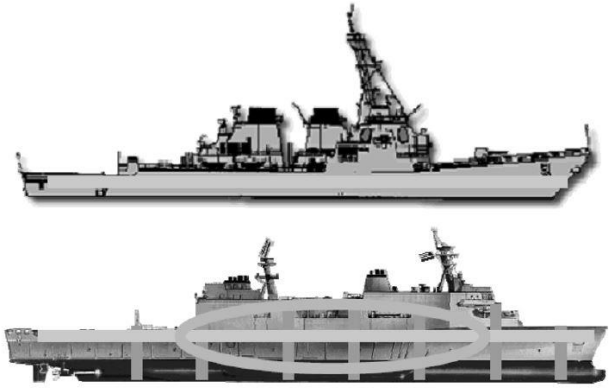

Figure 2: (Top) 2-axis degaussing cable running horizontally (bottom) 3-axis degaussing cable running horizontally and vertically [15]

Figure 3: NASA conceptual design for the N3-X aircraft [16]

1.3 Electrical Characteristics of Superconducting Materials Useful for Electric Power Devices

The phenomenon of superconductivity was discovered in mercury by the Dutch physicist, Heike Kamerlingh Onnes in 1911 [17]. Superconducting materials must operate within a domain, called critical surface [1], bounded by the three critical parameters, critical temperature (T_c), critical current density (J_c) and critical magnetic field (H_c), as shown in Figure 4. Outside the critical surface, the material returns to its normal state with high resistance. Onnes recognized the benefit of lossless electrical current transmission in superconductors and proposed a superconducting DC current connection between London and Paris [18]. However, these hopes were smashed with the disappearance of the superconductivity when carrying more than few amperes or in the presence of even a weak magnetic field. The first superconducting materials discovered fall into the category of Type I, and they do not allow the magnetic field to penetrate the bulk of the superconductor because of the Meissner effect [19]. The Type I materials are not useful for electric power applications. In 1930s, Type II superconductors were discovered, which allow partial penetration of the magnetic flux and tolerate much higher current and magnetic field than Type I, as shown in Figure 5. Practical Type II superconductors were discovered in the 1950s and early 1960s through the arrival of the intermetallic compounds and alloys, especially the A15 compounds [20].

Based on the critical temperature, superconductors are classified into two main categories. Low temperature superconductors (LTS) such as niobium-titanium (NbTi) and niobium-tin (Nb_3Sn), and high temperature superconductors (HTS), such as bismuth-strontium-calcium-copper-oxide (BSCCO) and rare earth-barium-copper-oxide (REBCO). Besides these two

categories, another superconductor that falls in between the two categories due its critical temperature, is magnesium diboride (MgB_2) [2], [21]. Table 2 summarizes the superconductors that are useful for practical power devices.

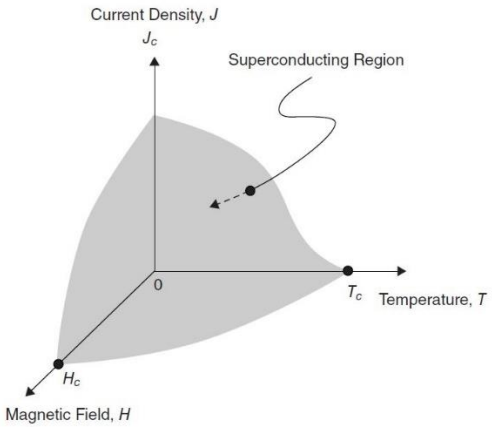

Figure 4: Superconductivity critical surface [1]

HTS technology offers 3 to 5 times greater power densities than the conventional technology [1]. Superconducting devices typically operate at temperatures lower than their respective critical temperatures listed in Table 2 since the critical current is inversely proportional to the operating temperature. For instance, at a fixed magnetic field, the critical current of a HTS material increases up to 3 to 4 times when the operating temperature is lowered from 77 K to 50 K [22], as shown in Figure 6.

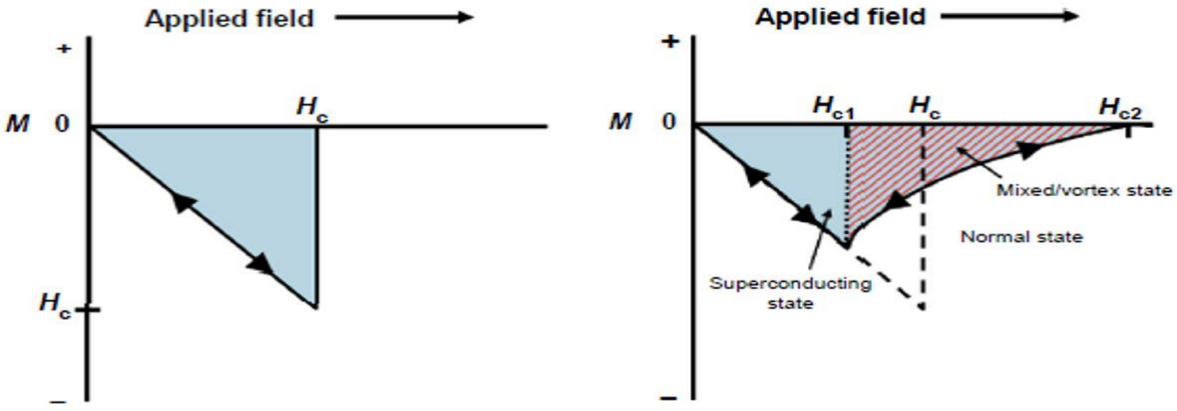

Figure 5: Typical M versus H curve for (a) Type I superconductor, (formerly called “Soft” superconductors) (b) Type II superconductor (formerly called “Hard” superconductors) [2]

Table 2: Superconductors that are useful for practical power devices [2]

Superconductor	**Critical temperature(K)**
Nb	9.5
NbTi	9.5
Nb_3Sn	18.3
Nb_3Al	18.8
MgB_2	39
$REBa_2Cu_3O_7$ (REBCO)	93
$Bi_2Sr_2Ca_1Cu_2O_8$ (Bi-2212)	85
$Bi_2Sr_2Ca_2Cu_3O_{10}$ (Bi-2223)	108-110

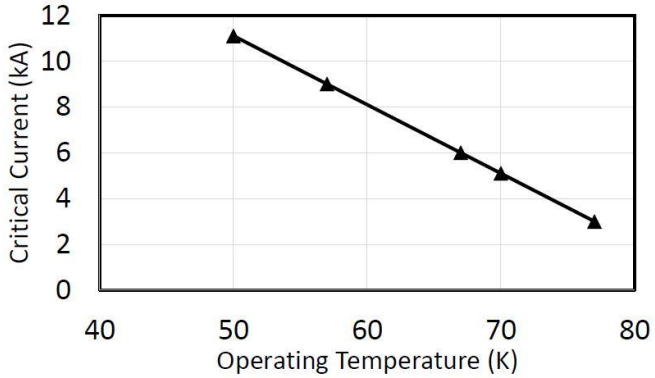

Figure 6: Critical current vs temperature for gaseous helium cooled typical SC cable [22]

1.4 High Voltage Engineering Studies for Insulation Systems

In the development of power dense electrical devices, it is necessary to optimize the electrical insulation designs. If the electrical insulation system is overrated, it can result in additional weight and size being added to the power device. If the electrical insulation system is underrated, then it can lead to an in-service failure. To optimize the electrical insulation design, it is necessary to understand the electrical, thermal, and mechanical stresses, which the electrical device will be exposed to during the normal operation and how they affect the electrical insulation of the device. This requires complete knowledge of the electric stresses, controlling methods, besides understanding the dielectric properties of the insulation material for the electric field type, AC or DC [23]. In the following subsections, dielectric properties of the materials including permittivity, conductivity and dielectric strength are discussed.

1.4.1 Dielectric Properties of Insulating Materials Related to Electric Field Type

The density of the current ($\vec{J}$) in the material consists of two parts. First part is the conduction current density ($\vec{J}_C$), and the second part is the displacement current density ($\vec{J}_D$), as shown in the equation:

$$\vec{J} = \vec{J}_C + \vec{J}_D \tag{1}$$

The conduction current density is related to the conduction electric filed, and it represents the current density of the free charges in the material. The displacement current is related to the displacement field ($\vec{D}$), which correlates the current density of the bonded charges in the material that cannot migrate in the same way that the free charges do, but they can be polarized, and accordingly displaced, in a way to form a very small dipoles due to the electrical field [24], [25].

Thus, equation (1) can be written as:

$$\vec{J} = \sigma \vec{E} + \frac{\partial \vec{D}}{\partial t} \tag{2}$$

The conduction current density is represented in the term ($\vec{E}$), where σ is the conductivity of the material, and $\vec{E}$ is the electric field intensity while the displacement current density is represented by the derivative term ($\frac{\partial \vec{D}}{\partial t}$).

The displacement field is related to the electric field intensity and the polarization ($\vec{P}$) [26], according to:

$$\vec{D} = \varepsilon_o \vec{E} + \vec{P} \tag{3}$$

where ε_o is the permittivity of free space, known as the dielectric constant, which equals to 8.85×10^{-12} (F/m).

When the material is assumed to be linear and isotropic (e.g. the electric susceptibility is not a function of the intensity of the electric field), the displacement field equation can be written as:

$$\vec{D} = \varepsilon_r \varepsilon_o \vec{E} \tag{4}$$

where ε_r is the relative permittivity of the material, and it is commonly referred as the relative dielectric constant.

Its value relates the absolute permittivity of the material (ε) proportionally to the free space permittivity, as shown in the equation:

$$\varepsilon_r = \frac{\varepsilon}{\varepsilon_o} \tag{5}$$

Now, substituting equation (4) in (2) will gives us:

$$\vec{J} = \sigma \vec{E} + \frac{\partial(\varepsilon_o \varepsilon_r \vec{E})}{\partial t} \tag{6}$$

For AC and impulse excitation, when polarization effect is significant (frequency is more than 1 Hz [23], or at another frequency, depending on the material), the simple electrostatic field theory is applied, and conductivity influence is neglected with the absence of the mobile charges and conduction current. The electric field is capacitive, and the dominating current in the dielectric is the displacement current. Accordingly, the permittivity, and consequently the relative dielectric constant, is the influential parameter in determining the intensity and distribution of the electric field.

For DC excitation, when frequency is less than 1 Hz [23], the electric field is governed by the conduction phenomena, and the conduction electric field, also called the resistive electric field prevails. Therefore, the dominating factor is the conductivity of the dielectric material that correlates $\vec{E}$ and $\vec{J}$ and shapes the conduction electric field.

For both types of excitation, AC and DC, the electric field intensity and distribution can be found accurately for gases, but it is approximated for liquids and solids since they are not as well-known insulating materials as the gases [23].

To sum up, and as illustrated above, the electric insulating characteristics are related to the relative dielectric constant and the conductivity (the reciprocal of resistivity) properties of the material. The lower the relative dielectric constant and the conductivity, the lower is the current density in the material, and hence, the better is the electric insulating material/system.

1.4.2 Dielectric Strength of Insulating Materials

The dielectric strength, of a material is the maximum value of electric field stress needed to be applied on the electric insulating material to cause an electrical breakdown in the material [27]. In other words, it is the maximum applied electric field that the insulating material can

withstand, and so, can resist decomposition resulting into losing its dielectric properties. The increase in the electric stress of the system, by increasing the system voltage, causes the ionization of material atoms/molecules, and hence, the dielectric breakdown. Thus, the "breakdown voltage" is the maximum applied voltage on the insulation at the breakdown instant [28]. When determining the operating voltage level of devices it is necessary to ensure the insulation material has a dielectric strength which can withstand voltage levels significantly higher than the desired operating voltage [29]. The dielectric strength of a material may vary over its operational lifetime based on the frequency, thickness, temperature, mechanical defects, and contamination [27]. The dielectric strength is commonly measured in (kV/mm) or (MV/m) while the breakdown voltage is commonly measured in (kV).

The insulation media used in electric power devices include vacuum, gases, liquids and solids. In addition, a combination of gas or liquid with the solid insulation is also commonly used as the insulating system for high voltage power equipment [28].

Ideally, vacuum is considered as the best insulator with the dielectric strength up to 1 MV/mm, which is only limited by electron emission from the surface of the electrodes. However, it is reduced to 10 kV/mm when the gap distance reaches several centimeters [28]. In case of vacuum insulation, breakdown does not cause any permanent damage, and the dielectric strength can be restored after removing the applied breakdown voltage. Similarly, for some dielectric gases and liquids, breakdown does not cause a permanent damage to the insulation material [30], so they can restore their dielectric strength if the applied breakdown voltage is removed and the energy released during breakdown does not cause any significant damage to the conductor surface. For solid materials, typically permanent damage occurs to the material in a breakdown event resulting in the materials inability to operate at the same voltage as prior to the breakdown occurrence.

For different insulation media (e.g. gases, liquids or solids), there are generic factors that affect their dielectric strength, which are: shape and nature of the electrodes, shape and frequency of the applied voltage waveform, purity of the sample, and temperature. In general, the dielectric strength decreases with increasing frequency (from pure DC to high frequency waves), as shown in Figure 7. A decrease in the dielectric strength also occurs with the increase of temperature. The raise in frequency and/or temperature gives the electrons the tendency to depart from the atoms/molecules of the insulating material, so the dielectric strength decreases.

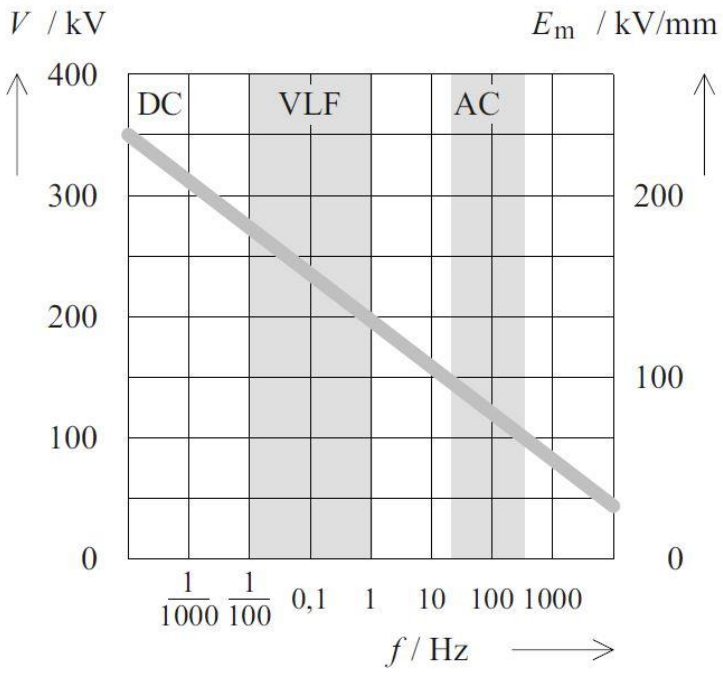

Figure 7: Withstand voltage (V) and dielectric strength (E_m) vs frequency (f) for cross-linked polyethylene (XLPE) cable sample [27]

Besides these main factors, each type of material has its own other specific factors, as discussed below.

1.4.2.1 Gaseous media. For gases, the dielectric strength depends on the gas dielectric properties, the gap distance between the electrodes, the type of gas, the density of the gas, and degree of humidity. The dielectric strength per unit length varies from steadily increasing with the increase of the gap distance in a uniform electric field for small distances, several millimeters, to lower values for large distances, several meters [28]. The most common gas insulator for power and high voltage equipment is air. Its dielectric strength varies from 3 kV/mm (at common temperature, pressure and humidity level) for a uniform electric field and small gap distance to approximately 0.6 kV/mm for several meters of gap distance. In case of lightning, where the gap is very big, the average dielectric strength decreases to 0.1-0.3 kV/mm due to the decrease in the electric field efficiency for the long distances [28].

In gases, the dielectric strength increases with the increase of the gap distance in between the electrodes and with the increase of gas pressure. The dielectric strength is directly proportional to the gas density, as will be elaborated in Chapter 4. Humidity causes a decrease the dielectric

strength significantly of a gas-insulated system. Existence of impurities in most cases reduces the dielectric strength of the gas.

Other important characteristics such as toxicity, condensation temperature, and chemical stability are also considered in selecting a gas for an insulating medium in power equipment [31].

Pressurized gases provide reliable and versatile dielectric media for high voltage insulation applications. The ideal dielectric strength of a gas is typically expressed by its Paschen's law. It is a function of pressure and distance between the electrodes. It describes the relationship of the breakdown voltage, which is the lowest voltage required for starting the electric discharge, between two electrodes in a gaseous medium. In the linear region of the Paschen's curve, increasing the density of the gas results in higher breakdown voltages, as will be shown in chapters 4 and 5. For highly pressurized gases, dielectric strength up to 25 kV/mm have been achieved [28].

Commonly used insulating gases are Nitrogen (N_2), mostly used at high pressures, with a dielectric strength same as air, carbon-dioxide (CO_2), Freon (dichlorodifluoromethane, CCl_2F_2), and Sulphur Hexafluoride (SF_6) [28], which has been designated in 1997 (at the Third Conference of the Parties (COP3)) as a greenhouse gas, significantly affecting the global warming. Thus, insulating gases with other characteristics, besides their dielectric strength characteristic, such as condensation temperature, toxicity, and chemical stability have been investigated with the goal of finding effective, safer, and environmentally acceptable alternatives [31].

1.4.2.2 Liquids. The dielectric strength of liquids depends on their dielectric properties (i.e. their molecular structure), the gap distance in between the electrodes, and existence of impurities. In addition, the electrical characteristics that are considered to evaluate the liquid suitability for power apparatus are conductivity, permittivity, loss tangent or power factor, and the ability to withstand high stresses. Other important characteristics as toxicity, gas content, flash point, stability, and viscosity are also considered [28].

Liquid insulation media have been used in high voltage power equipment, and they are preferred when heat conduction is required besides the insulation properties. Although that liquids are resilient after failure caused by an over voltage, the solid insulation supports deteriorate due to the discharge deposit may eventually result into surface breakdown. A 100 kV/mm dielectric strength for highly purified liquids can be achieved with the commercial liquids under ideal conditions, but real service conditions of the existence of impurities and dissolved gases the dielectric strength of liquids is reduced considerably. The mineral oils are the most commonly

used in power equipment as insulating liquids, but others such as silicones, fluorocarbons, askarels, and organic esters (including castor oil) are also commonly used. In addition, polybutanes have been increasingly used in power industry due to their excellent properties. For practical applications, when the piece of equipment is continuously in operation, it is recommended that the liquids are used around voltage stresses of 5-6 kV/mm. Higher voltage stresses, 10-20 kV/mm can be tolerated by liquids in high voltage applications (like high voltage bushings) when the liquids are only filling up the voids in the solid insulation [28].

1.4.2.3 Solids. The dielectric strength for solid materials is higher than that of gases and liquids, and it depends on the molecular structure, thickness, the characteristics of the surrounding medium (i.e. gas or liquid) and ambient conditions, such as pollution and humidity in case of gaseous surrounding medium [28], [27].

Regarding the thickness, the dielectric strength is not linearly proportional to the thickness of the insulating material. The higher dielectric strength per unit thickness is achieved with the thinnest layer of the material sample because thickening the material increases the probability of defects, which can be in the form of voids or/and impurities, and these defects lower the dielectric strength [32], [33].

A 1 MV/mm of dielectric strength can be achieved in some solids under ideal conditions when the material is perfectly homogenous with no imperfections and is in a carefully controlled environmental conditions. Such a breakdown is called “intrinsic breakdown strength” [28]. As in liquids, this cannot be achieved in practice in solids and the typical dielectric strength is much lower, and usually the breakdown occurs over the surface instead of occurring through the bulk of the solid insulation. The most common reasons behind the failure of solid insulation materials are the discharges that occur either on the surface of the solid insulation or within the voids [28].

In addition to the above mentioned factors, ageing factor also affects the dielectric strength of the insulating solid materials [30]. Electric field non-uniformity also affects dielectric strength materials significantly.

The solid insulation materials can be broadly categorized into the following three groups [28]:

- Organic materials (amber, paper, pressboard and rubber)
- Inorganic materials (ceramics, glass and mica)

- Synthetic polymers, which are divided into thermoplastics (polyethylene, Perspex and polypropylene) and thermosetting (epoxy resins)

1.4.2.4 Composite materials. Several combinations of solid insulation with a gas or a liquid have been utilized as insulation media. Composites are sometime more useful due to their higher dielectric strength, mechanical strength, chemical stability, and longer life needed for the insulation system of electrical power devices. For instance, oils are used to impregnate the solid insulation layers in conventional cables and transformers to increase the heat transfer capability and also to increase the dielectric strength of the insulation system.

Despite the benefits of composites, the interface between materials can cause the reduction in the dielectric strength and failure of the electric insulation system due the electric field enhancement caused by the different dielectric properties for the interfaced materials. The most common undesired combination occurs with use of solid insulation since it is usually surrounded by gaseous medium. The interfaces between solid insulation and the other materials, such as gas or liquid, are the common reasons behind the failures of solid insulation materials.

The most common interface is the surface of the solid material and the surrounding gas medium. This interface causes an electric field enhancement at the meeting point with electrodes. The insulator surface provides a weaker path for the discharge, and this phenomenon is commonly known as the surface flashover. The failure of the insulation surface can happen by forming a conducting path (this phenomenon is called “treeing” or “tracking”), or it can simply occur in the form of a flashover. In practice, the failure of the insulation surface is the most common cause of insulation failure in electrical power equipment [28]. Moreover, the surface flashover voltage decreases with the existence of humidity and pollution [27]. Details of this phenomenon will be discussed in Chapter 7.

Another common interface occurs in the voids/cavities within the solid material which are filled by a gas such as air. The gas filled voids cause a phenomenon called the “partial discharge (PD)”. The voids in the insulating solid material suffer from electric field enhancement causing local field intensity higher than the applied AC electric field average due to the interface between the two different dielectric materials. Due to the electric field enhancement, the air/gas molecules decompose exhibiting a discharge [27]. This discharge happens in local regions in the solid insulator, not connecting the electrodes [30], and that is why it was called partial discharge. It reduces the dielectric strength, and it also impacts adversely the lifetime of the electrical insulation

system. Thus, the PD is an indication of the deterioration of the insulation of electrical equipment. Partial discharge phenomena have been receiving more attention in the last 3 decades because they determine the life time of the insulation versus the electric stress characteristics for the solid insulating material [29]. The adverse impacts of PD on HTS cable designs is illustrated in subsection 1.5.2, and a solution to address the PD challenges is discussed in subsection 1.5.3.

1.5 Electrical Insulation Challenges for Superconducting Power Devices

1.5.1 Cryogenic Temperature Considerations for Electrical Insulation System Design

For solid electrical insulation materials that are used as insulation components for HTS cables/devices, there are mechanical issues that should be taken into consideration. These issues come from the thermal contraction due to the cryogenic operating temperatures. Since the materials' shrinkage rate is different for HTS material and the insulation material, the HTS layer may crack causing a permanent damage to the HTS material. Moreover, the mechanical brittleness for solid insulation materials make them unsuitable for HTS cables [34]. Besides that, HTS materials are different from conventional metallic conductors, copper for instance, so they may not tolerate the high temperature of the insulation layer extrusion process. The existence of sharp edges in thick tape HTS materials make it more difficult to extrude insulation. Thus, lapped tape insulation using polypropylene laminated paper (PPLP), over the HTS inner conductor cable design is preferred over extruded solid insulation. However, extruded design has been investigated and developed with limited success with ethylene propylene rubber (EPR) [35].

When using plastic materials in the HTS cable insulation systems for mechanical support purposes, serious attention should be paid to the cryogenic temperature aspect. Again, this is due to the fact that plastic materials become brittle at cryogenic temperatures. Cracks can occur leading to mechanical damage and electric field enhancement leading to system failure such as electrical faults or superconducting material quench.

1.5.2 Partial Discharge Limitation in HTS Cables

The partial discharge (PD) phenomenon represents a challenge that limits the design options of liquid or gaseous cryogen based HTS cable insulation system. While liquid nitrogen (LN_2), which is used as the coolant and dielectric medium in many HTS power cable designs, partial discharge streamers that occur during pre-breakdown stage can significantly cause

irreversible degrade to the solid insulation material. The degradation happens in an erosion form which can be as surface damage for polytetrafluoroethylene (PTFE), or in the form of a hole for glass fiber reinforced plastic (GRP) insulation materials [36].

For the lapped-tape HTS cable designs that use a gas as the cryogen, the gas penetrates the solid insulation layers. Butt gaps are used to reduce mechanical damage and to avoid excessive stress applied on the HTS tape by the insulation layer [37]. The gaps in the insulation also form due thermal contraction during cool down to cryogenic temperatures [38]. The gas molecules fill the butt gaps, as shown in Figure 8. Under AC electric field, PD occurs due to the fact that the gas filling the butt gaps has lower permittivity than the solid insulation, which causes a local electric field enhancement. For instance, for helium gas that is used as the cryogen, the relative permittivity is 1.0. It is less than the relative permittivity of the surrounding solid, which is greater than 2. Thus, the trapped gas suffers an electric field approximately double the average electric field intensity [35]. That leads to PD occurrence at lower voltage levels than the rated operation voltage. The low partial discharge inception voltage (PDIV) might lead to total failure of the electric insulation as it causes local damage to the solid insulation and over time adversely impacts the performance and lifetime of the solid insulation [39].

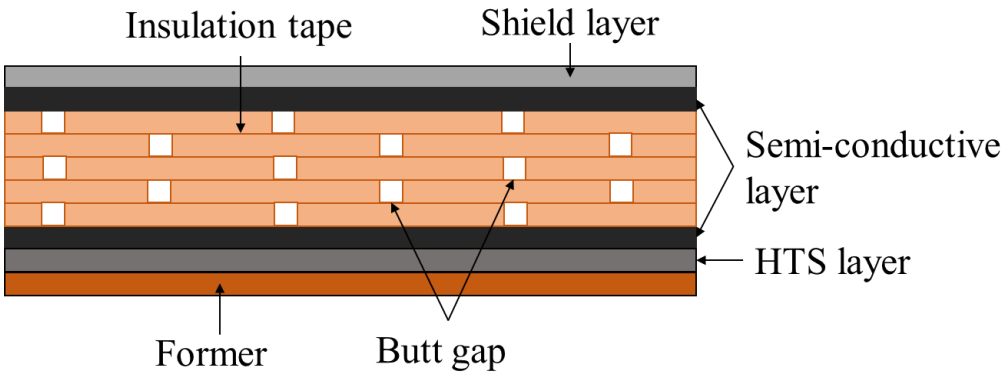

Figure 8: Butt gaps in between the lapped tape-layers of HTS cable [38]

1.5.3 Addressing Low Partial Discharge Inception Voltage Issue for Gas-Cooled HTS Cables

Previous research in our research group addressed the low PDIV issue. Attempts to address the low PDIV by adding more lapped tape layers and increasing the gas pressure showed little success. Using the gas mixtures with increased dielectric strength also did not help much [40].

Extruded polymers, such as EPR, seemed to be promising to prevent voids, but helium gas is difficult to prevent penetration in to the insulation materials [35].

As mentioned above, strengthening GHe by helium-based gas mixtures has been investigated. As will be discussed in Chapter 4, some gas mixtures showed higher dielectric strength than pure GHe. Encouraged by the significant enhancements in the dielectric strength in He-H_2 mixtures, a new cable design that is similar to the gas insulated line (GIL) was proposed [41]. For GIL design, the cable needs to be centered at the axis of the gas pipe to have the required clearance, and accordingly, to provide the required dielectric strength for the insulation system [42]. The coaxial cable design (i.e. inner and outer diameters) should be carefully chosen to prevent corona discharges inside the cable [23]. In addition, paying attention to the insulator spacers design is important since it should fulfill the electrical and thermal aspects, and gas flow (in case of HTS cable application) requirements.

1.5.4 Bubble Formation in Liquid-Cooled HTS Cables

As the focus of this dissertation is the dielectric aspects of gas-cooled HTS cables, the dielectric strength of gases is investigated, as will be discussed in Chapter 4, and the gas-cooled HTS cable design is also discussed and experimentally examined, as will be shown in Chapter 5.

To understand the limits of the S-GIL design and to thoroughly understand the relationship between the intrinsic dielectric strength of the medium and the highest possible operating voltage for a given design, liquid nitrogen (LN_2) was used for the insulation medium in S-GIL design concept. LN_2 is a much stronger dielectric compared to GHe in general if bubble formation can be mitigated/suppressed. Compared to the dielectric strength of GHe, which is 4 kV/mm in a uniform electric AC field at 1.0 MPa and 77 K [43], LN_2 is stronger with a dielectric strength of 19.6 kV/mm when the bubble formation is prevented regardless of temperature and pressure [44]. However, its dielectric strength decreases to half with the presence of bubbles [45]. At atmospheric pressure, the bubbles form in boiling LN_2 [2]. The bubble formation can be prevented by pressurizing and subcooling LN_2 below the normal boiling point. For example the boiling point can be increased by 20 K by pressurizing it to 0.5 MPa [46]. By increasing the boiling point and lowering the operating temperature below 77 K, a significant reduction in bubble formation has been achieved.

1.6 Organization of the Dissertation

The dissertation is organized as follows:

- Chapter 2 presents a vision of cross-country multi-terminal superconducting dc power cables that can provide a solution for integrating remotely located renewable energy resources into the power grid and connecting different grids without any synchronization issues. The chapter discusses the technical challenges and potential solutions to realize long distance superconducting DC lines. The work discussed in Chapter 2 was presented at the Cryogenic Engineering Conference and the International Cryogenic Materials Conference (CEC-ICMC 2017) and published in:

  A. Al-Taie, L. Graber, and S. V. Pamidi, "Technical Challenges and Potential Solutions for Cross-Country Multi-Terminal Superconducting DC Power Cables," *IOP Conf. Series: Materials Science and Engineering* 279 (2017) 012034
- Chapter 3 presents the facilities and the experimental arrangements of the high voltage laboratory used for the measurements presented in the dissertation. In addition, the challenges of performing high voltage experiments at cryogenic temperatures are discussed. A brief discussion of the experiments performed to develop the experimental protocol necessary to ensure temperature equilibrium during the breakdown measurements in high pressure cryogenic gas media.
- Chapter 4 elaborates on the mechanism of electrical breakdown in gases and the dielectric strength of the gases, which is determined using Paschen's curve. A new representation of the Paschen's law is postulated that relates the dielectric strength to the gas density and gap distance, instead of the pressure and gap distance. The new representation is better suited for applications where the gas media is used as insulation medium at varying operating temperature and pressure. The chapter ends with a summary of the knowledge of the dielectric strength GHe and gas mixtures. Part of the work described in Chapter 4 was presented at the 2019 IEEE Electrical Insulation Conference (2019 EIC) and published in:

A. Al-Taie, C. Park, P. Cheetham, C. H. Kim, L. Graber and S. Pamidi, "A New Representation of Paschen's Law Suitable for Variable Temperature Power Applications," in *2019 IEEE Electrical Insulation Conference (EIC)*. (in press).

- Chapter 5 discusses the S-GIL design concept and the insulator designs involving tubular spacers made of different materials. Experimental results of the high voltage measurements on the different designs at a range of gas pressure up to 2 MPa are also discussed. Experiments using gas mixtures were also discussed. This work will be published soon.
- Chapter 6 presents the research that extended the studies on S-GIL design concept with replacing the gaseous cryogen with liquid nitrogen to test the limits of the S-GIL and further establish the relationship between the intrinsic dielectric strength of the insulation medium and the maximum possible voltage that can be achieved with the SGIL. The chapter discusses the better thermal aspects that the liquid cooled cable design provides compared to the solid insulation HTS LN_2 cooled cables. Part of the work described in Chapter 6 will be presented in the 2019 Cryogenic Engineering Conference and the International Cryogenic Materials Conference (CEC-ICMC 2019) and will be published in:

  A. Al-Taie, S. Telikapalli, P. Cheetham, C. H. Kim, S. Pamidi, "Liquid Nitrogen Cooled Superconducting Power Cable with No Solid Insulation," in *IOP Conference Series: Materials Science and Engineering*. (under submission).
- Chapter 7 provides the fundamental investigations on the surface flashover phenomenon in gaseous media. The chapter discusses two different experimental setups. The first experimental setup allowed us to learn from the challenges with aligning the electrodes with the solid insulator specimen and resulting discharge along the paths different from the desired one. The second, improved set up for measuring surface flashover voltage in gaseous helium and other gaseous media addressed the challenges experienced with the first set up. Surface flashover measurements were conducted on different solid materials in different gas media at room temperature and cryogenic temperature. Part of the work described in Chapter 7 was presented in the 2018 Applied Superconductivity Conference (ASC 2018) and published in:

A. Al-Taie, P. Cheetham, S. Satyanarayana, C. Park, J. Wei, C. H. Kim, L. Graber and S. Pamidi, "Understanding Surface Flashover Strength in Cryogenic Helium Gas for Superconducting Devices," in *IEEE Transactions on Applied Superconductivity*, vol. 29, no. 5, pp. 1-5, Aug. 2019, Art no. 7701805.

Another Part of the work described in Chapter 7 will be presented in the 2019 Cryogenic Engineering Conference and the International Cryogenic Materials Conference (CEC-ICMC 2019) and will be published in:

A. Al-Taie, P. Cheetham, S. Telikapalli, C. Kim, S. Pamidi, C. Park and L. Graber, "Understanding Surface Flashover in Helium Gas Cooled High Temperature Superconducting Devices," in *IOP Conference Series: Materials Science and Engineering*. (under submission).

- Chapter 8 presents broad conclusions of the research conducted for this dissertation and include a few ideas for future work as continuation of the work presented here.

CHAPTER 2

CROSS-COUNTRY MULTI-TERMINAL SUPERCONDUCTING DC POWER CABLES

2.1 Introduction

There is a renewed interest in DC systems in power transmission and distribution. By the start of the last century, an efficient electrical power transmission system was needed to transfer the power over long distances and to start the expansion of the power grid. The ability to change the voltage levels by AC power transformers was the settling point for the War of the Currents and the start of utilizing the AC power system by the end of the nineteenth century [47]. Even though AC power became the norm since then, DC power transmission was not totally ignored. This is due to the fact that the DC power technology provides an efficient and effective interconnection between any two independent AC grids to transfer power [13], in addition to adding stiffness to both of them. The conventional solution for this is known as the rotary converter. It is essentially a motor-generator coupled machine. The unit connected to the grid that supplies the power to be transferred operates as a motor, and the other unit operates as a generator and is connected to the grid receiving the power. This method is used in several locations around the world. For instance, in Japan, it is used to connect power networks of adjacent areas with different frequencies, 50 and 60 Hz. Hundreds of MVAs can be transferred using this method [48]. Basically, the motor-generator coupled machine need to be built to the maximum rating of the power transferred, so the coupled machine must be built to GW scale if it is intended to transfer power in that range. However, there is a growing trend towards using of solid-state solutions based back-to-back (B2B) high voltage direct current (HVDC) grids tying systems [49].

Having mostly relied on the AC power transmission and distribution (T & D) systems for the last century, the utilization of the DC systems is being considered and the interest is growing [13]. The new trend of increasing reliance on renewable energy sources, which provide ample amounts of energy usually at remote locations, requires a very efficient method to transmit these large amounts of energy to urban demand centers. The rapid development in power electronics has contributed in utilizing HVDC power transmission and making it feasible and controllable. Currently, and after decades of notable success in the HVDC transmission field, DC transmission

is preferred over the AC when the power transmission distance exceeds the break-even point. It presents the meeting point for the AC and DC systems' capital and operational cost curves. The break-even point is in the range of 500 to 800 km for overhead lines, but much shorter for underground cables, which is between 20 and 50 km for submarine cables and twice as long for underground cables [50]. The reason behind the lower values for the break-even length in cables is due to the cable's capacitive charging length when transmitting power in AC form [2]. However, this limitation does not exist when transmitting DC power. Additional benefits for the HVDC transmission system over the HVAC are discussed elaborately in the literature [47], [51]. In conclusion, HVDC transmission is an efficient and economical choice for transmitting large amounts of power over long distances.

The next step will be to expand HVDC point-to-point links to a true multi-terminal HVDC (MT-HVDC) system, which has the ability to provide all the above-mentioned benefits while adding more flexibility with respect to system control. Recently, enhancing the transmission system capacity and improving the system control are the two major challenges that are facing the power sector in North America [13]. Therefore, considering the MT-HVDC power transmission systems is a prospective innovative solution that can help with addressing these two challenges. MT-HVDC systems support the grid in many aspects, like serving as asynchronous ties between multiple grids/networks and providing a system that can transfer power in a more efficient way over long distances, besides the ability to receive or deliver the power at multiple points necessary for integrating distributed renewable energy sources into the grid.

The realization of the need for the MT-HVDC systems is increasing every day because they offer a full seizing of the technical and economic benefits of the HVDC transmission system [52]. Figure 9 shows the potential of MT-HVDC systems in decreasing the total capital cost by reducing the converter stations needed. However, switchgear is needed to control the power flow and for protection.

2.2 Need of Superconducting Cable Technology for the MT-HVDC Systems

The MT-HVDC system involves handling large amounts of power, on GW scale. This will lead to some challenges such as:

- If suspended overhead cables and transmission lines were used, they would be vulnerable to atmospheric conditions including weather and lightening.

- If underground conventional cables were used, the complexity and size of the project would be substantially higher since these cables need to be separated by several meters to avoid the overheating [12]. Besides, due to their size, it is more difficult to obtain right of ways for larger areas for the station footprints, especially when it is within urban areas [13].

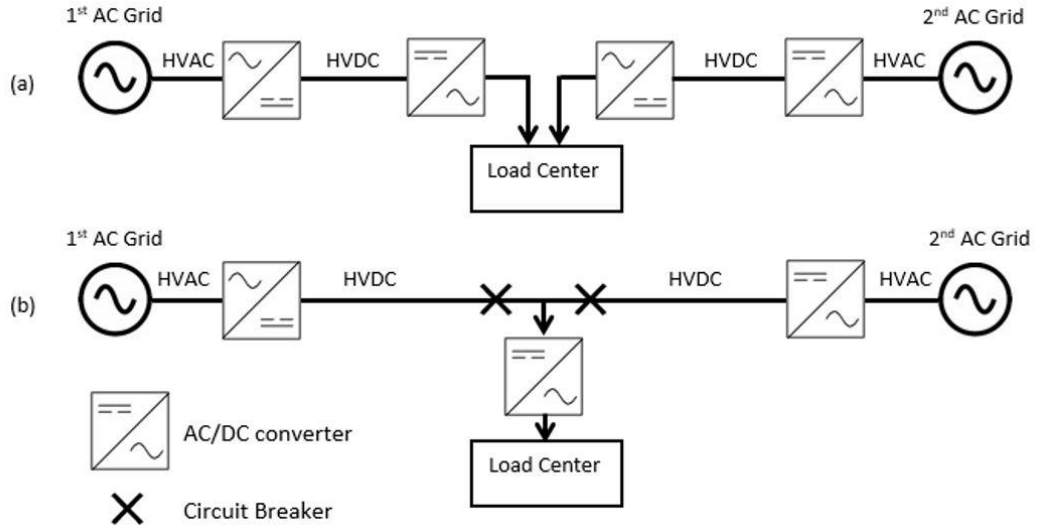

Figure 9: (a) Two point-to-point HVDC links with 4 converters (b) the same two DC links connected in a MT-HVDC configuration with 3 converters

All these problems could potentially be addressed by replacing conventional cables with state of art HTS cables. Underground HTS cables will address the weather conditions concerns. Besides, the superconducting DC power cables have the attractive "zero loss" state. Although the superconducting cables offer higher in efficiency when transmitting AC power compared to the conventional cable technology, they are even better when transmitting DC power due to the absence of the significant negative impact of the AC losses, which will be discussed in the next section. Thus, each superconducting HVDC cable has the ability of carrying currents up to 100 kA whereas the conventional HVDC line can carry a few kA at most [13], and so, less right-of-way and footprint are needed. In addition, if more cables are needed for the sake of expansion, the Superconducting DC cables can be buried closer to each other unlike the conventional cables due the fact that magnetic field can be completely eliminated outside the superconducting cable with

a proper cable design [12]. In summary, the HVDC based HTS cable technology offers the optimum solution to achieve higher performance and power density for the MT-HVDC systems.

In Europe, the vision of using superconducting HVDC for long distance transmission is being explored under a large project aimed at moving towards a low-carbon economy called the "Best Paths" program. The program intends to develop technologies to increase the capacity of the European interconnected transmission networks [53]. The main goal is to integrate the abundant renewable energy, from the wind farms smoothly and efficiently into the pan-European power transmission network. Thus, the program intends to achieve the European MT-HVDC based HTS cable power transmission network. The HTS cable for the program intends to use the magnesium diboride (MgB2) superconductor and cooled with gaseous helium (GHe), and they are investigated to carry currents up to 5-10 kA under 200-320 kV of high voltage levels to transfer up to 3.2 GW of power [54].

2.3 AC Losses in Superconducting Cables Due to Ripple and Harmonics from Converters

AC Superconducting power cables suffer from AC losses. DC superconducting cables do not produce any losses as long as the DC current is clean and free from AC ripple and harmonics that originate from the power converters [55]. The extent of losses due to ripple is small, but it is necessary to eliminate it for long distance superconducting DC cable systems to make them more efficient and to minimize the expensive cryogenic cooling capacity required [56]. The harmonics could also come from reversing the power flows in HVDC based HTS systems. There are a few different converter topologies that can be used in HVDC systems [56]–[60]. The selection of converter topologies for HTS HVDC systems has to be based on their suitability for high current operation and the need for clean DC power. It has been reported that the parallel hybrid modular multilevel HVDC converter design offers significant reduction in the extent of ripple in HVDC systems. [60]. Long distance cables tend to dampen the ripple in general, but it is important to consider this issue in the design of superconducting cable for HVDC applications for negligible steady state losses [55]–[59].

2.4 Technical Challenges and Potential Solutions for the MT-HVDC HTS Cables Technology

2.4.1 Superconducting Technology Challenges

HTS technology has the potential for providing an efficient MT-HVDC systems, but has its own technical challenges, cost issues, and lack of standards and industry accepted test protocols.

Regarding to cost, there have been several early and recent research studies for utilizing superconductors to transport large amounts of power over long distances [61], [18]. The Electric Power Research Institute (EPRI) conducted research on the economic feasibility of utilizing superconducting cables for transmitting large amounts of power over long distances. The analysis concluded that a superconducting cable system would cost approximately the same as a conventional transmission line if the line is transmitting power in excess of 5 GW, over a long distance of about 1,000 km. Part of that result due to the fact that the cost of the cryogenic system, which is needed to maintain the superconducting properties, will be a small share of the total cost [13]. In addition, while the efficiency of the conventional power transmission lines drops substantially when carrying bulk power over long distances, the high efficiency of superconducting cable systems will not be affected. Furthermore, the power losses in the terminations are constant and not affected by the cable length. These termination losses are a large fraction of the total losses of the system because they handle the connection between the ambient temperature of the current leads and the cryogenic temperature of the superconducting cable. However, these losses decrease relative to the whole system losses with the increase in cable length to negligible values with respect to the total cost. Furthermore, a drop in the cost of the superconductor and power electronic converter technology is expected in the near future. The increase in manufacturing capacity of volume of HTS materials and cables will bring about a substantial decrease in the cost due economies of scale. On the power electronics side, the device prices are dropping rapidly, which will reflect on the capital cost drop for the converter substations. However, new technology devices, like silicon carbide (SiC) devices, are still not in the mass production level to allow a practical cost estimation. In addition, the prospective development in the HTS materials and the efficiency of the cryogenic cooling system is expected to further reduce the capital and operational costs. Thus, at this point the technology is not mature enough to conduct a meaningful economic analysis for such systems.

One obstacle for HTS technology is the lack of standardized test methods. It is still an issue for the utility companies to perform testing for the HTS DC cables because there is no a standard test for it, in contrast to the HTS AC cables as was achieved discussed [62]. This presents one of the major challenges for utilizing HTS DC cables widely in power grids. HTS DC cable has its unique challenge in performing a load cycle, contrary to the HTS AC cable or the conventional HVDC cable. Applying both voltage and current simultaneously through the use of a current transformer is impossible due to its AC loss characteristics [63], [64]. Thus, some appropriate new methods for performing reliable and acceptable qualification tests on HTS DC cable are needed. On the other hand, thermal cycling studies of HTS cables is very important for utilities to demonstrate and verify the cable's lifetime since the cables will be subjected to several contractions and expansions during cool-down and warm-up cycles during installation and operation. The thermal cycles are similar to HTS AC cables that are in operation and hence some data exists. The thermochemical issues are design dependent and further work is needed to qualify the designs for 30-40 years of service as required by electric power companies [65], [66]. However, for the planned and installed HVDC based HTS cable projects, the utilities companies have started constructing test centers and establishing specialized tests for the new technology. One of the latest projects that was implemented in South Korea, which has combined two standardized tests, besides the HTS experience. South Korea is one of the earliest countries that adopted the smart and clean energy applications and has been considerably progressing in developing the HTS power cables integration to the real Grid. A project by the Korea electric power corporation (KEPCO) and LS Cable Limited has done the designing and manufacturing part, and started researching the HVDC based HTS cable integration into the Gumak grid in 2011 [67]. The big picture of the project is to connect two conversion stations, from Halim conversion station to Gumak conversion station, by a 5.3 km long DC line. A 0.5 km long underground HTS DC cable project was meant to connect an existing 4.8 km long DC overhead transmission line to Gumak conversion station. Therefore, a ±80 kV, 3.25 kA, 500 MW DC HTS cable was constructed and installed in the Gumak converting station. After passing successfully all the tests by the 101 m cable prototype, the actual cable was installed and started the demonstration in the real grid since October 2014 [68]. For testing, the recommendations were based on Electra 496 and Cigre TB 538, and the HTS experience. In addition, an additional measurement for the DC HTS cable lifetime was performed. That was done through the investigation of the cable response to the mechanical stress due to cool-down and

warm-up cycles. The testing period was from 20 Dec. 2012 to 31 Oct. 2013, and the results showed that a combination of HV tests with the HTS experience, which was called the qualification test, is required for the HTS DC cable project. Finally, a test for the cryogenic system is always required to verify the ability of the cooling system to handle the cable performance as designed.

2.4.2 Cryogenic Systems Challenge to Support Long Distance Superconducting HVDC Systems

One of the major challenges in bringing HVDC based HTS cable systems to the power grid until recently has been the lack of reliable and economic cryogenic refrigerator systems. This challenge has recently been addressed by the industry through the development of large cryo-refrigerators based on Turbo-Brayton cycles with >150 kW cooling power at 70 K [69], [70]. These large cryogenic systems are significantly more efficient and require little maintenance compared to Stirling refrigerators and Gifford-McMahon cryocoolers [71]. Turbo-Brayton cryocoolers have been used successfully for the HTS cable projects in Korea [72], [73]. Further new approaches are being investigated to reduce the complexity and costs of the cryogenic systems for large HTS systems [74], [75]. Further technical advancements are needed to improve the reliability and reduction of capital and operational costs of cryogenic systems and the interfaces between the room temperature components and cryogenic components at the terminals of MT-HVDC systems.

2.4.3 MT-HVDC Systems Technology Challenges

The MT-HVDC based HTS cable systems will face the same challenges of the conventional MT-HVDC systems, such as the DC fault protection and the control of the power flow for the meshed DC system with different kinds of converter types.

One major difference between HVDC and HVAC is in the management of faults. While HVAC systems rely on its natural current zero crossings to clear the fault, HVDC requires more complicated circuits to create artificial current zero crossings. It has been reported that the fault current magnitude in HVDC transmission systems will be lower than in HVAC systems for the same amount of the power transmitted [76]. The real problem with the DC systems is the faster rate of the rising fault current than in AC systems [77]. This is due the faster DC system dynamics and transients, which means a very sensitive DC fault relays are needed to detect faults and DC circuit breakers are needed to remove faults quickly. Unfortunately, these kinds of DC circuit breakers are still not commercially available, but there have been some developments of building

and testing of a few prototypes [78]. However, this issue can be dealt with by using the HTS cables, if these cables were designed to operate as fault current limiting (FCL) cables [2]. The superconducting material loses its superconducting property when the current exceeds its critical value (*Ic*) and transitions to the normal state of being a high resistance material. However, the HTS cables should be designed in a specific way for that particular purpose, or else they could be damaged by the massive fault currents. Thus, this is a great feature for the HTS power transmission cable systems that give them a distinguished advantage making them more attractive over the conventional systems. To conclude, use of FCL HTS cables can a contributing factor to solve the protection problem for the MT-HVDC systems, which is a big draw back for the conventional cable/line-based MT-HVDC systems.

2.4.4 Challenge of Establishing Research and Development Centers

The laboratory establishment for research and development of large superconducting systems is still a challenge for the MT-HVDC based HTS cable systems. Unlike the advantages of changing the magnitudes of voltage and current by the transformers in the case of AC system experiments, establishing the required large DC power sources for testing MT-HVDC based HTS cable systems is a major challenge, especially coupled with the need for collocating the large cryogenic systems in the laboratories and research facilities. The conventional cables' laboratories and testing facilities lack for the existence of cryogenic cooling systems. As a result, the experimental research work on MT-HVDC based HTS cables is still an issue that needs to be addressed by making the necessary investments, which will accelerate the development and implementation of this game changing technology. Therefore, for modelling and analysis of the MT-HVDC based HTS cable systems, simulations are needed. The real-time simulation for these systems is very important as for any new piece of power equipment that needs to be integrated into the grid. The simulations are also important due to the fact that the DC system stability and dynamics are much faster compared to the corresponding AC systems [77].

2.5 System Components

2.5.1 Converters

Many types of converters have been utilized in the HVDC systems all over the past years. The load commutated converter (LCC), based on thyristors, was introduced first during the 70s of

the past century [79]. It is suitable for bulk power transmission, with low losses (approximately 0.7% of losses per converter), but it lacks for the turn off feature. Thus, it has a drawback regarding to controllability. Besides that, it has disadvantages of needing variable reactive power from the Grid, AC source on both ends for successful commutation, and transformers on AC sides to have a 30-degree phase shift. Then the voltage source converter (VSC), which utilizes insulated gate bipolar transistors (IGBTs) was introduced by ABB and marketed as "HVDC Light" in 1997 [79]. It uses the pulse width modulation (PWM) technique for better voltage waveform and less harmonics. It has higher losses compared to LCC (typically 1.7% of losses per converter). However, it has many other advantages over the LLC, besides the source controllability: First, the conversion station is more compact, less foot print, due to fewer/smaller harmonic filters are needed. Second, it can be utilized anywhere in the grid, whether it is a weak or strong network, with no consideration for phase shift. The capability of offering the blackstart and the many other technical features made the VSC to be more preferable over the LLC. In 2010, a new multilevel VSC technology called modular multilevel converter (MMC) was introduced simultaneously by two companies (Siemens and ABB) in two projects [79]. Siemens's HVDC PLUS technology project, the Trans Bay project, was an 88 km subsea cable installed to transfer 400 MW of power from Pittsburg to the city of San Francisco in California [80]. This converter was introduced by Marquardt and Lesnicar in 2002 [81]. It has a better efficiency than the VSC (almost 1% of losses per converter) due the less needed switching frequency, with better control. Thus, it really represents the state of art for the HVDC converters' technology.

2.5.2 HVDC HTS Cables

The HTS HVDC cables connect the converter station in one grid to the other, or extend between any two converter stations as in a MT-HVDC radial link. These cables, which are actually pipelines, handle and carry a large DC current between the conversion stations. Since the application in which the HTS cable is going to be used is directly impacted by the design configuration decision, a single pole per envelope design configurations is used for the HV applications [2]. Different cable layouts have been proposed, the warm, the cold and the two-stage dielectric HTS cable layout. Each one of them has its own advantages and disadvantages. The different aspects of these designs have been investigated and the results showed that the warm dielectric cable design is the right fit for the HVDC HTS cables due the absence of the induced currents on the cryogenic piping [82]. Besides, it is expected to be less costly, because there is no

need for a special cryogenic dielectric medium. Additionally, it requires smaller diameter of cryogenic piping. However, it occupies more volume because each DC pole requires an individual separate cryostat [2]. Thus, the total cross section of the warm dielectric HTS cable is significantly larger than the Cold Dielectric for a given power rating, which reflects in lower effective power density of the cable. Therefore, the cold dielectric cable design is preferable over the warm dielectric where compact HTS cables are preferred.

Regarding insulation, so far extruded insulation has been reported rarely in the technical literature, including extruding thin layers on the HTS tapes directly [2]. Although the extruded insulation possibilities exist for the warm dielectric cable design, but it is not preferred for the cold dielectric designs, where the lapped tape insulation has been used commonly. Here, the insulation tapes wrapped onto the HTS layer and surrounded by the cryogenic coolant, which penetrates the insulation layers to serve also as dielectric medium, inside the cryostat. However, the dielectric properties vary for the different kinds of the cryogenic coolants. For example, with one sheet of PPLP, at 77 K of temperature and within a uniform electric field, liquid nitrogen has higher dielectric breakdown strength of values around 270 kV/mm of DC voltage and 115 kV/mm of AC voltage than GHe, at 1.0 MPa, which is around 180 kV/mm and 60 kV/mm of DC and AC voltages, respectively [83]. Nevertheless, it would be more economic and easier in cable manufacturing if the researchers or the manufacturers succeed in developing an extruded cryogenic insulation which can form a thin layer over the HTS layer instead of the lapped-tape insulation.

Since the cryogenic coolant submerge the insulation tapes, it is critical to keep the coolant operating temperature under the boiling temperature to avoid having any bubbles which can deteriorate the insulation integrity, and consequently, the performance of the HTS cable. For that purpose, pressurizing and subcooling are used to increase the margin between the operating and the boiling temperatures. For instance, the permissible temperature raise of LN_2 over the operating temperature, which is 75 K, increases from 2 K at 100 kPa pressure to 20 K at 500 kPa of pressure [46]. Increasing the temperature margin will also increase the HVDC cable length limit, with the absence of the charging length limit in HVAC cables, so that the cooling stations can spaced apart farther. Moreover, for long distance HTS cables, the corrugated cryostat pipes, which helps with making the pipes flexible for bending, can be replaced by flat smooth pipes to reduce the pressurized coolant friction and the cost.

2.5.3 Terminations

The cable termination is the interface between the room temperature components and the cryogenic components of the system and are the locations of current injection and the cryogenic inlet and outlets. A schematic of a cable termination is shown in Figure 10. The thermal, the mechanical and the electrical stresses are all mostly concentrated in the terminations and hence the MT-HVDC based HTS cables system requires efficient and effective termination designs.

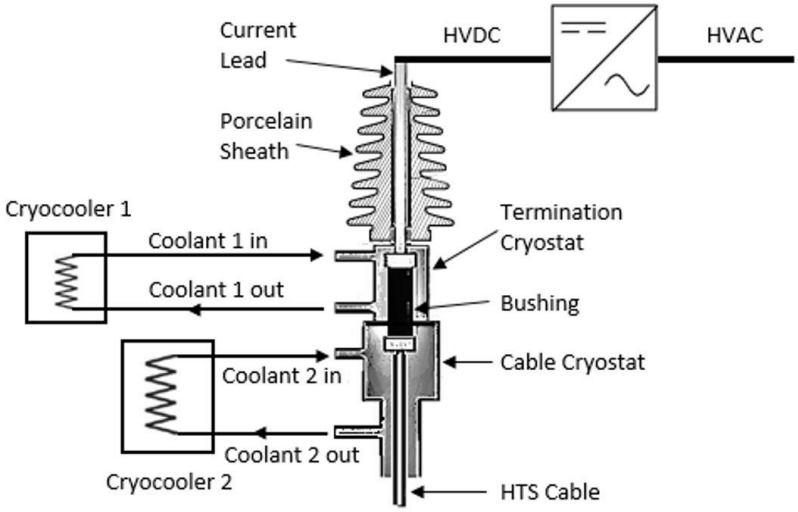

Figure 10: Proposed two-stage cooling HTS cable's termination

2.6 System Configuration

Several possible configurations exist for MT-HVDC based HTS cables systems. According to the particular application served by the MT-HVDC system, an appropriate configuration has to be designed. If the application is to have a MT-HVDC system that spans long distances, cross-country MT-HVDC system, the radial configuration as shown in Figure 11 is more suitable. This cross-country radial MT-HVDC scheme is appropriate for transferring the power from a renewable energy source, Terminal 1, all the way to the far away AC grid of the load center, Terminal 4. It also has other taps at certain locations in between to deliver or withdraw power from the cable system, terminals 2 and 3. In addition to the bidirectional power injection that these two terminals offer at their locations close to other generation/load centers, it can serve the purpose as cooling stations for the HTS cable system to maintain the operating temperature and pressure for the

cryogenic coolants. To calculate the distance between any two cooling stations, the following equation is used:

$$Q = \dot{m}\ Cp\ \Delta T \tag{7}$$

For instance, if LN_2 is used with the operating temperature range (ΔT) of 68 to 78 K, a mass flow rate ($\dot{m}$) of 200 (g/s), and specific heat capacity of (Cp) of 2 (kJ/kg/K), then the maximum heat load of the cable (Q) between the cooling stations can be up to 4 kW. Considering 1 W/m of heat flux for typical HTS cable will give us 4 km, which is the maximum length that the HTS cable can go between the cooling stations. However, calculating the distance between the cooling stations involves other factors such as the pressure drop which should be taken into consideration too. An alternating rigid and flexible sections of the cryostat, which was developed by Chevtchenko [84], is a potential solution to decrease the friction of the inner surface of the cryostat. Furthermore, smooth cryopipes can be proposed to replace all the corrugated sections since the pipes are going to be buried underground and no flexibility is needed for bending them. This will significantly reduce the total friction of the inner surface of the cryostat. On the other hand, the topography can also add complications to the pressure drop consideration when the cable route involves inclined areas. Moreover, since the heat load of the DC cable is solely from the heat leak into the cryostat, the cryostat design is the key factor to increase the distance that HTS cable can go between refrigeration stations. A team of researchers from EPRI led by Hassenzahl have come with a very interesting result of 20 km distance separating the cooling stations which can be achieved with a cryostat design that uses counter-flow, using go and return streams for the LN_2 [85]. A 3 kg/s of mass flow rate and 3.1 MPa as maximum pressure, with allowable 1.0 MPa of flow pressure drop, were developed for the EPRI study to enable the 20 km distance. Finally, it is possible to add cryogenic cooling stations in the middle of cable sections which adds additional flexibility to the system [13].

2.7 Chapter Conclusions

The chapter outlined the opportunities for increasing the efficiency of long-distance electric power transmission systems by using HTS DC power cables. The multi terminal superconducting HVDC transmission systems allow easier integration of diverse power grids and the insertion of distributed renewable sources into the power network. The integration of the grids and renewable

energy sources eliminate the use of fossil fuels for meeting the transient power demands and improve the resiliency of the whole electric power network. There are, however, several technology advancements needed in areas of HTS, cryogenics, and power electronic systems to make the long distance superconducting multi terminal HVDC transmission systems a reality. The technology gaps and possible options for various components of HVDC systems were discussed in this chapter.

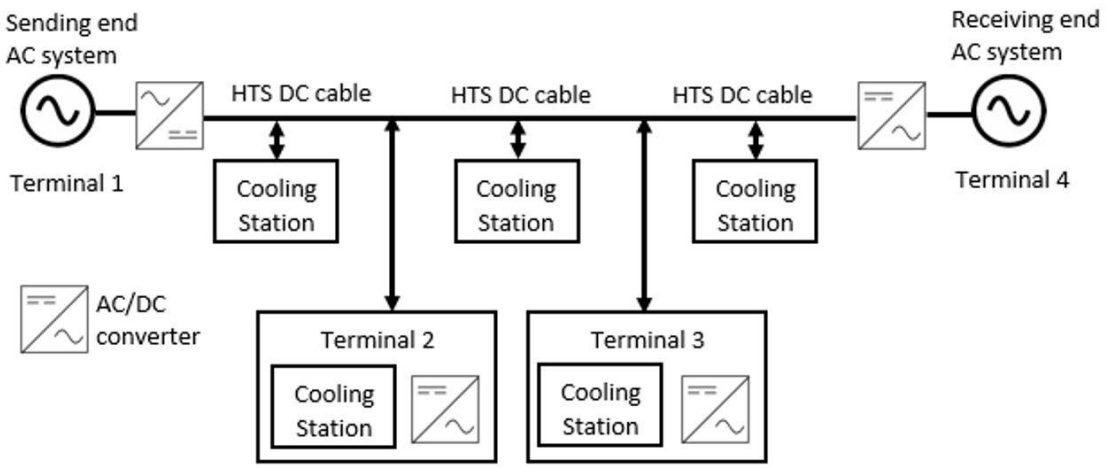

Figure 11: Simplified four-terminal radial MT-HVDC based HTS DC cables with cooling stations scheme

CHAPTER 3

EXPERIMENTAL INVESTIGATION OF INSULATION MATERIALS AND SYSTEMS

3.1 High Voltage Research Facilities

All experimental work in this dissertation was conducted in the high voltage laboratory (HV lab) in Florida State University's Center for Advanced Power System, (FSU-CAPS). The two HV power supplies which were utilized to perform high voltage measurements were a Haefely test kit and a Glassman DC power supply.

The Haefely test kit is located within a Faraday cage, to ensure zero equipotential environment to eliminate any noise that could affect partial discharge measurements. The Faraday cage also provides a physical barrier to the HV equipment. The Haefely test kit includes a 7.5 kVA, 0-100 kV, AC (rms, 60 Hz) transformer, which its primary side is supplied from the 220 V lab outlets through two variac transformers that are connected in cascade, as shown in Figure 12. The first variac is motor driven and is used to adjust the input voltage to the primary side of the main transformer. The second variac is used to alter the voltage step which is provided to the primary side of the main transformer when applying a continuous ramp rate to a device under test. For instance, if the second variac is set to a 2:1 ratio, a voltage step between 300-500 volts ramp up is applied. On the transformer secondary side, the HV components are connected. The transformer is also used as a common grounding point for all HV experiment setups.

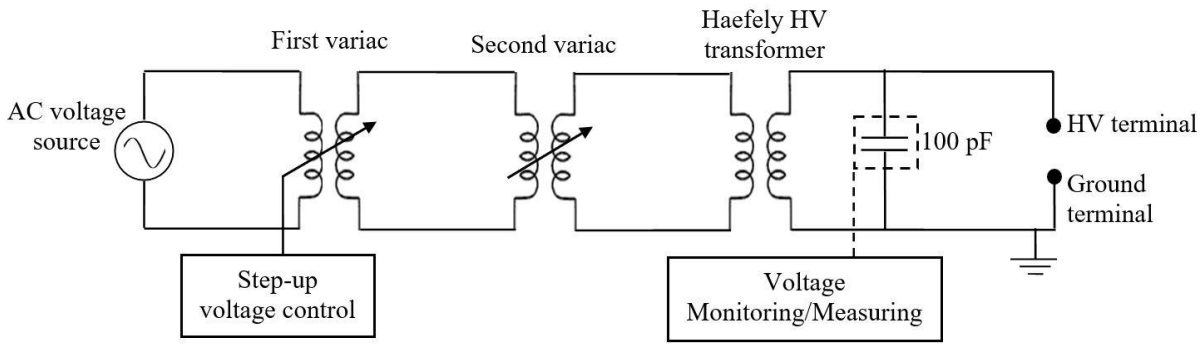

Figure 12: Circuit diagram for Haefely kit high voltage AC experiments

The Faraday cage is divided into two sections, the main section and the extension cage. The main section contains all of the Haefely test kit, and the extension cage contains a cryostat that provides the required environment for cryogenic experiments. For gas pressurized experiments, the pressure vessel is fixed inside the cryostat with the help of the support legs, and the HV connections is fed through the HV bushing mounted on the top plate of the pressure vessel. The cryostat can be filled with LN_2 to provide LN_2 bath cooling to enable experiment setups installed with the pressure vessel to be performed at cryogenic temperatures.

The control, monitoring panel and data acquisition (DAQ) system of the Haefely test kit is located outside of the Faraday cage. It is connected at the same ground potential of the Faraday cage. Voltage measurements from the HV circuit are provided to the DAQ system by including either a capacitive or a resistive divider as part of the circuit. An additional in-house controller was developed which utilizes a raspberry-pi to send a consistent pulse train to the Haefely controller to allow for a uniform voltage ramp rate. The voltage step of the ramp rate can be adjusted by changing the tap position on the second variac as mentioned earlier. The Haefely kit allows all kinds of HV testing techniques, like AC, DC, impulse, partial discharge ... etc.

Figure 13 shows the control, monitoring and DAQ system for Haefely kit outside the Faraday's cage while Figure 14 depicts the experimental setup inside the Faraday's cage and its extension cage.

The Glassman DC power supply is meant for DC experimental setup, has a better DC wave profile (i.e. less AC ripple) compared to the Haefely test kit. In addition, it has the ability to limit the output (discharge) current. Restricting the output current reduces the energy released during a surface flashover which enables more measurements on a sample before degradation occurs. The output current for the Glassman high voltage source was restricted to 2% (3.2 mA). The Glassman facility is a DC HV power supply of 16 kW and offers a range of 0-100 kV DC. The Glassman power supply is located in another cage within the HV lab. This secondary cage is constructed from wood and provides the required physical barrier between HV equipment and personnel within the HV lab. A portable cryostat is used to enable high voltage measurements to be completed at cryogenic temperature. The use of the portable cryostat only allows for small scale experiments to be performed using the smaller pressure vessel in the HV lab. The HV cable of the Glassman power supply connects directly to the HV bushing, and the cryostat is grounded through a wire connection to the Glassman chassis, which is grounded through the lab outlets connection that

delivers the power. The DAQ system is located outside the cage with National Instrument device, as shown in Figure 15, and the monitoring and control is done via a LabVIEW program. Here, the DC voltage ramp rate is also adjustable, and it can be changed via LabVIEW. Figure 16 shows the facilities inside the wooden cage.

3.2 Steps to Achieve High Purity Gaseous Environment for Experiments

Before the start of each experiment, a purification procedure is performed to ensure that the vessel has no impurities/moisture that can adversely impact the integrity of the measurements and experiment reproducibility. Thus, a pre-experiment procedure is done as follows:

Figure 13: Control, monitoring and DAQ system for Haefely kit

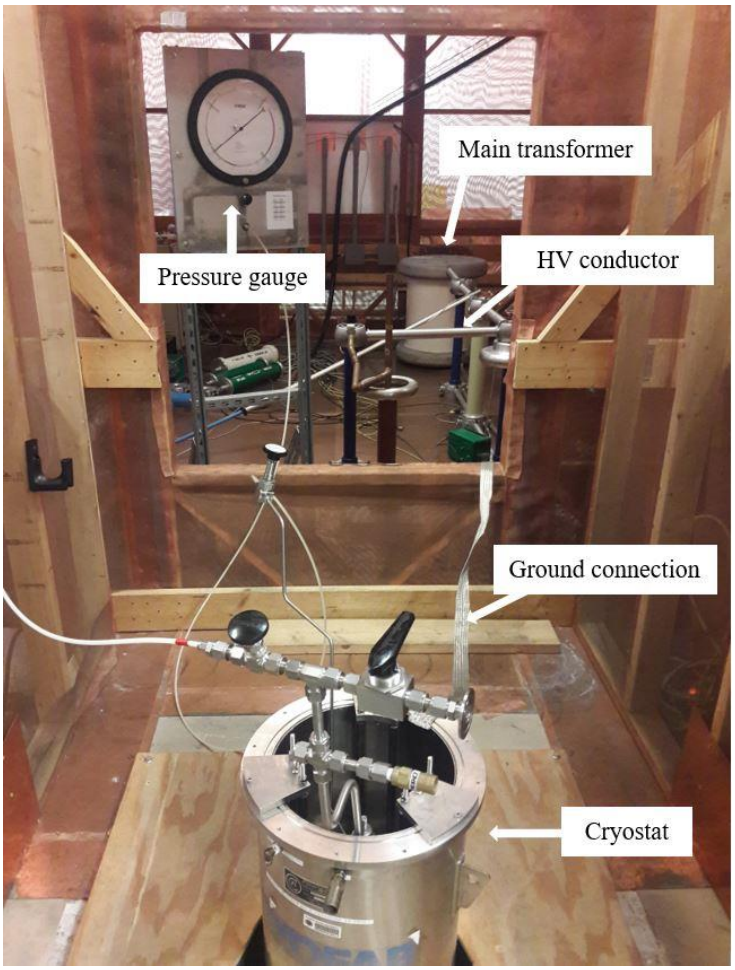

(a)

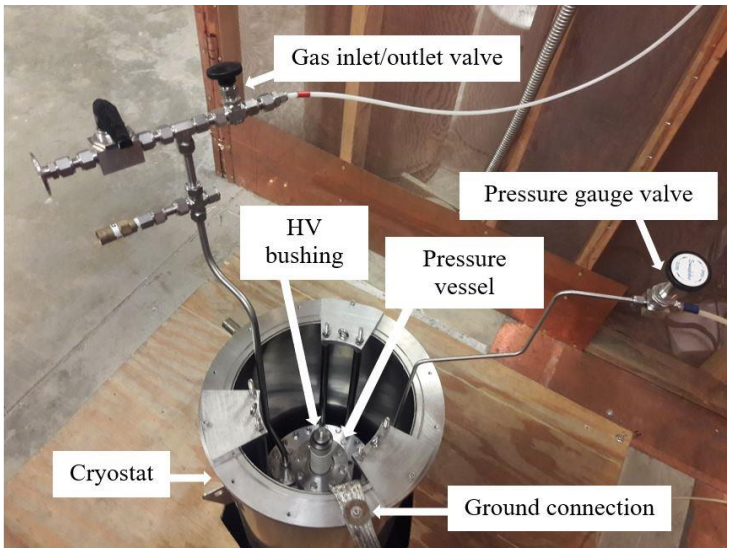

(b)

Figure 14: (a) the experimental setup inside the Faraday's cage and its extension (b) upper view of the cryostat in the extension cage

1- Pressurizing the vessel to 2 MPa with industrial grade of gaseous nitrogen (GN_2).
2- Releasing the gas close to atmospheric pressure, and then evacuating.
3- Pressurizing the vessel to 2 MPa with industrial grade of gaseous helium (GHe).
4- Releasing the gas close to atmospheric pressure, and then evacuating.
5- Pressurizing the vessel to 2 MPa with industrial grade GHe again.
6- Releasing the gas close to atmospheric pressure, and then evacuating.
7- Pressurize the vessel with the gas under investigation.

Pressurizing with N_2 serves two goals. First, its relatively big molecules perform a coarse purification, which helps to remove any impurities in the pressure vessel and on the experimental setup. Second, it absorbs the moisture inside the vessel. The nitrogen gas is left for a while in the pressure vessel for moisture absorption, 30-60 minutes, and this also helps with checking if there is any leak in the system before starting the experiments. Afterwards, pressurizing with GHe twice helps performing a fine purification due to the smaller GHe molecules size.

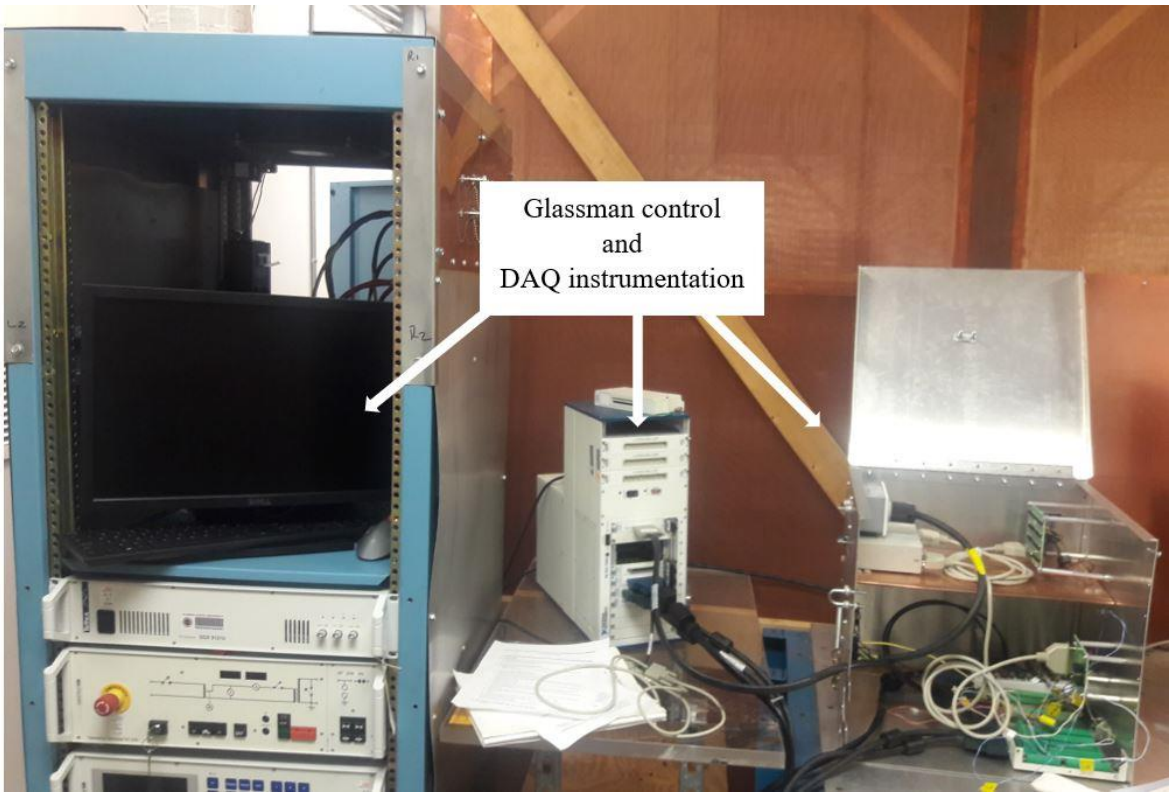

Figure 15: (Left to right) the computer, National Instrument device and DAQ system

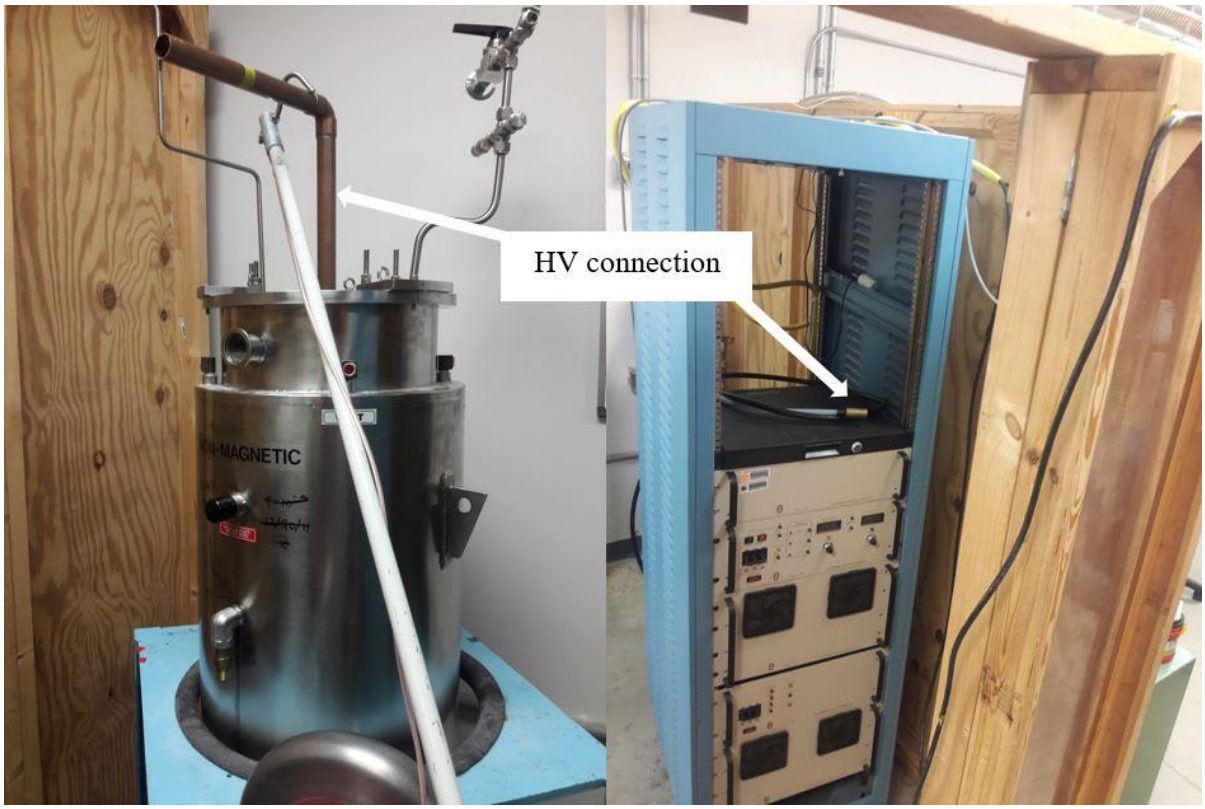

Figure 16: (left) the portable cryostat showing the HV connection coming out of the pressure vessel, which hangs inside (right) Glassman HV facility, the wooden cage, CAPS-FSU

3.3 Challenges in Breakdown Voltage Measurements at Cryogenic Temperatures

To ensure reproducibility and measurement consistency at cryogenic temperatures, it is important that the gas temperature inside the pressure vessel is uniform. Since pressurizing the vessel by adding the room temperature gas results in a momentary temperature increase and releasing the gas to lower the pressure results in a momentary temperature decrease, a waiting time is needed to allow the gas temperature inside the vessel to come back to the measurement temperature of 77 K. It would be helpful if temperature sensors can be used and distributed at difference positions inside the vessel, but it is not feasible in high voltage measurements because the cryogenic temperature sensors do not tolerate a breakdown (BD) event. Another way to track the temperature inside the vessel is through monitoring the pressure. However, a local temperature change due to the released energy in a breakdown event might not result in any noticeable bulk pressure change. To ensure consistency and repeatability of measurements, a waiting time after

each measurement is required to ensure that the data recorded is always at 77 K. The waiting time needed differs based on the amount of energy released which depends on the BD voltage.

A series of experiments were conducted as discussed below to track the temperature change after changing the pressure level and the local temperature increase after a BD event.

3.4 Thermal Equilibrium Experiments

The thermal equilibrium experiments were conducted to establish as the measurement protocol for breakdown voltage measurements in gas media at cryogenic temperature (77 K). Eight temperature sensors (T1-T8) were used at different positions inside the pressure vessel on an emulated HTS cable. An aluminum rod was used to emulate an HTS cable which was screwed to the underside of the HV bushing which is attached to the top flange of the pressure vessel. Besides replicating the typical breakdown voltage experiments on HTS cables, the cable-like arrangement offers monitoring of the temperature gradients along the length of the pressure vessel as the temperature sensors are mounted along the length of the cable. Consequently, three temperature sensors were attached to the top and bottom of the emulated stress cones, and at the center of the cable to track the temperature along the length of the cable or along the height of the pressure vessel. Additionally, with the help of a threaded rod that screwed to the vessel's top plate with a radial distance of 5 cm away from the center axis of the vessel, another three sensors were placed and aligned to the first three sensors. The position of the threaded rod was the closest to the gas inlet/outlet. Another threaded rod, which was installed at 3.8 cm from the first threaded rod, screwed also to the vessel's top plate and provided the support to mount the additional two sensors. A plastic spacer was used to maintain equal distances between the sensors and the emulated cable. With this arrangement, the eight sensors were distributed at three vertical and three radial positions inside the vessel allowing temperature mapping in the pressure vessel. Pressure and temperatures' readings were monitored and recorded using National Instrument equipment with a LabVIEW program. For pressure measurements, a pressure transducer was used. This allowed for pressure measurements to be recorded by the DAQ system simultaneously with the temperature measurements. The eight temperature sensors were connected to a temperature monitoring device (Lake Shore Temperature Monitor - Model 224). The sensors were connected to different channels, four of them to C channels (C2-C5) and the other four to D channels (D2-D5). Figure 17 depicts a schematic for the experiment setup. The connections were facilitated though a feedthrough on the

top flange of the vessel, as shown in Figure 18, to connect the sensors to the temperature monitor with a thermal sealing mechanism. Figure 19 demonstrates the wiring diagram used for the measurements. The LabVIEW program collected the data from the temperature and pressure sensors.

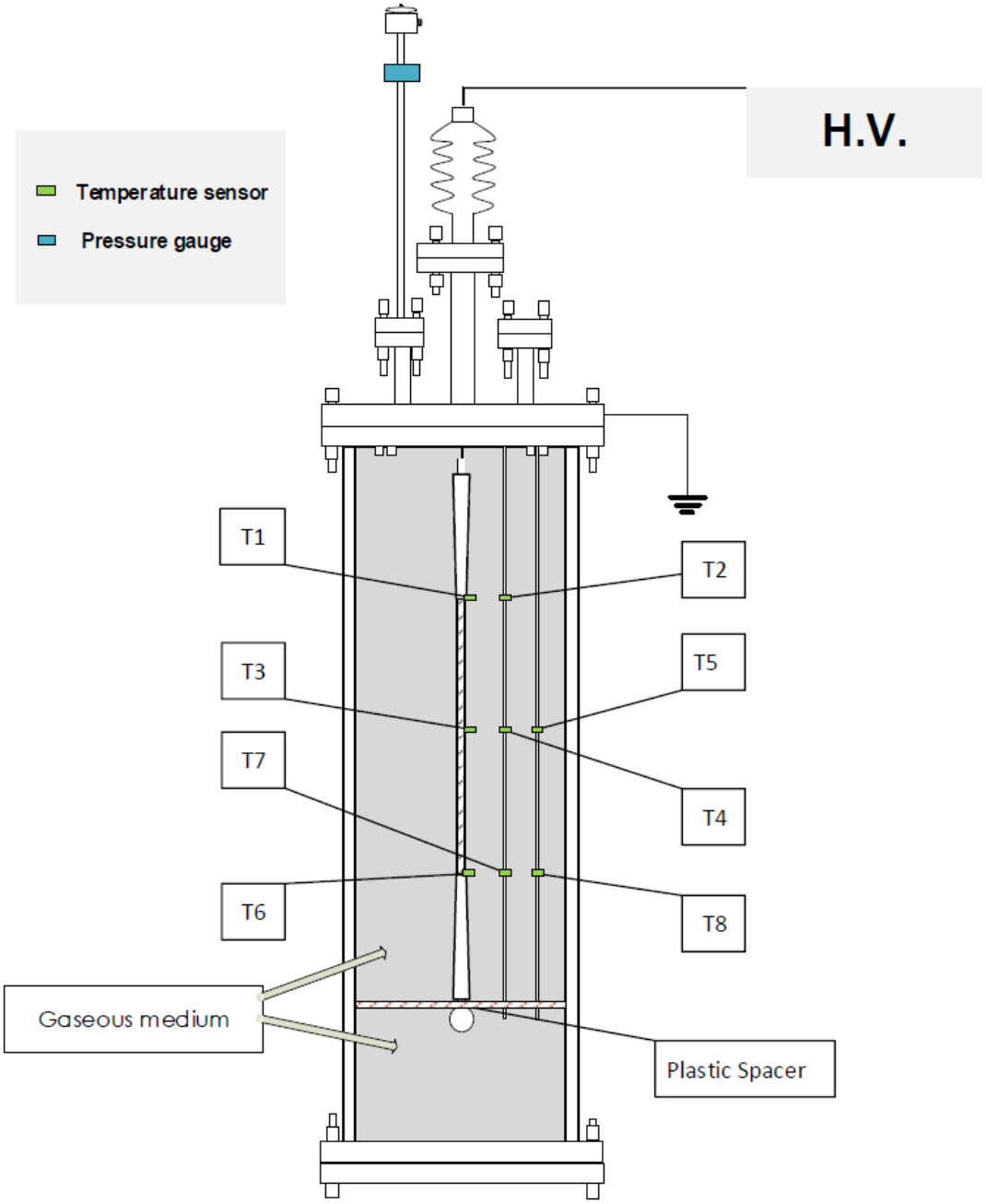

Figure 17: Schematic for emulated thermal equilibrium and the locations of the eight temperature sensors

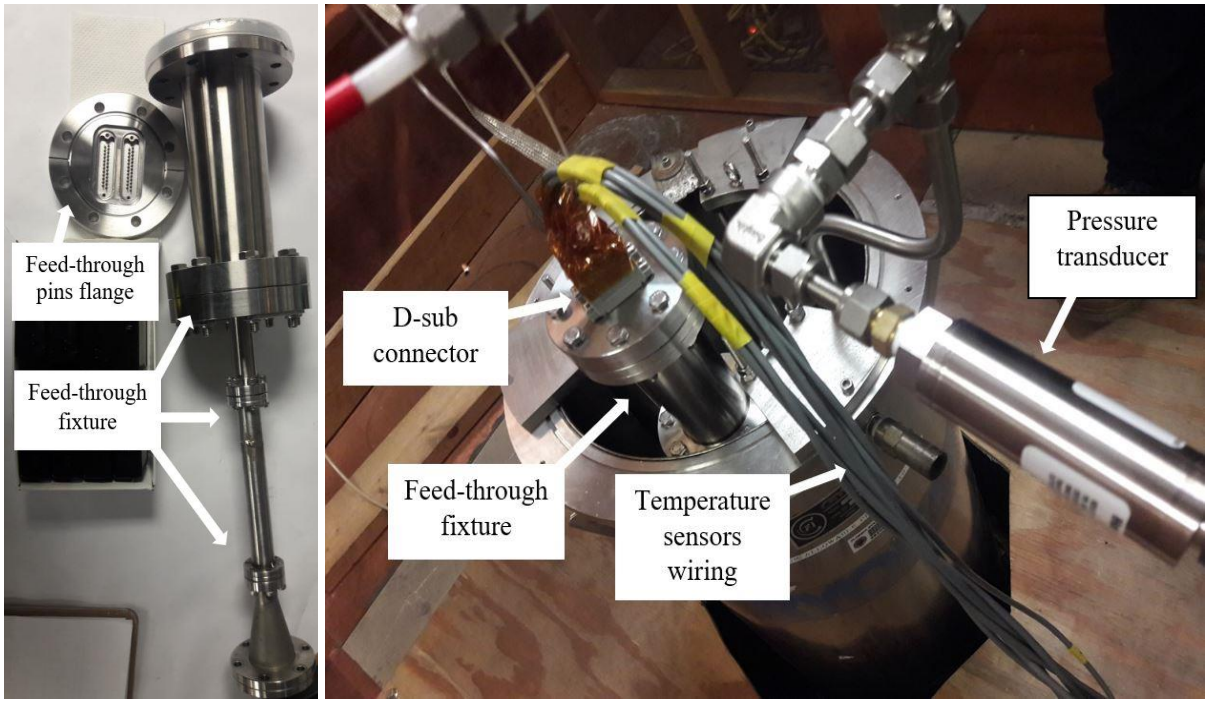

Figure 18: Temperature sensors' wires feed-through experimental setup

3.4.1 Room Temperature Experiment

Although the characterization of the HTS devices requires experiments at cryogenic temperatures, room temperature experiments shed light on the materials and designs. Thus, thermal equilibrium experiment was performed at the room temperature to improve and validate the experimental protocols.

Starting from almost zero pressure, after establishing vacuum, which is the last stage of the pre-experiment process to achieve pure gas environment, GHe was filled to pressurize the vessel to 2 MPa. Adequate time was allowed for temperature to stabilize. Then the pressure was adjusted to 1.5 MPa by releasing the gas. This time, the temperature decrease due to release of the gas was of interest. The process was continuing to achieve the other pressure levels that are usually used in the high voltage measurements. They are 1 MPa, and 0.5 MPa. Thus, releasing the gas and waiting process is repeated twice afterwards. The pressure and temperature readings are shown in Figure 20. Data from temperature sensors T1-4 and T5-8 are plotted separately for clarity.

The data shown in Figure 20 allowed to make the following conclusions:

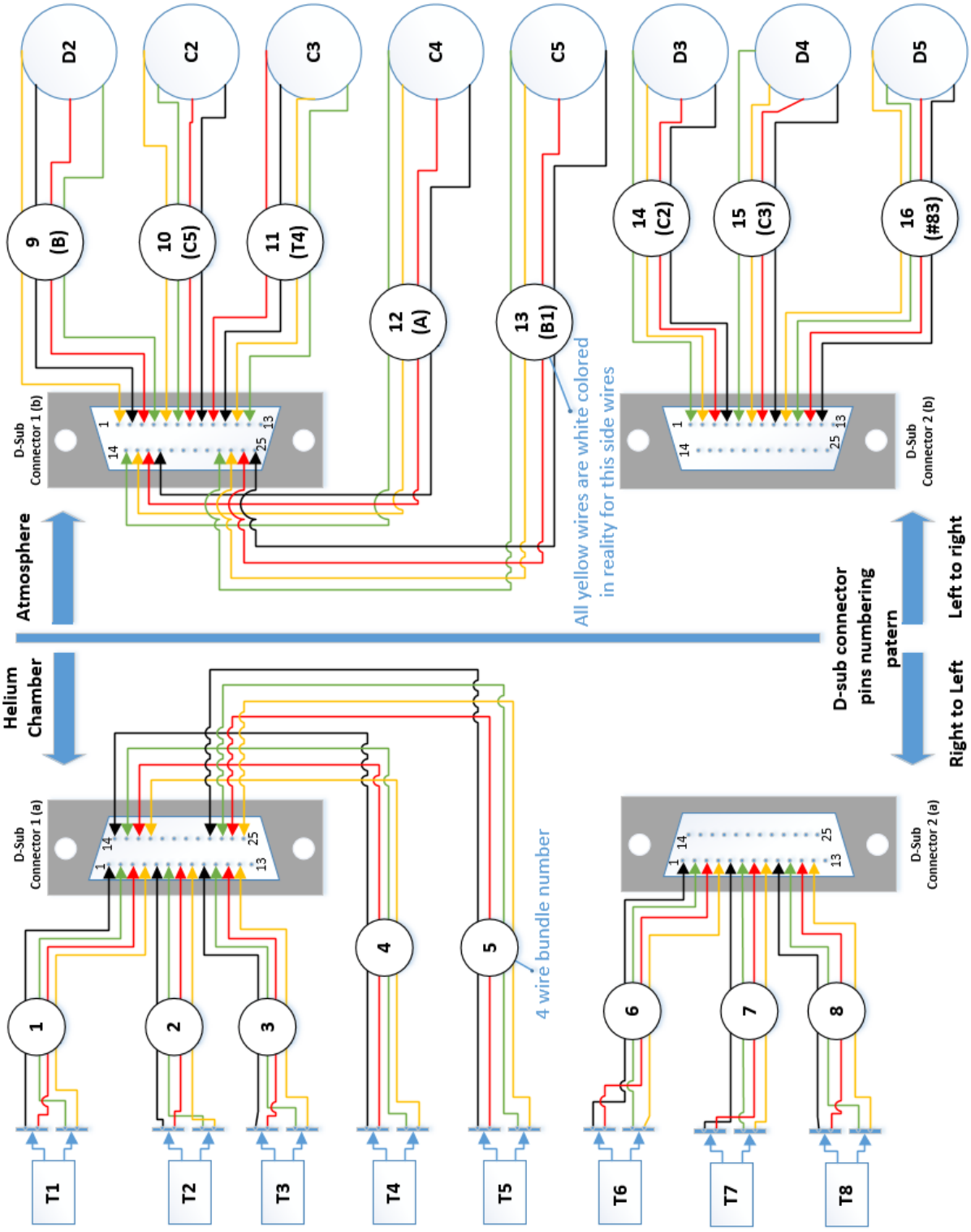

Figure 19: Wiring diagram showing all the temperature sensors (T1-8) and the wire connections to the monitoring channels (C2-5 and D2-5)

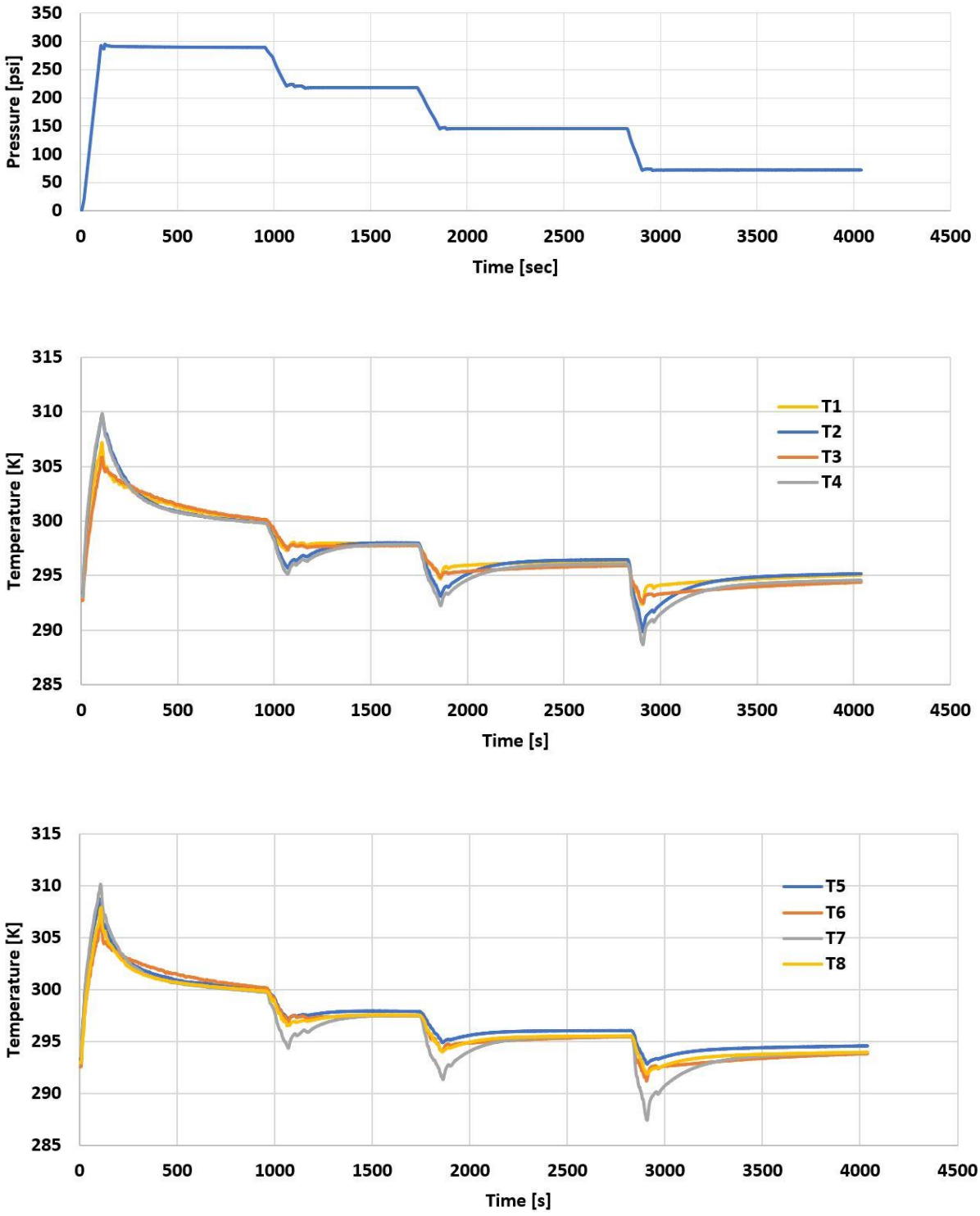

Figure 20: Pressure and temperatures during pressurization of GHe from 0 to 290 psi (2 MPa), and releasing it to 217.5, 145, 72.5 psi in room temperature experiments

- The pressure change affects the temperature as was expected. For large changes in pressure, such as filling the empty pressure vessel to 2 MPa, it is better to follow the pressure change using the sensors in positions close to the gas inlet/outlet. These were the sensors T2, T4 and T7. Since pressurizing results in an increase in temperature, after the inlet is closed and the temperature gets equilibrated, the pressure drops and requires adding to adjust the pressure to 2 MPa. The two peaks in the pressure around the 2 MPa (290 psi) are not tracked by all the temperature sensors, suggesting local temperature differences. This suggests the difficulty in using the bulk pressure measurement as a surrogate of the temperature. This is particularly important when the local temperature around the gap between the electrodes increases due to a deposition of energy in a breakdown event.
- It takes many steps of small additions of gas to get the pressure to the desired level. This has been noticed during many previous experiments, and this phenomenon is worse in the experiments at cryogenic temperatures, as will be shown in the next subsection.
- Pressurizing from almost zero pressure to 2 MPa, which is a big pressure difference, resulted into a significant rise in the gas temperature (around 17 K), and it takes a long time for the temperature to return to the initial temperature.
- A waiting time of around 300 seconds was enough for the temperature to reach a stable point after releasing the gas. Hence, 5 minutes waiting time is suggested after any pressure release process in the experiments.

3.4.2 Experiments at Cryogenic Temperatures

The start point here is different than the room temperature experiment. Cooling the gas from room temperature to 77 K causes a pressure drop which is at the same ratio of temperature drop, approximately 3.7 times. Accordingly, usually the vessel is pressurized to 2 MPa, then LN_2 is added into the cryostat. The pressure drops to approximately 0.5 MPa. Thus, as shown in Figure 21 for experiments at 77 K, the starting point is close to 0.5 MPa (78 psi). That is also the reason for the x-axis (the time scale) to start from the second 1970 in Figure 21 since the previous mentioned process of pressurizing and adding LN_2 to reach 0.5 MPa at 77 K takes the time from zero to 1200 s, 20 minutes.

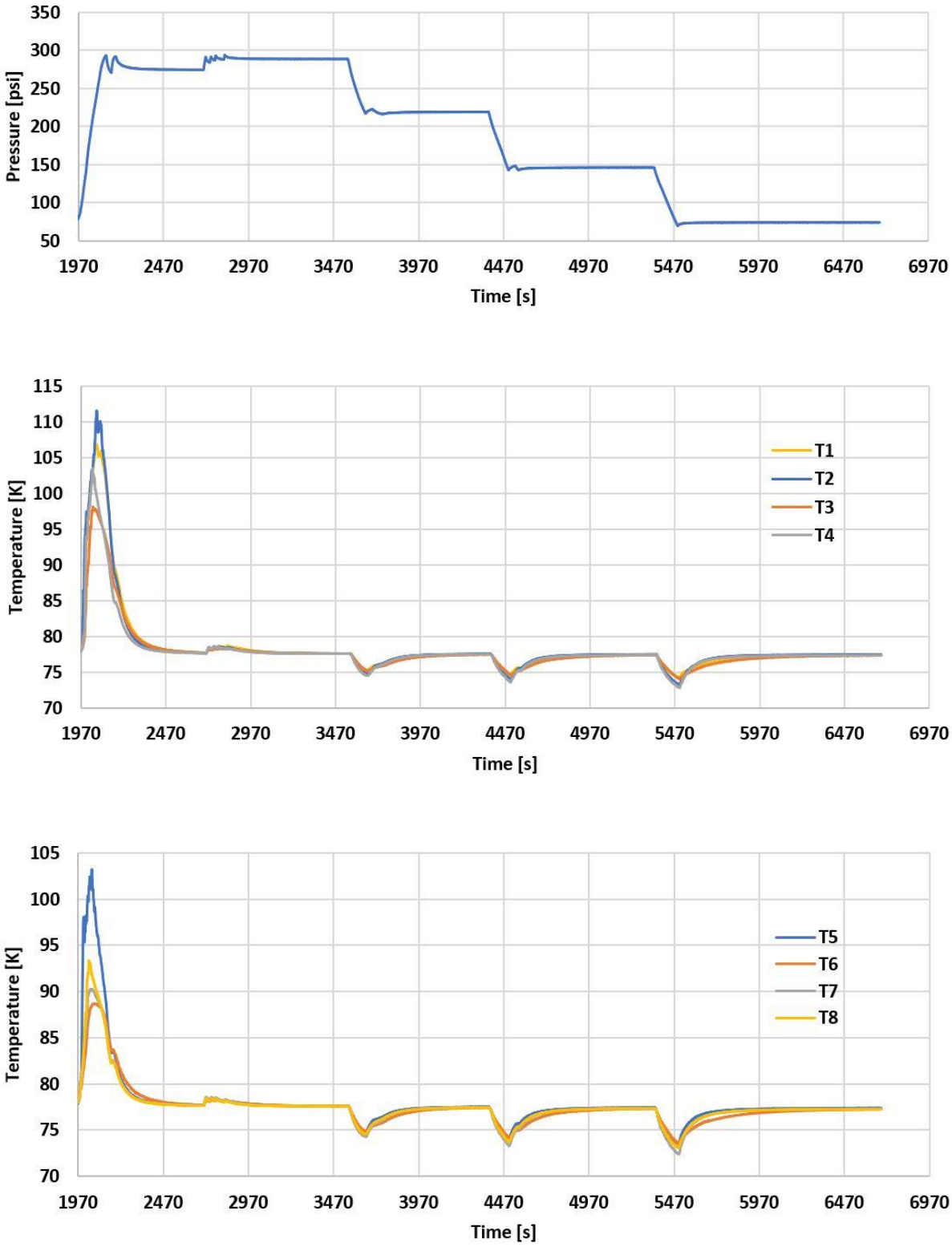

Figure 21: Pressure and temperature data for pressurizing GHe from 78 (0.5 MPa) to 290 psi (2 MPa) followed by releasing it to 217.5, 145, 72.5 psi at 77 K

The time from 1200 to 1970 s, approximately 13 minutes, was just another waiting time to check that no change happens to thermal equilibrium.

The experiments at 77 K led to the conclusions similar to the room temperature experiments, except the following:

- Here, the temperature sensors that were mostly affected by pressure change were the ones that are installed at the highest vertical level inside the vessel and close to the gas inlet/outlet. The sensors T1 and T2 showed the highest temperature rise of 34 and 29 K, respectively. Then, T4 and T5 with a temperature rise of 25 K, and T3 with 20 K. The temperature sensors T6-8, which are the bottom level, showed lower temperature rise in response to gas pressure increases. However, for releasing the gas, same scenario as for room temperature experiments was noticed. Therefore, pressure change was better followed by sensors in positions directly affected by the gas inlet/outlet. These were the sensors T2, T4 and T7, which were mounted on the first threaded rod.
- It took the gas around 500 s, to settle at 2 MPa when pressurizing from 0.5 MPa at 77 K since the added gas was from the tank at room temperature. Adding this time to the required time to reach 0.5 MPa at 77 K when starting form room temperature and vacuumed vessel, which is 20 minutes, gives a total of approximately 28 minutes for the whole process. The waiting time after pressurizing is around 300 s for temperature to settle back to 77 K. In addition, it took 400 s to reach the thermal equilibrium from the start of gas release process to decrease the pressure to the next lower level. Accordingly, the waiting time suggested after releasing the gas is around 200 s.
- More pressure fluctuations are observed when pressurizing to 2 MPa since the incoming gas is at room temperature before entering the 77 K vessel.
- The temperature gets back to its start point of 77 K, due to the presence of liquid nitrogen outside the pressure vessel.

3.5 Breakdown Emulation Experiments

To estimate the waiting time required after aa BD event, the temperature sensors were relocated close to the BD point to track the temperature evolution with time. As mentioned earlier, the actual BD cannot be performed because it will damage the cryogenic temperature sensors. Instead, emulating the amount of power/energy (in the form of heat) released during a breakdown

is used as an alternative to study the local temperature variations. A resistive heater wire connected to a controlled power supply was used as the source of heat.

3.5.1 Energy Release Calculation

The manuals for Haefely kit and Glassman high voltage test facilities do not state the wave form of the discharge current to estimate the amount of energy in a breakdown event (E_{BD}). Using the capacitor value, which is 25,000 pF, of the DC experimental setup, the stored energy in the capacitor (E_{Stored}) can be calculated by the following equation:

$$E_{Stored} = \frac{CV^2}{2} \tag{8}$$

where V is the capacitor voltage and C is the value of the capacitor used in the DC circuit. When breakdown happens, the capacitor discharges its stored energy. Thus, E_{BD} equals E_{Stored}, and capacitor voltage equals the breakdown voltage (V_{BD})

Table 3 shows the energy released in breakdown events at various voltage values. It was decided to choose 5 J of breakdown energy in emulated experiments since 20 kV range represents the typical breakdown voltage in our experiments.

Table 3: Breakdown energy released for each breakdown voltage

Breakdown Voltage (kV)	Breakdown Energy (J)
10	1.25
20	5*
30	11.25
40	20
50	31.25**
60	45
70	61.25
80	80
90	101.25
100	125

* breakdown energy that was taken into consideration.

** maximum breakdown energy that can be achieved in our experiments due to the limitation of the experimental setup.

3.5.2 Heater Wire Length Calculation

The emulation was done through using a cryogenic heater wire wound around the HTS cable. With the use of the current source, 1 A current can supply the cryogenic heater wire to generate the same amount of heat released by the actual breakdown. To find the required resistance (*R*), in Ohms, to emulate the amount of the worst-case breakdown energy release, the following equation is used:

$$R = \frac{P}{i^2} \tag{9}$$

Since the 5 J of energy has been chosen, and the current source is supplying only 1 A, the required resistance for the heater wire should be 5 Ω when the current pulse is for 1 second.

The length of the wire needed to achieve the required wire length can be calculated from the following equation according to the resistance per meter length of each wire type.

$$Wire\ length = \frac{R}{R\ per\ unit\ length} \tag{10}$$

A Nichrome (32 AWG) Lakeshore Cryotronics Inc. cryogenic heater wire was used. Its resistance per unit length is 33.4 Ω/m at 77 K. Thus, the heater wire length needed with a 1 A current is 15 cm to achieve the targeted 5 W of power.

3.5.3 Experimental Setup and Results

The tubular insulator S-GIL cable experimental setup was used since the S-GIL design is going to be tested and characterized experimentally. The cable was inserted inside the grounded copper tube and insulator tubes snugged in between (details of bundled tubes S-GIL design are discussed in Chapter 5). Figure 22 shows the experimental setup and sensors locations. BD emulation cryogenic heater wire was wound around the HTS cable, and the temperature sensors were placed at different locations, (T1) 1 cm above, (T2) 2 cm above, (T3) 1 cm below the heater wire, (T4) and (T5) on a higher vertical levels on the cable at 10 cm and 20 cm above the heater wire, respectively, (T6) inside one of the PTFE insulator tube next to the heater wire, (T7) inside another PTFE insulator tube and 1 cm above the heater wire vertical level, (T8) outside surface of the copper tube, as shown in Figure 22.

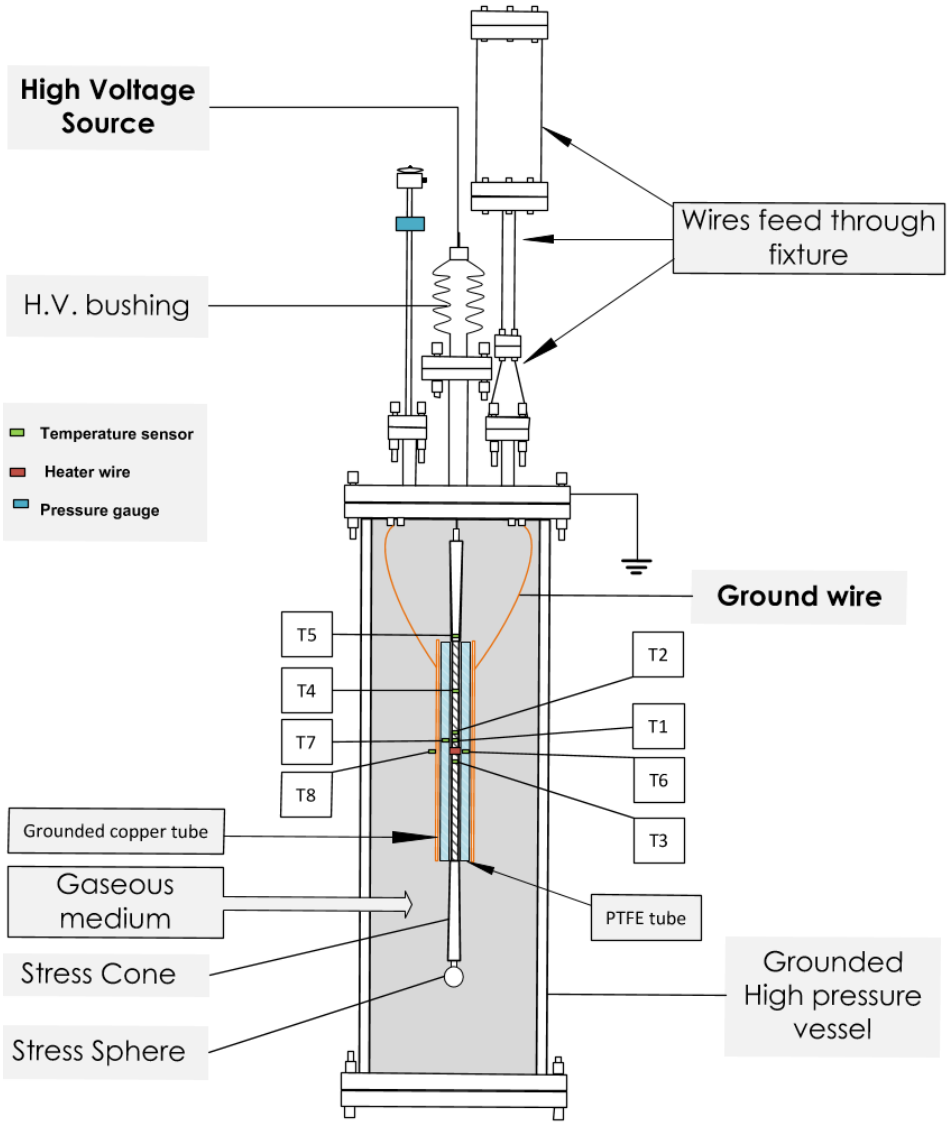

(a)

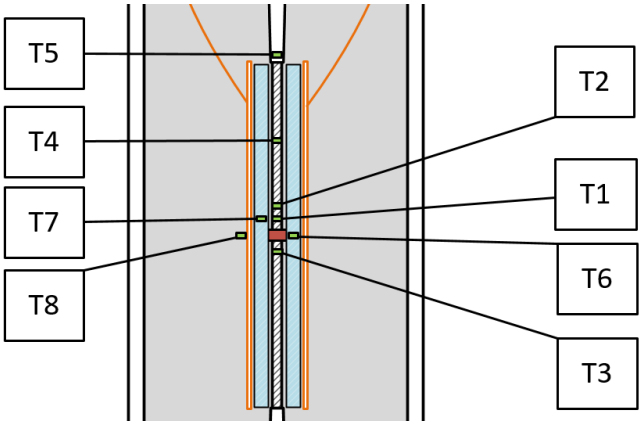

(b)

Figure 22: (a) Breakdown emulation experiment setup (b) closer view for sensors locations

Two heater wires were connected in parallel and wrapped around the cable. The reason for using two parallel wires is for redundancy in case one of the wires fails. Replacing the wire would require disassembling and assembling the experimental setup. Thus, two 30 cm wires were connected in parallel to achieve the 5 Ω required resistance. The heater wire was supplied by a current source with two wires fed through the vessel. Another two wires were used for voltage measurements. The current ON/OFF control was done manually. Monitoring and recording data was automated using LabVIEW.

During the experiments, one of the parallel wires got detached, so the resistance of the heater became 10 Ω. Accordingly, the source current was reduced to 0.5 A, and the pulse width was increased to 2 sec to achieve the targeted 5 J of energy release.

Figure 23-26 show the temperature data of the sensors for pressure levels of 0.5 to 2.0 MPa, respectively. T1-4 and T5-8 sensors were plotted separately for clarity.

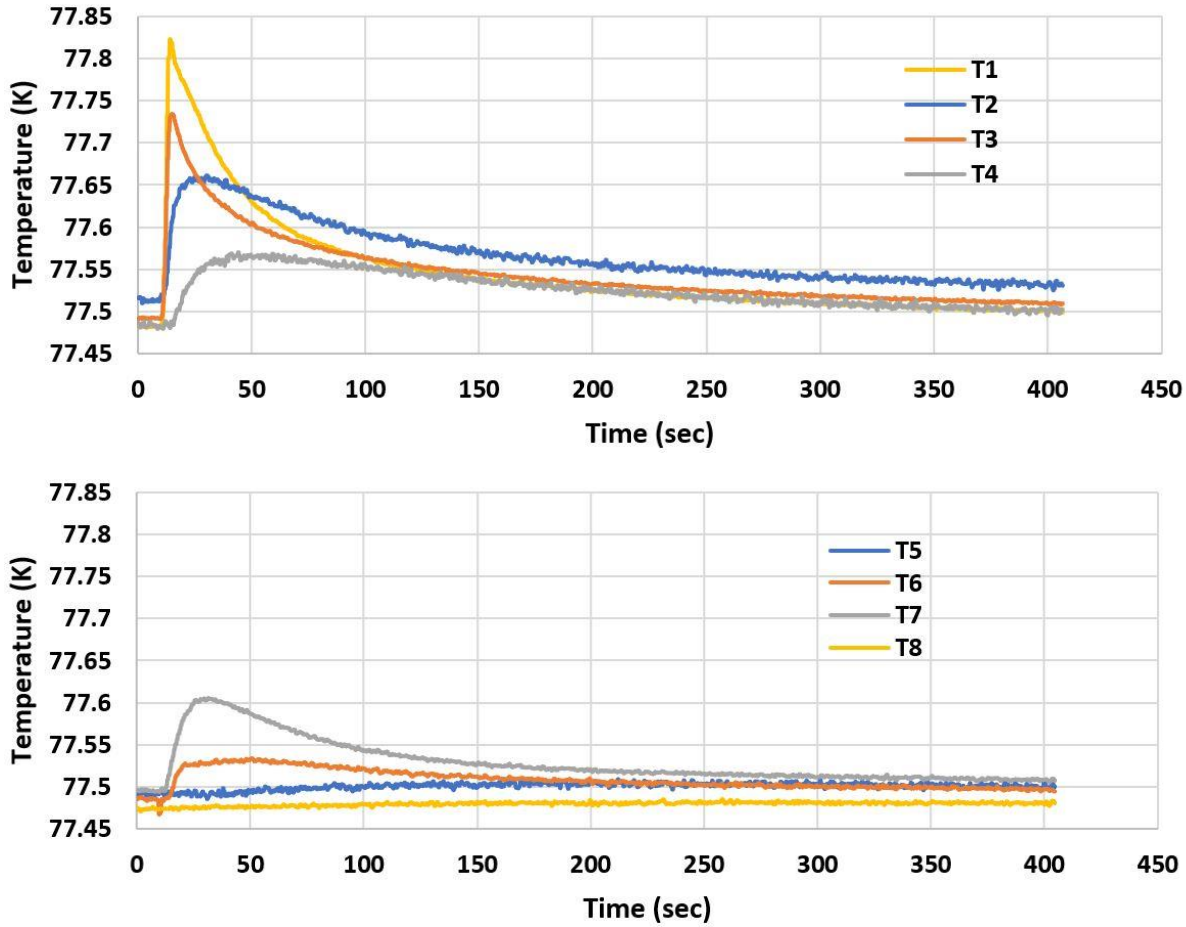

Figure 23: Temperature sensors readings at 0.5 MPa in emulated BD event

Analysis of the data showed that there exists a temperature gradient after BD heat release. However, it was almost the same for all four pressure levels except that for T1 (1 cm above the heater wire). T1 peak increased with the increase of pressure level. It reflected a rise of approximately 0.3, 0.4, 0.5 and 0.6 K for pressure levels of 0.5, 1.0, 1.5 and 2.0 MPa, respectively.

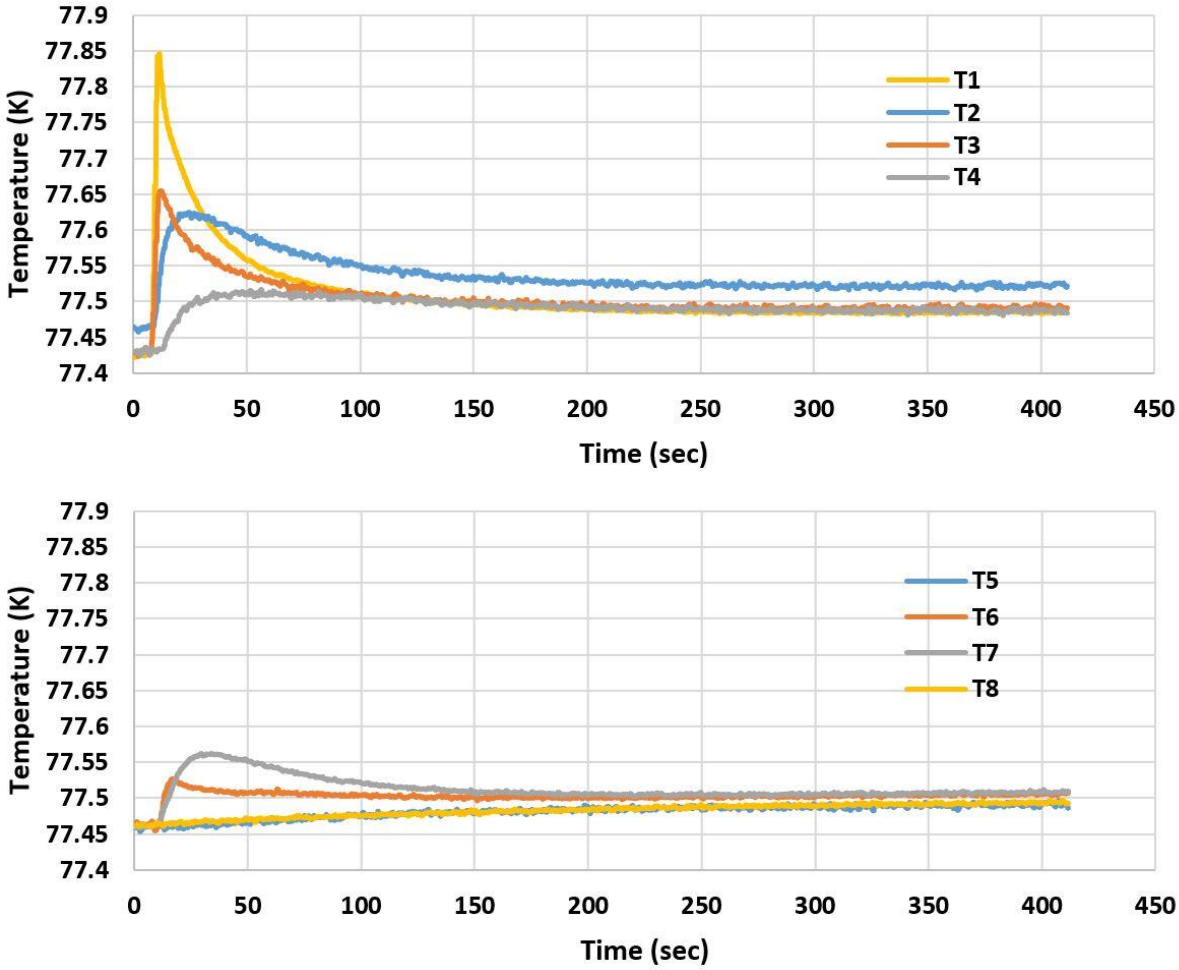

Figure 24: Temperature sensors readings at 1.0 MPa in emulated BD event

The temperature sensors surrounding the heater wire recorded the most temperature increase since they are very close to the local heat deposition. The results showed that the highest change in temperature occurred instantaneously at the closest sensors to the heater wire, which are T1 (1 cm above the wire), and T3 (1 cm below the wire), with a value of approximately 0.2 K. At these two locations temperature enhancement dissipates fast, and their temperature tracking shows sharp peaks. Then, T2 (2 cm above the wire) peaks approximately 5 s after first two peaks and

takes longer to come down. This comes from the fact that the heater was turned on for 2 s. The results also showed that the heat keeps going upward towards T4 (10 cm above the wire) demonstrating a delayed 0.075 K peak. However, most of the heat dissipates before reaching T5, which sits 20 cm above the wire, so almost no change in temperature observed at that location.

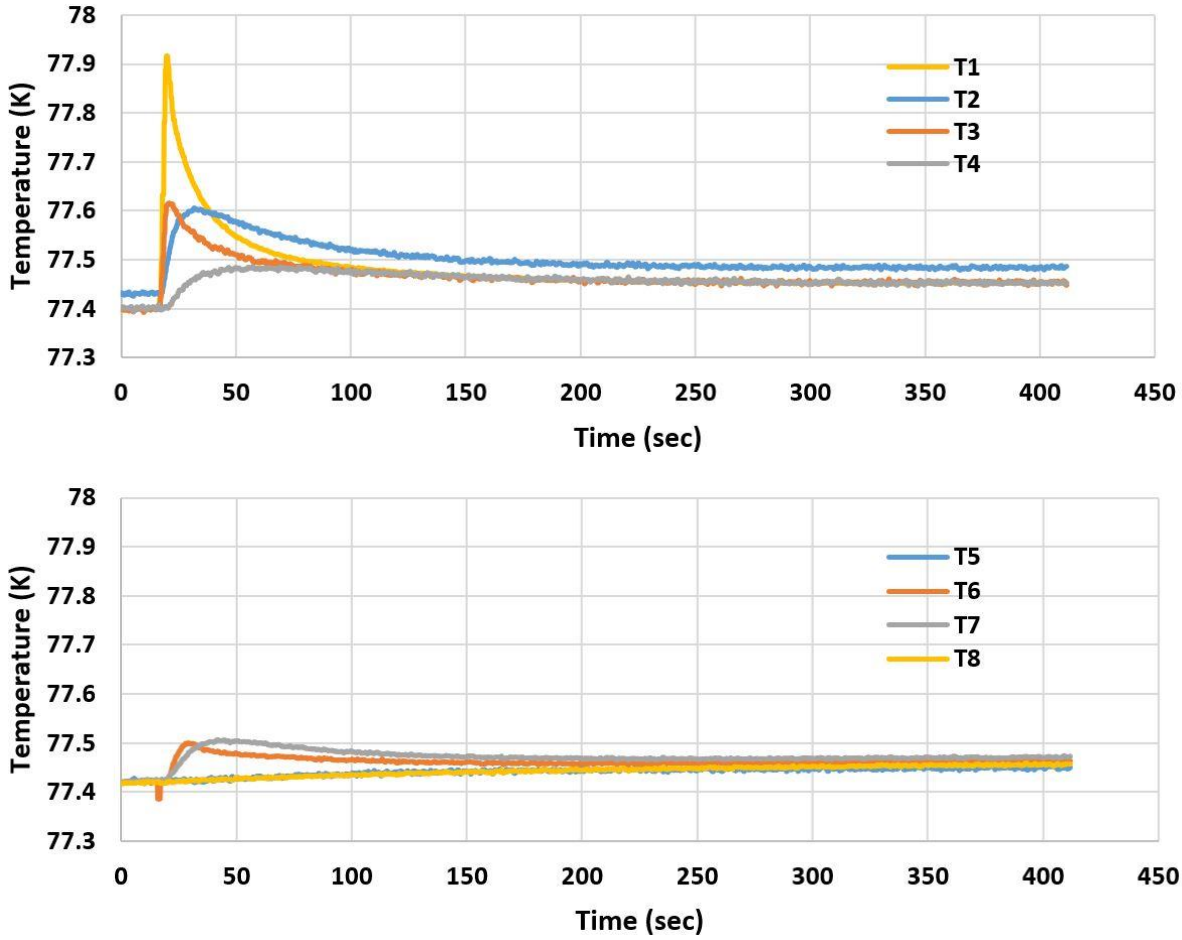

Figure 25: Temperature sensors readings at 1.5 MPa in emulated BD event

For the rest of the sensors, T6 (next to the heater wire but inside the PTFE tube) sensed a small peak of approximately 0.05 K since the PTFE acts as a thermal insulation while T7 sensed a peak value of 0.1 K since it sits 1 cm higher than T6 in another PTFE tube. Finally, T8 does not sense any temperature change while sitting on the outer side of the copper tube. Again, all these results were almost identical regardless of gas pressure level inside the vessel except T1.

In general, the time required after a BD event for dissipating the local heat enhancement and reaching the original temperature was 2-3 minutes for all the locations. These results support

the waiting time that was built into our experimental protocols based on our experience in BD measurements at cryogenic temperatures.

Finally, although that the difference in temperature is very low, approximately 0.025 K, T2 temperature does not reach the rest of the sensors. Calibration and accuracy errors could be the reason behind that. These two were also responsible for the slight differences in the start temperature of the sensors.

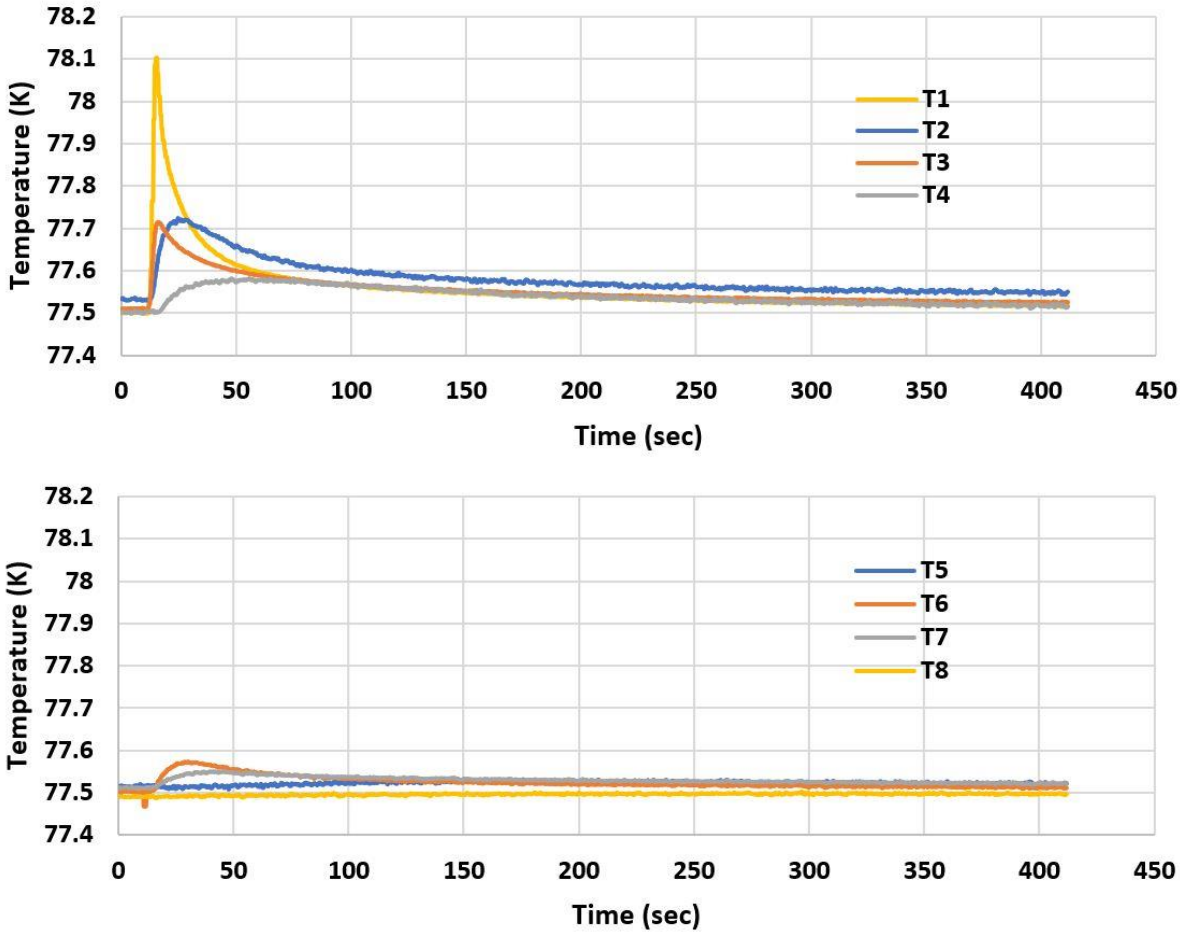

Figure 26: Temperature sensors readings at 2.0 MPa in emulated BD event

3.6 Chapter Conclusions

The experimental facilities in the high voltage laboratory at the Center for Advanced Power Systems, Florida State University (FSU-CAPS) used for the dissertation work are described. Capabilities of the high voltage lab facilities, lab equipment and methods of performing

measurements are discussed. The ability of conducting experiments at room temperature and cryogenic temperatures is a useful feature that benefited the research work. Furthermore, the pre-experimental process to achieve high purity gas environment is described.

Performing cryogenic high voltage experiments involves challenges regarding to tracking temperature inside the gas vessel during pressurizing/releasing the gas and during and after a breakdown event. Assumption that temperature tracking can be achieved by tracking pressure has been investigated for the two events by performing a set of controlled experiments. The first set of experiments investigated required waiting time to achieve thermal equilibrium after gas pressurizing/releasing, and the second investigated the required waiting time to dissipate local temperature enhancement caused by a breakdown event. Results showed that global vessel temperature can be tracked by global vessel pressure, but the local temperature changes cannot be tracked by global pressure. Accordingly, at room temperature, at least 10 minutes of waiting time is required after pressurizing to 2 MPa while it needs 5 minutes after releasing the gas. For cryogenic temperature experiments at 77 K, 5 minutes of waiting time is required after gas pressurization step and approximately 3 minutes after a gas release step to achieve thermal equilibrium inside the pressure vessel before performing the breakdown voltage experiments. Finally, 2-3 minutes of waiting time is required in between successive breakdown measurements to obtain measurements consistency.

CHAPTER 4

A NEW REPRESENTATION OF PASCHEN'S LAW SUITABLE FOR VARIABLE TEMPERATURE POWER APPLICATIONS

4.1 Introduction

Gaseous dielectric insulation systems used in electrical power devices encounter operating temperatures that range from high temperatures of several hundred degrees Kelvin to low temperatures close to absolute zero. High temperatures are often encountered in wide band gap power electronics and cryogenic temperatures are encountered in helium gas cooled superconducting devices [86], [87]. The wide range of possible operating temperatures make it important to develop methods to estimate the dielectric strength of gas media over a wide range of temperatures. CIGRE has recognized the need and initiated a working group that has been preparing a report to summarize the existing knowledgebase of electrical insulation systems for cryogenic temperature superconducting power devices [88]. High temperature superconducting (HTS) power devices are being developed for power grid, aerospace, shipboard, data centers, and high energy physics applications as they offer significantly higher power density and efficiency compared to conventional copper devices [2], [7]–[10], [89]. One of the appeals of HTS technology is its ability to achieve high power densities at low and medium voltages as the achievable current density is very high [2]. HTS materials operate at cryogenic temperatures maintained by circulating cryogenic liquid or gas media. Liquid cryogens such as nitrogen and gaseous cryogens such as helium and hydrogen have been utilized for superconducting power applications and are being considered for large superconducting power systems [8]–[10]. Liquid cryogens pose safety hazards in some applications and limit the operating temperature to narrow windows [90]. Gaseous cryogens allow larger operating temperature windows, and thus greater design flexibility for HTS power applications. Additionally, the ampacity and power density of HTS devices are functions of temperature and increase significantly with lowering the operating temperature. Larger operating temperature windows allow a stream of circulating cryogenic gas to cool multiple devices in series with successively higher operating temperature before transferring the gas to cryogenic refrigerator, thus reducing the complexity and cost of the system compared to a single cryogenic system per device [91].

For the power sector, there are no recommended design guidelines and industry standards to facilitate widespread application of HTS technology. Information on suitable electrical insulation systems for HTS devices that operate at cryogenic temperatures is sparse. The limitation is particularly restraining for gas-cooled HTS devices because it is a relatively new area and the dielectric strength of a gas medium is a function of the density, which in turn is a function of the operating temperature and pressure. The conventional method for determining the dielectric strength of gas medium is commonly known as the Paschen's curve, which provides the dielectric strength as a function of the product of the gas pressure and gap distance. However, this way of presenting the data often does not provide a practical way to design gaseous dielectric systems because the pressure alone does not represent the dielectric strength without already knowing the operating temperature [92], [40]. Therefore, a more practical and user-friendly method for representing Paschen's law is proposed. The new representation presents the dielectric strength as a function of the mass density and gap distance product, instead of the product of the gas pressure and gap distance in the standard Paschen's law. The new representation is motivated by the knowledge generated by our research during the past 5 years that the dielectric strength of a gaseous helium is a function of its density; the dielectric strength of a gas medium of a given density is independent of temperature and pressure [93].

To find the gas mass density, the ideal gas law is used first to calculate particle mass density (N/V) as:

$$\frac{N}{V} = \frac{p}{k_B T} \Leftrightarrow \rho = \frac{p \cdot m}{k_B T} \tag{11}$$

where N is number of particles (atoms or molecules) of the gas, V is the volume, p is the pressure, k_B is the Boltzmann constant, and T is the temperature in Kelvin. Multiplication of N/V by the mass of the gas particle yields the gas mass density.

4.2 Townsend's Mechanism and Paschen's Law

The ignition (breakdown or sparking) voltage in gases can be found analytically using Paschen's law depending on distance, and pressure when the temperature is kept constant. Estimating the ignition voltage is based on Townsend's discharge mechanism, which is valid for uniform (or weakly non-uniform) and space-charge-free electric fields. Townsend's mechanism states that a primary electron, which was emitted by different energy sources (like photoelectric,

thermionic or collision emission from the cathode) causes the ionization process to be accelerated by the electric field to accumulate ionization energy to start electrons' avalanche that leads to the discharge. The ignition condition for Townsend's mechanism requires the primary electron to regenerate one secondary electron (new primary electron), at least, by feedback process (i.e. avalanche impact) at the cathode to restart the next avalanche, and so on, to maintain consecutive avalanches and form a highly conductive channel between the electrodes [27]. Accordingly, the ignition condition is formulated as:

$$\gamma(e^{\alpha d} - 1) \geq 1 \tag{12}$$

where α is Townsend's first ionization coefficient, γ is Townsend's second ionization coefficient (feedback coefficient or surface ionization coefficient), and d is the gap distance between the electrodes or the different potential conductors/metals. The Townsend's first ionization coefficient is proportional to the electric field and gas density. However, it is commonly derived to pressure instead of density, which is valid when the temperature is constant. Thus, α is a function of electric field intensity and pressure, as:

$$\alpha = A\ p\ e^{-\left(\frac{B}{E/p}\right)} \tag{13}$$

where A and B are Townsend's first ionization coefficient constants, p is the gas pressure, E is breakdown electric field, which is equal to V_{bd}/d, and V_{bd} is the breakdown voltage. Note that the above equation is an approximation for Townsend's first ionization coefficient. Additionally, it is important to mention that this equation is not valid for high electron-affine gases, such as sulfur hexafluoride (SF_6), and to a lesser extent oxygen (O_2) and carbon dioxide (CO_2), in which electron attachment to gas molecules needed to be considered since it leads to higher breakdown voltages. In that case, an electron attachment coefficient (η) should be subtracted from (α) to obtain the effective ionization coefficient (α_e) to establish realistic estimations of the breakdown voltage values [27], [94].

Now, substituting (13) in the equality case for (12) and solving for E, and consequently for V_{bd} yields the approximation equation of Paschen's law:

$$V_{bd} = \frac{B \cdot pd}{ln\left(\frac{A \cdot pd}{ln(1 + 1/\gamma)}\right)} \tag{14}$$

Regarding the range of validity (i.e. the higher and lower *pd* values that the approximate equation derives is valid), the approximate equation is applicable for space-charge-free discharges where the electric field is not distorted significantly by the space charges generated due the avalanches of the discharge and uniform field. Thus, the higher limit of V_{bd} is limited by transition to space-charge-dominated region where the streamer discharge model becomes valid. The transition region is limited by αd = 14-18 [27]. For the lower limit of V_{bd}, the breakdown approximation equation does not describe the breakdown physics for low-pressure/low-distance values accurately. When *pd* asymptotes to zero, the theory states that V_{bd} should keep increasing to infinite values due to the lack of sufficient gas molecules ionization because of short-distances/low-pressure conditions, which prevents the growth of electron avalanche. However, in reality, V_{bd} does not increase infinitely due to field emission. On the low *pd* ranges, Townsend's mechanism consecutive avalanches model is no longer valid, and the situation is described by the vacuum breakdown.

Regarding the constants in the breakdown approximation equation, choosing the appropriate values for *A* and *B* results a good estimation for V_{bd} that agrees with the experimental results. Besides, *A* and *B* can be found experimentally from breakdown measurements. Table 4 lists *A* and *B* values for the given (*E/p*) ranges for the four gases that we are considering for this study. The table was developed based on data from Küchler [27] and Raĭzer [95] at 293 K. Values for *A* and *B* at different temperatures and for other gases are available in the last two references and from Heylen [94].

Table 4: Townsend's first ionization coefficient constants, particle mass and density factor at 293 K [27], [95]

Gas	***A*** **[1/(Pa.m)]**	***B*** **[V/(Pa.m)]**	***E/P*** **range [V/(Pa.m)]**	***m*** **[10^{-27}kg]**	D_f **[m^2/s^2]**
N_2	9.77	255	80 – 450	46.4	87,142.24
H_2	3.76	98	110 – 300	3.34	1,210,599
He	2.1	26	20 – 110	6.64	608,945.8
Ne	3	75	75 – 300	33.5	120,698.5

The approximation equation of Paschen's law gives the breakdown voltage values according to *pd* (product of pressure and gap distance) assuming constant γ values. That is the

conventional way for generating the Paschen's curves for research and industrial applications. Four gases, nitrogen (N_2), hydrogen (H_2), helium (He) and neon (Ne), were taken into consideration for this study since they have been used as cryogenic media for HTS devices in a pure form [41], [96]–[98] or in the form of mixtures [40], [99]–[101].

Paschen's curves for the four gases were plotted according to the conventional V_{bd} vs. *pd* relationship, shown in Figure 27. The curves represent the values at room temperature since *A* and *B* constants in Table 4 were used. Townsend's second ionization coefficient values varies for the same gas based on the electrode material [27], and they are valid for different (*E/p*) ranges [94]. Considering clean-surface iron electrodes, γ values were selected to be 0.06 for N_2, H_2 and Ne and 0.015 for He for plotting the curves [27]. For the lower *pd* limit, equation (14) gives a negative V_{bd} value when the *pd* product becomes small enough to turn the denominator to be negative. The negative values were neglected. The higher *pd* product value was chosen to be 2000 Pa.m.

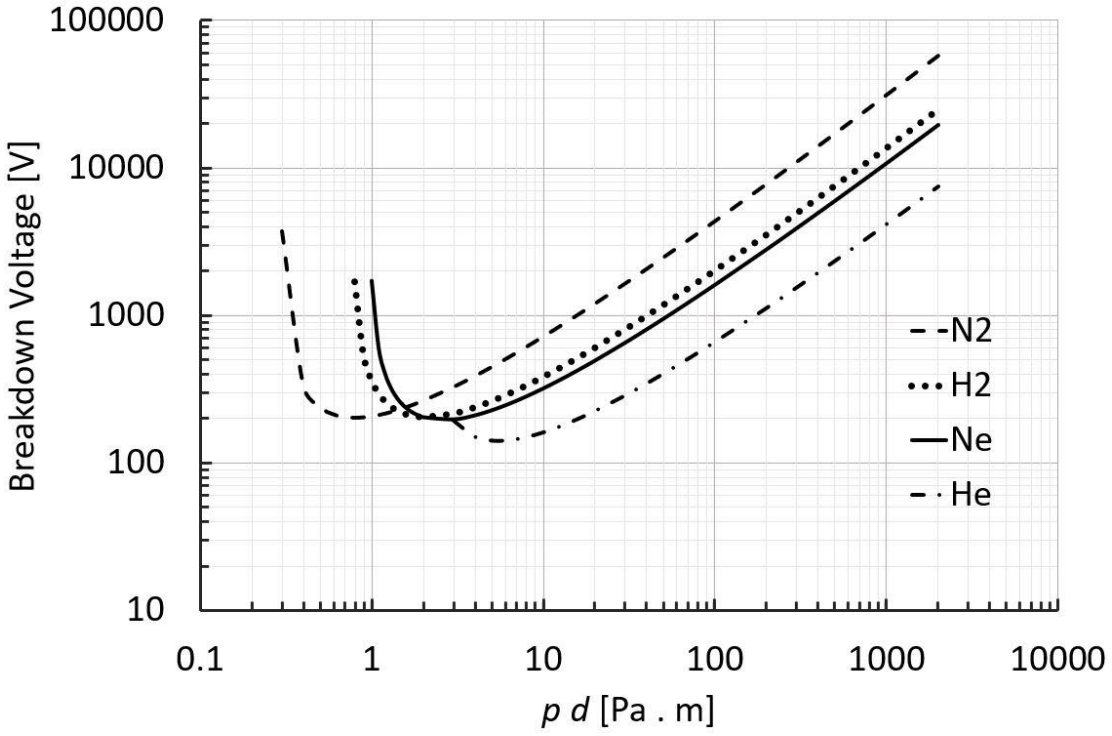

Figure 27: Conventional Paschen's curves for iron electrodes at 293 K

A second source of Paschen's curves is breakdown measurements. It is worthwhile to mention that performing the experiments for a large range of *pd* product to plot the whole curve for each gas type and different temperatures is a difficult task, and many factors should be taken

into consideration to achieve consistent results. Accordingly, there is a lack of complete information in the literature where sometimes the information does not exist or exists for only a part of the curve. Therefore, using the formula is considered an acceptable source for drawing the Paschen's curves. Although there were a few efforts to establish Paschen's curves for cryogenic gases by calculations [102], or empirically [103]–[105], there is a lack of adequate information for cryogenic temperature Paschen's curves. For instance, to generate a Paschen's curve for a gas at cryogenic temperature by calculation, the formula could lead to incorrect results since the constants *A* and *B* are given at certain temperatures, and they may vary with temperature.

4.3 Modified Paschen's Curves for Industry Practical Considerations

Although Paschen's curves have been a valuable resource for determining the dielectric strength of gaseous cryogens, there are two drawbacks associated with the practical aspect of them. First, for the electrical power industry, the conventional way of presenting the data as a function of pressure is not always practical since the electrical power apparatus, that use the gaseous media for insulation purposes, are different in size and shape. Pressure gauges are installed at a distinct location of the equipment, which may have a non-uniform temperature profile based on ambient conditions. Secondly, it will provide incorrect information when the gas is subjected to changes in temperature. Additionally, the gas could also approach its condensation temperature, which depends on the pressure. At the condensation point, the two-phase gas-liquid state yields uncertain breakdown voltage values that fluctuate within a range instead of a definite value. The validity of the approximation equation can be maintained if the variable is changing the distance, with constant pressure. If the operating conditions involve high pressures and lower temperatures to achieve high breakdown voltages, partial condensation should be evaluated after calculations before relying on the Paschen's curve data [92].

To address these practical challenges, we present a new representation of Paschen's law that uses the product of gas mass density ρ (kg/m^3) and gap distance d (m), instead of the pressure distance product. The modified plots are more practical for the industry than plotting the curves at many different temperature conditions. The justification of this proposition is based on the fact that Townsend's first ionization coefficient is originally a density function, and hence, temperature influence is eliminated. We have demonstrated the dependence of dielectric strength (breakdown voltage) of a gaseous media on its mass density regardless of temperature [93]. Figure 28

demonstrates the Paschen's curves plotted in Figure 27 after rescaling them to the product of gas mass density and gap distance, ρd, (g/m^2) by using (11) and mass of the gas particle for each gas type.

For further practicality, the following equation propose a new representation of Paschen's law that can be used to obtain the breakdown voltage as a function of mass density and distance product directly:

$$V_{bd} = \frac{B_\rho \cdot \rho d}{ln\left(\frac{A_\rho \,.\, \rho d}{ln(1 + 1/\gamma)}\right)} \tag{15}$$

where $A_\rho = A \cdot D_f$, and $B_\rho = B \cdot D_f$, and they represent the modified Townsend's first ionization coefficient constants while D_f is the density factor which equals to:

$$D_f = \frac{k_B T}{m} \tag{16}$$

in which m is the mass of the gas particle. Refer back to Table 4 for the different values of m and D_f according to each gas type where gas particle mass values were found by dividing the molar mass by Avogadro's constant. Regarding to the density factors, although they were calculated for 293 K, they are valid to find V_{bd} for any gas density at any other temperature since they are used with A and B that were given at the same temperature.

By using the same values of A, B and γ used to plot any gas Paschen's curve in Figure 28, the exact same operating point can be found by using equation (15). Using the equation is preferred over using the curve, again for practical reasons. It can simply be programmed on calculators and personal computers. Hence, the required gas mass density, which is independent of temperature, is directly obtained for the required dielectric strength and the system's minimum gap distance without the need to plot the whole curve.

After finding the mass density value (using curve or equation), the check for validity comes next by comparing the mass density value to the condensation mass value of the gas. Following, and if the mass density passed the condensation evaluation, the gas mass needed for the system can be found by multiplying the system volume that the gas is going to occupy by that mass density. Finally, the required gas mass can be calculated to provide the required dielectric strength.

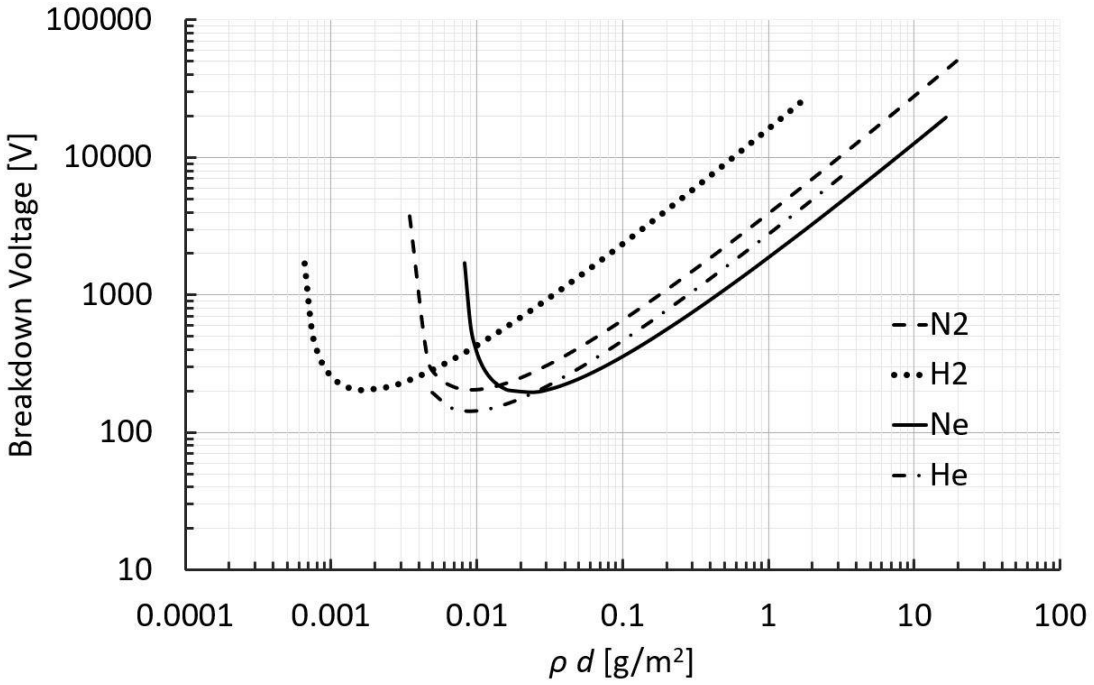

Figure 28: Proposed Paschen's curves as functions of the product of gas mass density and distance

To confirm whether condensation would occur or not, a condensation boundary line can be used to find the mass density at the condensation point, which should not be exceeded, to prevent condensation for a given operating temperature. Figure 29 was plotted to mass density instead of pressure for N_2 based on Park's data [92] as an example.

4.4 Higher Dielectric Strength for Gas Mixtures

As mentioned earlier, utilizing GHe as the cryogen is preferred in some applications due to its many benefits. The most important reason to utilize GHe for transportation applications, GHe is preferred over LN_2 due to confined spaces in case of cryogen leak existence [15]. On the other hand, it has much wider operating temperature window (4-80 K) serving in the gas phase compared to small temperature liquid phase window of LN_2 (65-77 K) [2]. This feature allows increasing the critical current of the superconductor. For instance, an increase up to 4 to 5 times in the HTS cable ampacity when reducing the operating temperature to 50 K from 77 K to [22], as was shown in Figure 6 in Chapter 1. The wide range of operating temperature allows also to connect several HTS devices in series or parallel to be cooled be the same GHe stream without the need for separate cryocooler for each device [91].

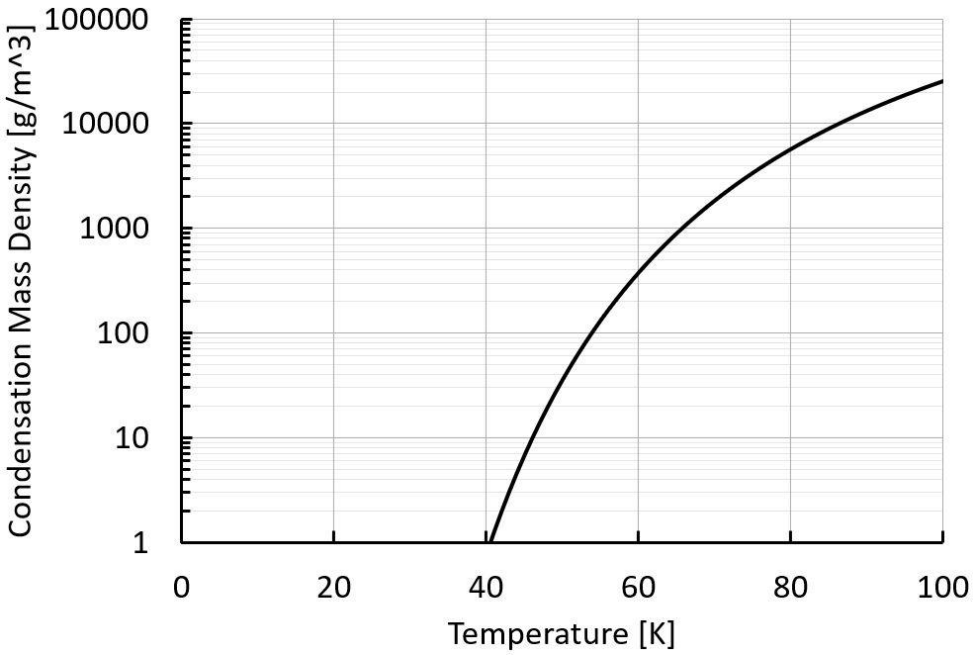

Figure 29: Condensation boundary line as a function of operating temperature for N2 (Area below the curve: gas phase. Area above the curve: liquid phase)

The main disadvantage of utilizing GHe is its weak dielectric strength. It is 4 kV/mm in a uniform electric AC field at 1.0 MPa and 77 K [43]. Although GHe dielectric strength seems good since it is little bit higher than air dielectric strength 3 kV/mm, it is not strong enough for HTS cable application because the high-power density requires much smaller volume and clearances compared to terrestrial power grid applications. Thus, investigating increasing the dielectric strength of GHe was another research direction for our research group. It was found that adding a small mol% of hydrogen to GHe improves the dielectric strength significantly [40]. A versatile model was proposed to describe and estimate the breakdown voltages of gas mixtures has been developed [102].

Many gas species have been tested, including the addition of 1, 2, 4 and 6 mol% of hydrogen to GHe. The results came close to the versatile model, with the highest dielectric strength for the 4 mol% of H_2 helium-based gas mixture. The 4 mol% gas species demonstrated 80% enhancement in the dielectric strength compared to pure GHe [40]. Therefore, the 4 mol% H_2 helium-based gas mixture has been considered for the dielectric strength experimental testing and compared to the GHe testing results.

4.5 Characterization of Gases

As discussed in the previous section, different gas mixtures have been characterized in our lab, and results provide a useful database for gas-cooled HTS devices. A separate research work has been conducted for that purpose to test the dielectric strength of the different gas species [106]. As shown in Figure 30, the experimental setup, including Bruce profiled electrodes has been arranged since they provide a uniform electric field for small distances, 1 and 2 mm. Pure GHe and 1, 2, 4 mol% of H_2 helium-based gas mixtures have been characterized at room temperature and 77 K, and at different pressure levels of 0.5, 1.0, 1.5 and 2.0 MPa.

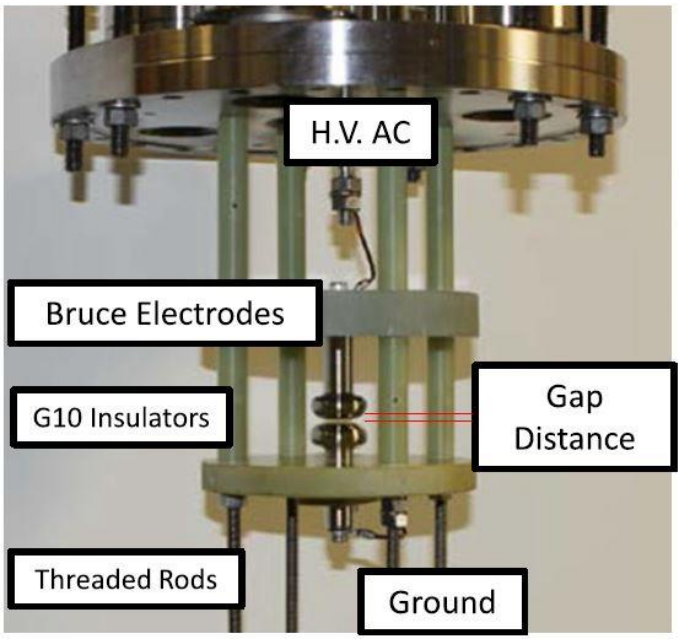

Figure 30: Uniform electric field gas characterization setup with Bruce profiled electrodes system [106]

The results proved the predicted outcome regarding to adding small mol% of H_2 to the GHe, and hence, the 4 mol% H_2 mixture showed the highest dielectric strength of 41.2 kV/mm (DC) and 27.2 kV/mm (AC rms) at 2.0 MPa and at 77 K.

The results also showed that the dielectric strength is related to the gas density. Thus, increasing the gas density by using higher pressure yields higher dielectric strength.

4.6 Design of Superconducting Gas Insulated Line

As discussed in the previous section, the helium-based gas mixtures demonstrated promising dielectric strengths that are suitable for medium and low voltage power cables. This result inspired the idea of utilizing helium gas or helium-based gas mixtures as sole electric insulation media without any solid insulation for HTS cables. The new innovative design is called superconducting gas-insulated transmission line (S-GIL) [41]. The main idea is to eliminate lapped tape insulation, which traps helium gas causing low PDIV. The solid insulation role was to provide the insulation system the required dielectric standoff between the HTS conductor and the grounded cable cryostat. In all past HTS cable designs, the insulated cable touches the cryostat. For the new S-GIL design, the conductor needed to be moved away from the cryostat, and the optimum situation is achieved by making the HTS conductor position at the axis of the cryostat. That was the required trade, and it was achieved with the help of insulating spacers designed specifically for that purpose. Figure 31 shows the difference between the commonly used and the S-GIL designs for HTS power cables.

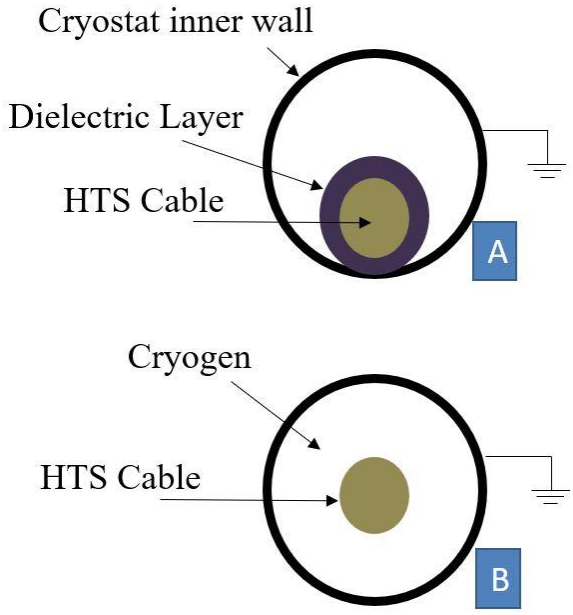

Figure 31: (A) Commonly used HTS cable design (B) superconducting gas insulated line design

The spacers should be designed in a way that they do not obstruct the gas flow. The spacer designs must have large percentage opening in its cross-section to allow the cryogenic gas flow without a significant pressure drop. Therefore, one of the major design challenges for S-GIL is the spacer design. Solutions to address these spacers for positioning the HTS conductor on the center axis and the many other advantages obtained from the S-GIL design with full analysis and details will be presented in the next chapter.

4.7 Chapter Conclusions

The necessity of estimation of dielectric strength of gaseous electrical insulation systems for gas cooled HTS power devices motivated the exploration of alternative methods to represent Paschen's Law suitable for a wide range of temperatures and pressures. We predicted and observed in experiments that the dielectric strength of gaseous media scales with mass density, which allowed us to present an effective new representation of Paschen's law in which the breakdown strength is a function of the product of gas mass density and gap distance ($\rho \cdot d$) rather than the product of gas pressure and gap distance ($p \cdot d$), which is used in the standard form. The values for breakdown voltage, calculated using the new representation, are confirmed for variable temperatures and pressures. This is shown by identical values for either manual rescaling of the graphs or for using the modified equations and coefficients. The new representation provides a practical tool for high voltage engineers and researchers to estimate the dielectric strength of gas insulation systems at wide range of temperatures. Furthermore, this representation also informs them about the important finding that the dielectric strength of gas media varies with mass density.

CHAPTER 5

INSULATOR SPACER DESIGNS AND MATERIALS OPTIONS FOR S-GIL CABLE CONCEPT

5.1 Introduction

In this chapter, the novel S-GIL design concept is presented. The design offers a solution to the challenges associated with the partial discharge phenomena and in particular the low PDIV values that the lapped tape insulation system for gas cooled HTS power cables is suffering from. The S-GIL design concept eliminates the need for a solid insulation as discussed at the end of Chapter 1. The design also provides other benefits since the HTS conductor is not enclosed inside the solid insulator for direct contact with the circulating gas coolant. In addition, the gaseous dielectric medium offers the ability to recover after a breakdown event. The S-GIL design is more advantageous in terms of better heat transfer which helps with minimizing the occurrence of hot spots in the HTS conductor layer. The design also helps with reducing the space charge accumulation due to the continuous gas flow and the absence of solid insulation. The S-GIL design takes advantage of and benefits from the gas mixtures with enhanced dielectric strength. It was shown by our research group that adding a small mol% of H_2 to GHe results in a gas mixture with a significantly enhanced dielectric strength [40]. For instance, adding 4 mol% of H_2 to He resulted in an 80% increase in the dielectric strength of the gas mixture.

For a single-phase AC design or a single pole DC design, the HTS conductor should be positioned at the center of the cryostat cross-section to maximize the standoff of the HTS cable from the grounded cryostat. The main design challenge in the S-GIL is the insulator spacer that is needed to ensure the position of the conductor close to the axis of the cryostat. Two design concepts are proposed considering the mechanical aspects of the HTS cable system. Each design has advantages and disadvantages, and ultimately the intended application will determine the appropriate design.

Electrically, the S-GIL similar to the Gas Insulated Transmission Lines (GIL) which use SF_6/N_2 gas mixtures as the insulation medium for room temperature applications [42]. Similar to the GIL, S-GIL also requires insulator spacers to ensure the conductor remain concentric to the grounded cryostat. Where these designs differ is that the S-GIL operates at cryogenic temperatures

and requires the insulating cryogen be circulated while GIL operates at room temperature and its insulation gaseous medium is stagnant in the cable section. This is an important characteristic as the current rating of the superconducting cable is a function of operating temperature and minimization of the temperature gradient along the cable length is essential for achieving the highest possible current rating. Hence, achieving the spacer designs that would facilitate sufficiently large mass flow rates of the cryogen is crucial. On the other hand, minimizing temperature gradient would also minimize the pressure gradient and allow for a higher density to be achieved which in turn would allow for potentially higher voltage ratings

Considering the electrical aspects, reducing the electric field enhancement is always the priority, and it is achieved by the design geometry and material selection. Regarding to the design geometry for coaxial cable, shown in Figure 32, the electrical field intensity can be found by Laplace's equation or Gauss's law, and the maximum electric field (E_{max}) will occur at surface of the inner conductor [23]. Thus, the electric field in between the inner conductor and cryostat is non-uniform, and E_{max} is given as:

$$E_{max} = \frac{V}{r_1 \ln(r_2/r_1)} \tag{17}$$

where V is electric potential of the inner conductor, r_1 is outer radius of the conductor and r_2 is the radius of the inner wall of the cryostat.

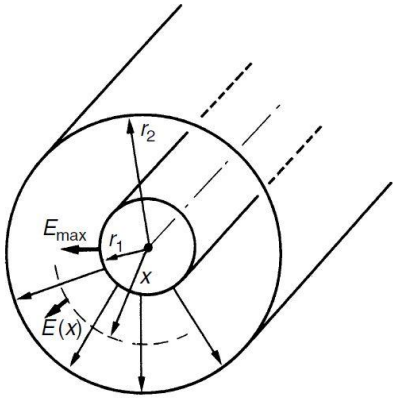

Figure 32: Cylindrical coaxial cable geometry [23]

The non-uniform distribution of the electric field, with maximum value on the surface of the conductor and minimum at the inner surface of the cryostat, has its implication on the

breakdown voltage (V_{bd}). When the field is non-uniformly distributed in between, electric field efficiency factor (η) plays a role in determining V_{bd} if the breakdown occurs only due to the impact of E_{max} alone, with no other factors effects [23], as shown in the equation below:

$$V_{bd} = E_{max}\, d\, \eta \tag{18}$$

where d is the gap distance and η = (E_{mean} / E_{max}). the value of η varies from 0 (for extremely non uniform field) to 1 (for perfectly uniform filed, and so, $V_{bd} = E_{mean}\, d$).

To optimize the electric field distribution, which reduces the corona discharges inside the cable, the outer cryostat size to inner conductor size ratio for the cylindrical coaxial cable design should be optimized according to equation (17) as follows [23]:

$$\ln(r_2/r_1) = 1 \tag{19}$$

Since commercial vacuum jacketed cryostats come in fixed sizes, the conductor size needs to be optimized for a given size of the cryostat. For the cryostat with 39 mm inner diameter, optimized size of the conductor was found to be 14.14 mm.

The work for this dissertation focused on potential electric field enhancement caused by the insulator spacers in the S-GIL design. Two spacers design concepts have been proposed, according to S-GIL cable design requirements, to be rigid or flexible, as depicted in Figure 33 [107].

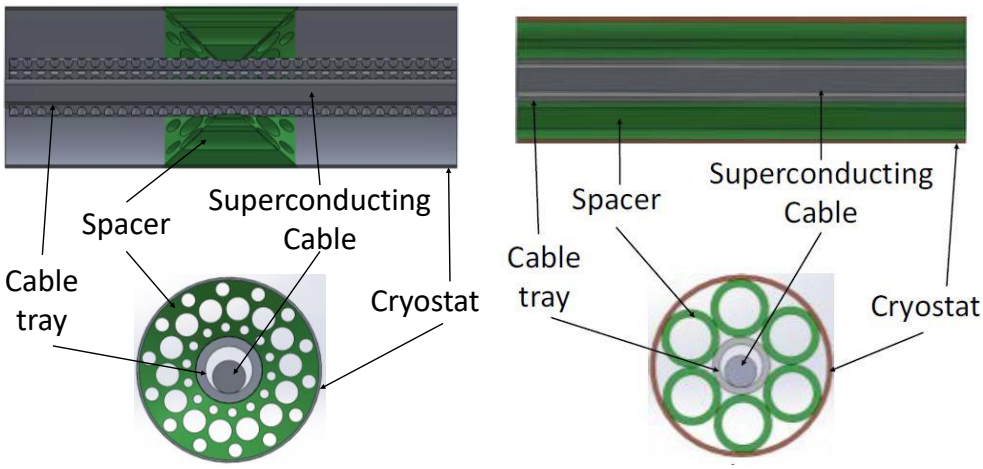

(a) (b)

Figure 33: Schematic for (a) rigid spacers S-GIL design concept using plastic spacer discs (b) flexible spacers S-GIL design concept using bundled insulating tubes [107]

As shown in Figure 33, both S-GIL designs will have the HTS cable installed within a perforated conduit made of a metal with the perforated conduit and HTS cable in electrical contact and hence at the same voltage potential [107]. This will ensure that the optimized ratio of the diameter of the conductor (in this instance outer diameter of the perforated conduit) and the inner diameter of the cryostat (at ground potential) can be achieved. Doing so also ensures that this design enables incorporation of various HTS cable designs with diameters smaller than the inner diameter of the conduit. For this design iteration of the rigid spacers S-GIL, the inner diameter of the cryostat is fixed at 39 mm, which results in the optimized outer diameter of the conductor/conduit being 14.14 mm. In sections of the rigid spacers S-GIL design without the insulator spacer discs, the electric field is characterized by the coaxial electric field equation, with a maximum electric field of 0.14 kV/mm occurring on the surface of the conductor [23], [108].

For the rigid spacer S-GIL design concept, insulator spacer discs were proposed that can hold the cable at the center of the cryostat, as shown in Figure 33 (a). The cross section of the spacer main design has a center circular opening so that it provides the support for the HTS cable with the cross-section area with ample opening for cryogen to flow. The spacer outer surface fits the cryostat inner surface. Three insulator spacer designs were developed for the S-GIL cable, and they are as shown in Figure 34. Table 5 lists the specifications for the three designs. Desgin1 has a large opening for gas circulation and increased creepage distance (between the centered conductor and the cryostat). Design 2 has also a large opening for gas circulation and increased creepage distance. In addition, it allows direct contact of HTS conductor with the cryogen. Finally, design 3 has the largest opening and the least volume and simplicity in the geometry. The research on spacer designs and manufacturing methods is ongoing and is not presented here [109]. The

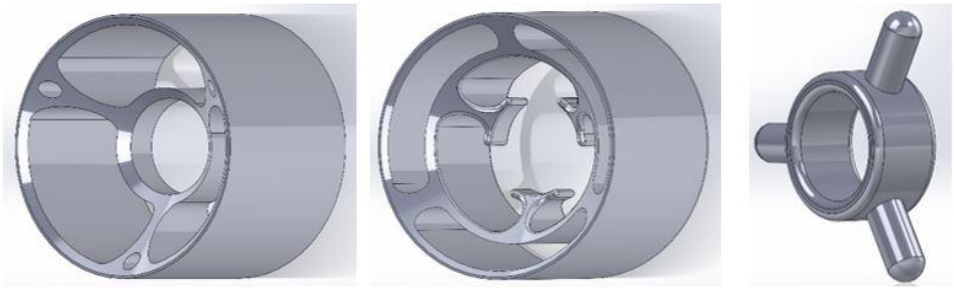

Design 1 Design 2 Design 3

Figure 34: Rigid spacers designs for S-GIL concept [109]

spacers were fabricated using additive manufacturing technique, commonly known as FDM 3-D printing.

Table 5: Specifications of rigid spacers designs [109]

Spacer Design	Length (mm)	Volume (mm^3)	Open Space (%)	Surface Area (mm^2)	Outer diameter (mm)
Design 1	29.2	7,069	76.6	9,125	39.0
Design 2	29.2	7,818	74.8	11,090	39.0
Design 3	10.0	1,798	82.6	1,629	39.0

For the flexible spacer S-GIL design, it is possible to use commercially available flexible cryostats typically used for many HTS cable applications. The use of a flexible cryostat requires the insulated spacer to run the entire length of the superconducting cable to ensure the conductor remains concentric. Thus, for the flexible S-GIL, tubular insulator spacers that are evenly distributed around the cable in a bundled pattern was developed to provide the mechanical support for the HTS conductor to sit at close to the center, as depicted in Figure 33 (b). Again, the tubes geometry was designed to reduce the electric field enhancement. They also add to the dielectric strength.

As shown in Figure 33 (b), for the flexible S-GIL design, the tube bundles were designed to fit snugly in the space between the conductor/conduit and the cryostat. Figure 35 depicts the three different designs that utilizes 6, 24 and 99 bundled insulator tubes.

For this design, which was seen as advantageous to implement due to its simplicity and availability, utilizing tubular spacers provides support to keep the HTS conductor concentric to the cryostat. To be able to utilize commercially available insulator tubing while also utilizing the inner diameter (39 mm) of a commercially available cryostat, it was necessary to set the diameter of the HTS conductor to 12.7 mm. The HTS conductor is close to the optimized conductor diameter of 14.14 mm which is derived from the coaxial electric field equation. Using this design philosophy three insulator design were determined for the tubular insulator spacers, shown in Figure 35, and the variations of these designs using commercially available tubes is described in Table 6.

The free space percentage shown in Table 6 was calculated by:

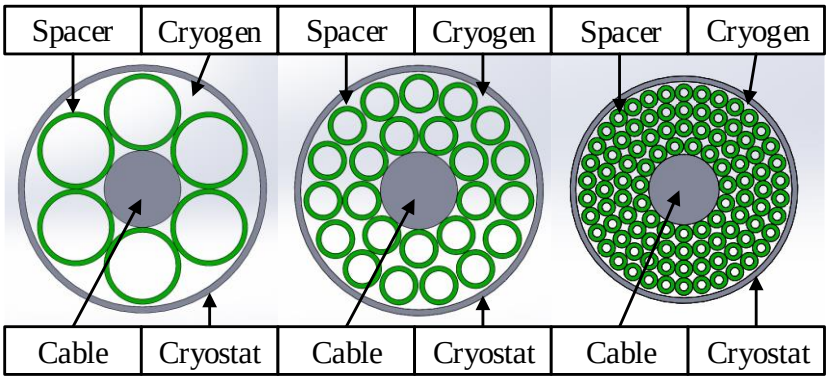

Figure 35: Cross-section for three flexible S-GIL designs utilizing tube bundles

$$Free\ space = 1 - \frac{(r_{OD}^2 - r_{ID}^2)\,N}{r_c^2 - r_s^2} \tag{20}$$

Where r_{OD} is the outer radius of the spacer tube, $r_{ID}$is the inner radius of the spacer tube, N is the number of tubes, r_c is the inner radius of the cryostat, r_s is the outer radius of the superconducting cable. The percentage of free space is important to consider for an insulator spacer for the S-GIL design as it is necessary to circulate GHe at flow rates of approximately 10 g/s to ensure the required operating temperature of the superconducting cable is maintained. The percentage of free space equates to the potential pressure drop which may be experienced over the length of the cable route due to changes in cross sectional area. It is also necessary to consider the drag on the inner and outer walls of the tubular spacer which may also increase the total pressure drop of the system. The total wall interfaces per unit length (A_{if}) with cryogen presented in Table 6 was calculated by:

$$A_{if} = (2\,\pi\,r_{OD} + 2\,\pi\,r_{ID})\ \times N \tag{21}$$

From analyzing the results of Table 6, it can be seen that while the 12.7 mm and 6.35 mm tubes have options with the same free space the total wall interface for the 6.35 mm tubes has approximately double the interfaces with the cryogen. Taking into consideration how changes in cross sectional and friction may affect the cryogenic circulation the 12.7 mm outer diameter tubular spacer provides the optimal solution.

As it is necessary to consider both the electrical and mechanical implication when selecting an insulator spacer for S-GIL, the 12.7 mm outer diameter spacer tubes were seen as being

advantageous as it had the highest percentage of free space as well as the smallest wall interfaces with the cryogen.

Table 6: Electrical and mechanical properties of potential materials for tubular insulating spacer design

Outer Diameter of Tube (mm)	Inner Diameter of Tube (mm)	Number of Tubes	Free Space (%)	Total wall interfaces with cryogen (mm/unit length)
12.70	11.11	6	83	448.8
12.70	9.53	6	69	419.0
6.35	4.37	24	62	808.3
6.35	4.76	24	69	837.7
3.18	1.59	99	45	1483.6
3.18	1.98	99	55	1604.9

Next design decision was to select the tube materials that yield minimal electric field enhancement. For AC HTS cable applications, as discussed in Chapter 1, the tubes materials were selected to have a relative permittivity values close to the gaseous cryogen used when AC field is applied. Otherwise, the discrepancy of the relative permittivity values between the solid spacer material and the cryogen will result into electric field enhancement at the conductor-insulator interface [107]. The relative permittivity is 1.0 for the considered gas medium, which is GHe. Therefore, three materials - Polytetrafluoroethylene (PTFE), which is commonly known as Teflon™, polyethylene (PE) and Nylon™ materials - were selected for the tubes to check the effect of electric properties of the material on the electric field enhancement, and consequently, the dielectric strength of the S-GIL insulation system. The relative permittivity values for PTFE, PE and Nylon are 2.1, 2.25 and 3.5, respectively. Based on the theory, the relative permittivity of the tube materials being close to that of GHe the S-GIL insulator designs should yield a dielectric strength close to the value estimated from the geometry. However, small differences are expected among the three different materials in their respective electric field enhancements.

Electric field analysis was completed on the 3.18 mm, 6.35 mm and 12.7 mm outer diameter insulator spacers. For the electric field analysis, a systematic study was completed by assigning the insulator tubing with the above-mentioned relative permittivity values for the selected materials for the various geometries shown in Figure 35. The finite element study applied a nominal 1 kV to the conductor and set the cryostat to ground potential. The remaining space within the model was set to have the permittivity of helium gas (1.0). The results of this study are presented in Table 7 with one of the test cases demonstrated in Figure 36.

Table 7: Max electric field for different design with different materials based on finite element electric field analysis study

Material	Relative Permittivity	Number of Tubes	Max Electric Field (kV/mm)
Polyethylene	2.25	6	0.28
		24	0.26
		99	0.29
Nylon 6.6	3.5	6	0.43
		24	0.40
		99	0.45
PTFE	2.1	6	0.26
		24	0.25
		99	0.27

From Table 7, it can be seen that the mismatch in permittivity between the insulator spacer material and helium gas has the greatest impact on the maximum electric field which is located on the triple point interface between the conductor, insulator spacer and helium gas (Figure 36 (b)). Changing the geometry of the insulator spacer between 12.37 mm, 6.35 mm and 3.18 mm had a negligible effect on the electric field enhancement. The other electrical consideration which must be taken into consideration is the creepage distance which refers to the distance required for a surface flashover to occur between the conductor and cryostat along the surface of the insulator spacer. All of the tubular spacer configurations shown in Figure 35 have the same creepage distance of 19.9 mm.

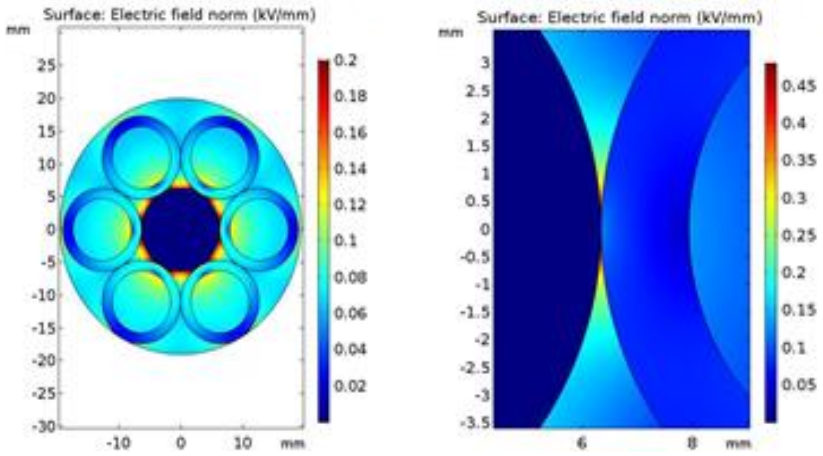

(a) (b)

Figure 36: Finite element electric field analysis for (a) cable cross-section (b) close view for conductor-insulating tube interface [107]

Again, for this iteration of the S-GIL design, a single-phase AC HTS cable geometry was utilized. While HTS cables are being developed for both AC and DC voltage applications, the mechanisms and electrical properties which influence the voltage rating of HTS cable differ when operated with an AC, positive DC, or negative DC voltage signals. AC operating conditions were chosen as it allows for a systematic study to be performed on tubular insulator spacers. It is envisioned that optimizing the electrical insulator spacers for dc voltage signals will be undertaken in the next stage of this work.

Our previous research demonstrated a prototype single phase S-GIL HTS cable design utilizing a polyethylene helical insulator spacer, had a breakdown voltage of approximately 35 kV AC rms at 77 K in 4 mol% H2 and GHe mixture. This was approximately 10 kV lower than the breakdown value obtained during the proof of concept measurements which did not contain an electrical insulator spacer. This prototype design was developed using an existing commercially available air core dielectric RF cable which had equivalent dimensions to what is envisioned for a single-phase S-GIL. While further adding credibility to the S-GIL design for GHe cooled HTS cables it also demonstrated the importance of optimizing the electrical insulator spacer design and material. The helical spacer design was also seen as potentially undesirable to install in long length HTS cable routes. Therefore, the next stage of our research was to investigate a simplified insulator spacer designs which can easily be incorporated into long length HTS cables, while also providing

electrical breakdown measurements equivalent to the proof of concept measurements we had already obtained.

Introduction of the spacers will result in an enhancement of the electric field, with the enhancement depending on the geometry of the spacer, the electrical properties of the spacer material [107], the electrical properties of the cryogen used, and the desired operating voltage signal (AC or DC). In addition, the insulators provide an insulating surface path between the HTS cable and the grounded cryostat. Consequently, surface flashover phenomenon is more likely to occur on the surface of the tubular insulators rather than breakdown through the gas. It is also necessary to consider the electrical implications of using various sized outer diameter insulator spacer tubing. The surface flashover phenomenon occurs at lower voltage levels than the dielectric strength of the dielectric gaseous medium. Flashover strength for the bundled insulating tubes S-GIL design was characterized for different tubes materials and gases.

For experimental investigations, the designs with 6 and 24 tubes were used. For the design with 6 tubes, the outer and inner diameters were selected to be 12.7 and 9.52 mm, respectively. For the design with 24 tubes, the outer and inner diameters were selected to be 6.35 and 4.37 mm, respectively.

5.2 Characterization of Insulation System Strength for Bundled Tubes S-GIL Design

Figure 37 shows the 6 and 24 bundled insulating tubes S-GIL designs that were prepared using Kapton tape to fix the tubes around the cable. In the case of 24 bundled insulating tube design, the tubes were installed in two layers, 9 tubes for the inner layer and 15 tube for the outer layer. Then, the cable inserted inside the grounded copper tube, which represents the grounded cryostat in the real cable system.

The experiment setup was mounted on the lower side of the top plate of the pressure vessel, and the cable is screwed in the current lead that pass through the HV busing. Holes were made at both ends to have openings for the gas to pass through the insulating tubes. That is shown in Figure 38 with the experimental arrangement.

Besides the surface flashover experimental setup on 1 m prototype cables, shown in Figure 39 (a), another experimental setup was prepared. This setup included a long copper tube, which represents the 39 mm cryostat for the cable, that is fixed to the ends of the cable and right on the ends of the stress cones by short plastic threaded rods, as shown in Figure 40. This setup is called

“optimized S-GIL design” since it does not include any insulating spacer, and the breakdown happens through the gas as an intrinsic breakdown. The optimized cable design experiments were conducted to collect breakdown data to be compared to the surface flashover data collected for the bundled tubes S-GIL design.

For all different experimental setups, which are attached to the vessel’s top plate, they get inserted in the vessel. Afterward, the vessel is sealed and inserted into the cryostat. The experimental setup is as shown in Figure 39 (b and c).

(a) (b)

Figure 37: The bundled insulator tubes S-GIL cable prepared with Kapton tape to bind (a) 6 tubes one-layer arrangement (b) 24 tubes two-layer arrangement

Before the start of any HV breakdown experiment, the steps to achieve high purity gaseous environment inside the sealed vessel that were mentioned in Section 3.2 are performed, and it helped also to check if there is any leak. Again, besides the characterization of the HTS cable at cryogenic temperature, characterization at room temperature was carried out first to check if everything is working properly. Additionally, the results of room temperature experiments allow for a comparison with the results at cryogenic temperatures. The room temperature experiments were performed with the pressure vessel in an empty cryostat. For the cryogenic tests at 77 K, the cryostat was filled with LN_2 to maintain 77 K in the S-GIL.

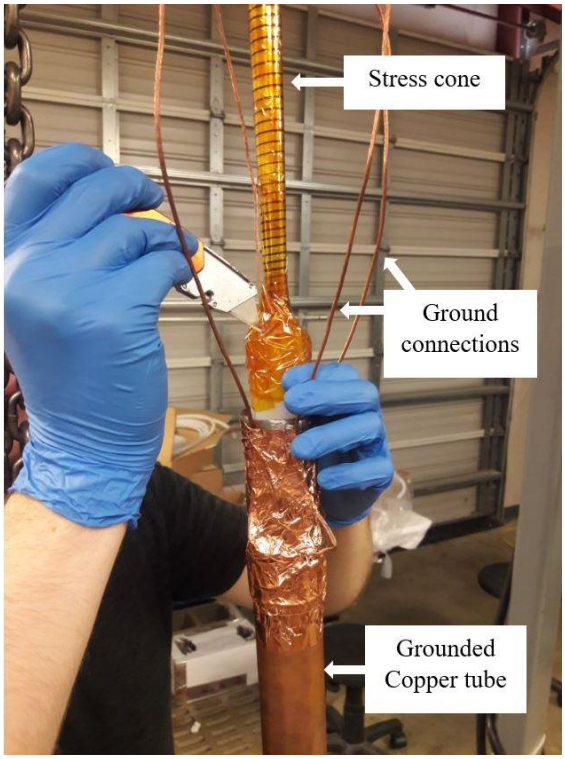

Figure 38: Inserting perforations to allow gas to enter inside the insulator tubes

5.3 Experiments and Results

All experiments for the dielectric strength tests of different S-GIL designs were performed using the Haefely test kit. As mentioned earlier, AC measurements were considered since it allows for a systematic study to be performed on tubular insulator spacers. Measurements were performed on 1-m long prototype cables at 4 different pressure levels (2.0, 1.5, 1.0 and 0.5 MPa) for both pure GHe and the 4 mol% H_2 GHe gas mixture at AC (rms, 60 Hz). The purity of research grade GHe that has been used was 99.9999%. Many samples have been prepared and tested, since each sample showed degradation after taking many measurements with an average of 40 tests for each sample cable. For each data point of pressure level, at least five measurements were recorded to provide an accurate comparison between variations in material, gas species and gas density. Many samples have been prepared and tested according for the 6-tube bundle S-GIL design experimental matrix, shown in Table 8. For the 24-tube bundle S-GIL design, only PE tubes were tested with the two gas species for the two different temperatures, room temperature and 77 K, as will be explained in the next section.

(a)

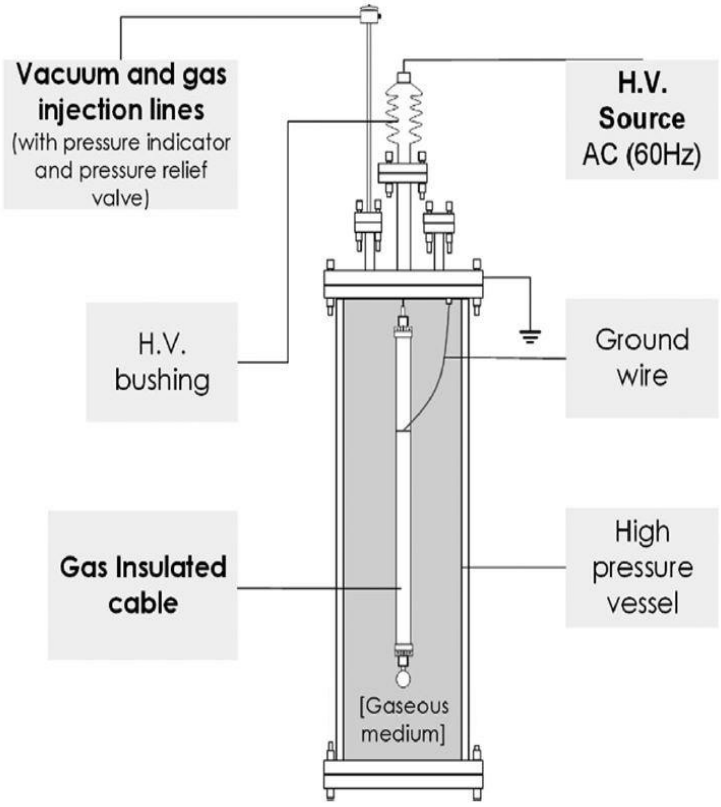

(b)

(c)

Figure 39: (a) The bundled tube S-GIL cable attached to the pressure vessel's top flange with ground connections (b) sketch for the experimental setup inside the vessel [41] (c) vessel inside view with cable inserted

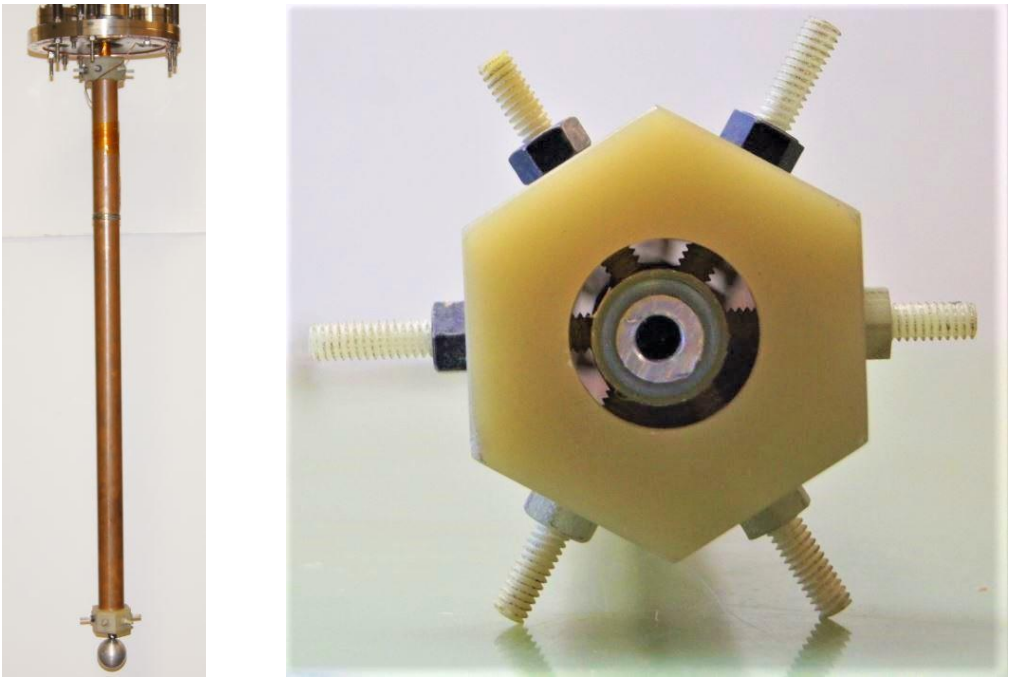

(a) (b)

Figure 40: (a) Optimized S-GIL design setup (b) lower view for the setup without the stress sphere

In general, each bundled tubes S-GIL sample is either tested with one gas at two different temperatures or with two gas species at the same temperature. After testing the sample with a gas at room temperature, the cryostat was filled with LN_2, which consequently cools down the gas inside the vessel. More gas is added to reach the required pressure. After completing the tests with one gas, the system was allowed to come to room temperature and the test cycle is repeated with a different gas.

Table 8: S-GIL characterization experimental matrix

Insulating tubes Material	S-GIL design	Temperature (K)	Gas species	Pressure (MPa)	Excitation
PE	6 tubes	RT	GHe	2.0, 1.5, 1.0, 0.5	AC
Nylon 6.6					
PTFE		77 K	4 mol% H_2 helium-based gas mixture		

Intrinsic breakdown experiments were performed for the optimized S-GIL design without any spacers. Thus, all measurements were carried out with the same setup, but with two different gases, GHe and 4 mol% H_2 GHe-based gas mixture at room temperature and at 77 K, with pressure levels of 2.0, 1.5, 1.0, 0.5 MPa for each gas type. The steps to achieve high purity gaseous environment inside the sealed vessel were performed before the start of the experiments.

The four sets of results for 6 tube bundled S-GIL design using different tube material are shown in Figure 41-44 for GHe and 4 mol% helium-based gas mixture at room temperature and 77 K, respectively. Figure 45 and 46 show the results of 24 PE bundled tubes S-GIL design for GHe and 4 mol% at room temperature and 77 K compared to 6 PE bundled tubes S-GIL design. For all the results, each data point at each pressure level is the average of at least five measurements.

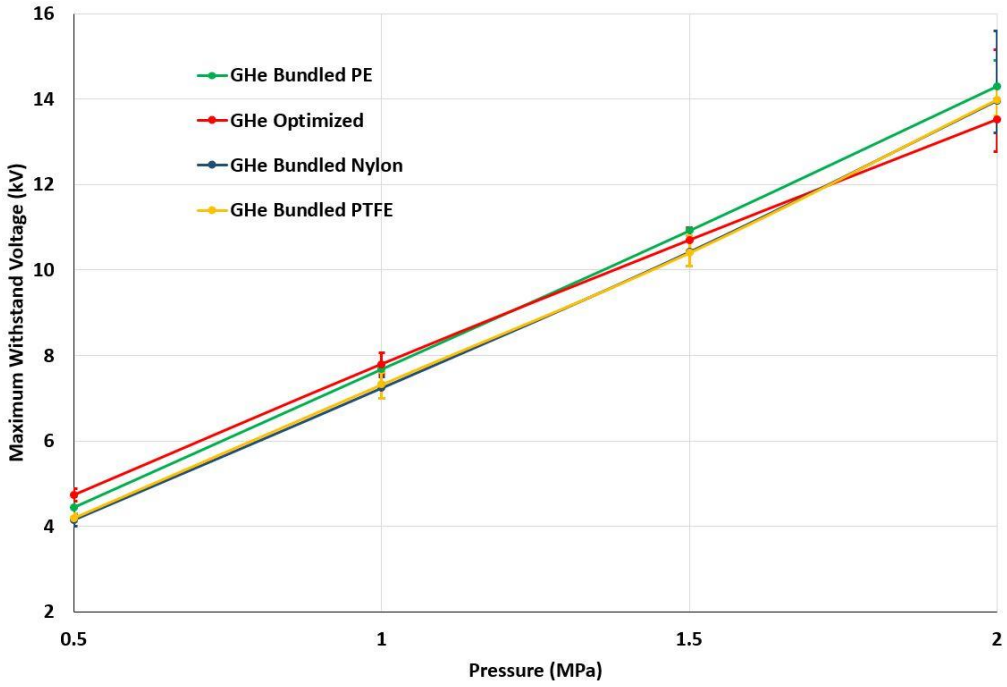

Figure 41: Intrinsic breakdown and surface flashover voltage for various pressures for optimized and bundled spacers S-GIL designs in GHe at room temperature

5.4 Analysis of the Results

All measurement data shown are in rms values for AC signals applied with 60 Hz frequency. For the optimized S-GIL design, with no spacers, breakdown voltage values were lower

than what was expected based on the geometry and dielectric strength of the gas medium (e.g. for 4 kV/mm dielectric strength of GHe at 1.0 MPa and 77 K [43], with a gap distance of approximately 12.7 mm, the breakdown values are expected to be around 50 kV. However, the measured values were around 17 kV. This is due to the field efficiency factor caused by the non-uniformity of the electric field. In addition, it was expected that the results obtained from the optimized S-GIL design to be the highest since it is an intrinsic breakdown compared to the surface flashover for the bundled spacers S-GIL designs. However, that was not observed. The reason behind that is most likely due to the movement of the cable from the axis and the uncertainty of geometry associated with the motion of the cable away from the axis.

Regarding to the 6 bundled tubes S-GIL design measurements at room temperature in GHe, no significant difference in the results was noticed since the weak dielectric strength of GHe is playing the main role at these operating conditions, as shown in Figure 41. Thus, the spacer material, and hence the material permittivity, is not the contributing factor in the dielectric strength in the room temperature tests.

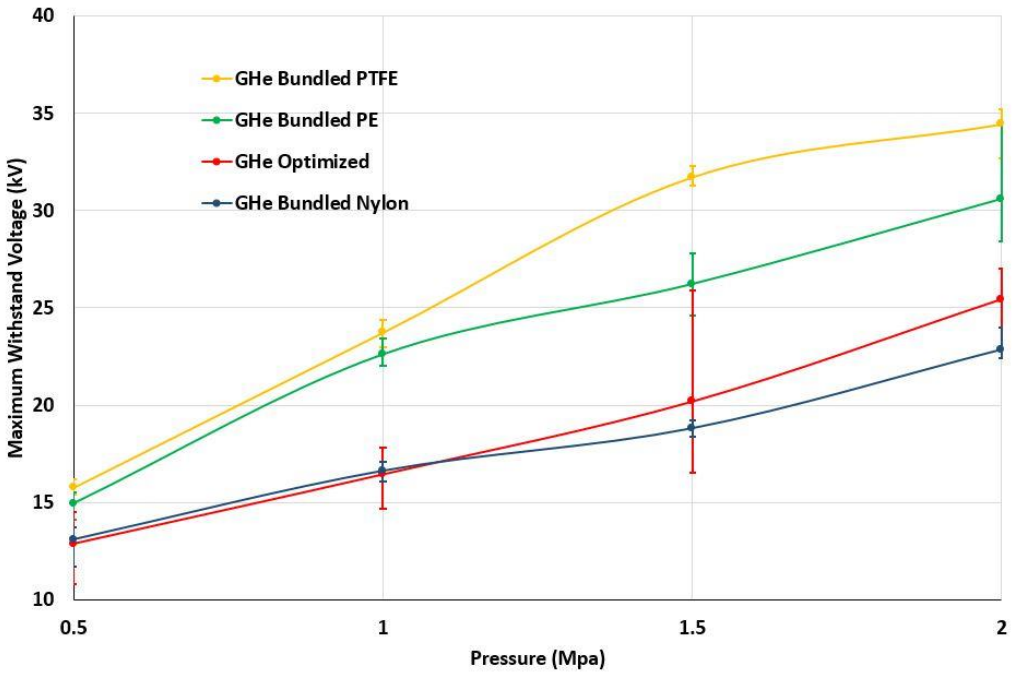

Figure 42: Intrinsic breakdown and surface flashover voltage for various pressures for optimized and bundled spacers S-GIL designs in GHe at 77 K

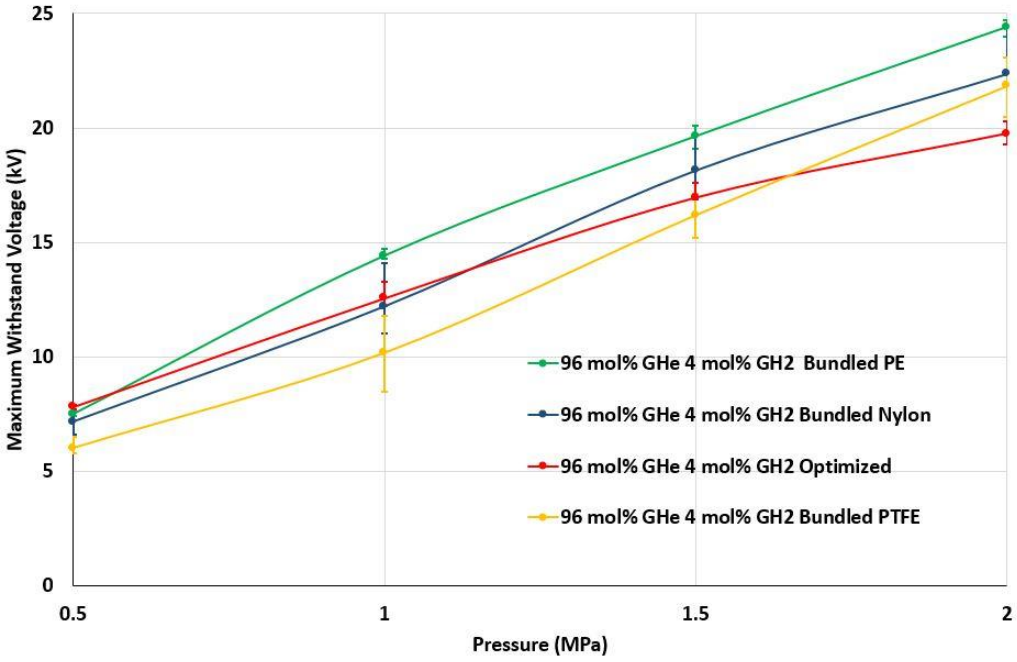

Figure 43: Intrinsic breakdown and surface flashover voltage for various pressures for optimized and bundled spacers S-GIL designs in 4 mol% H2 helium-based gas mixture at room temperature

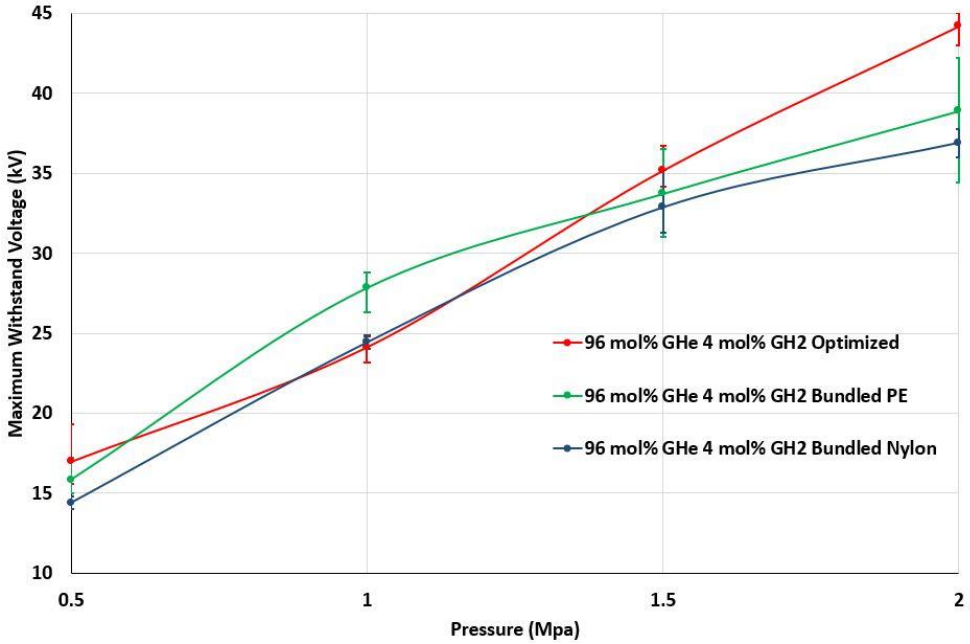

Figure 44: Intrinsic breakdown and surface flashover voltage for various pressures for optimized and bundled spacers S-GIL designs in 4 mol% H2 helium-based gas mixture at 77 K

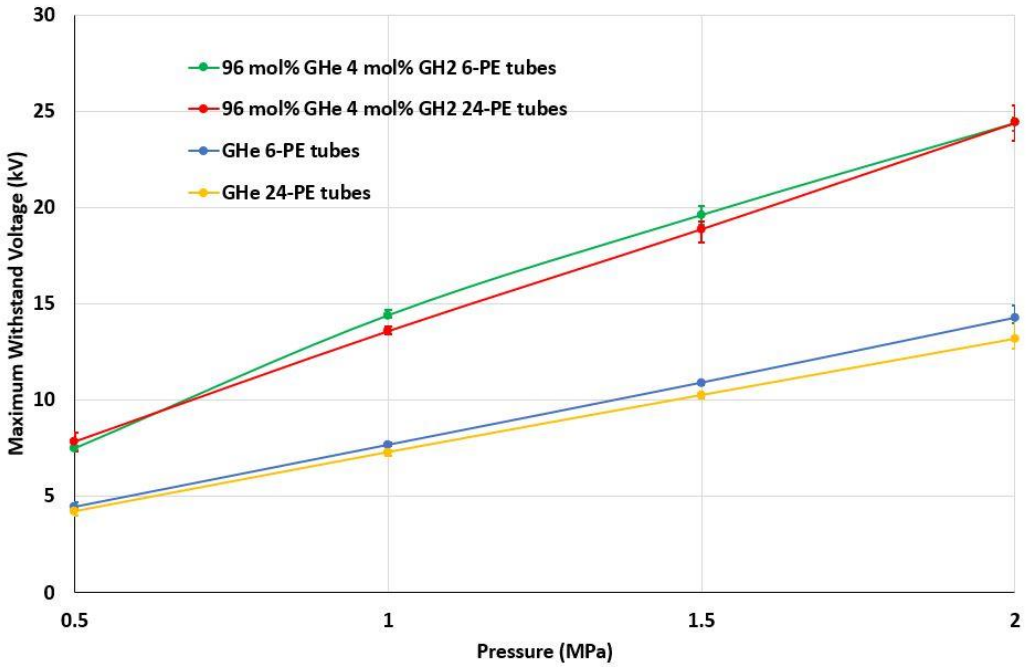

Figure 45: Performance of the 6 PE bundled tubes S-GIL design compared to 24 PE bundled tubes S-GIL design for GHe and 4 mol% at room temperature

The differences in the results of the 6 bundled tubes S-GIL design based on the tube material is shown clearly for the stronger gas species, the 4 mol% of H_2, and for both gases at 77 K since the gas density increases at 77 K to approximately 3.7 times for the same pressure value at room temperature resulting higher dielectric strengths, as shown in Figure 42-44. Analyzing these results yielded a conclusion regarding to material, and consequently regarding to the materials' relative permittivity values. It was expected that the design utilizing PTFE tubes will yield the highest surface flashover voltages, then PE and lastly the Nylon since AC field was applied. The experimental data supported the prediction. It was noticed that for PTFE, the material showed fast degradation after repeated measurements, and hence, it was decided not to continue the experiments with PTFE tubes. The experiments with PE and Nylon resulted in reproducible and consistent results, and the performance of the 6 PE tube S-GIL design is better than the samples with Nylon tubes due to lower relative permittivity of PE.

For the 24 tubes S-GIL design, PE material was selected since it showed reasonable sample degradation rate and the best performance. Thus, the data collected for 24 PE tubes S-GIL design (with outer diameter of 6.35 mm for each tube) were compared to the 6 tubes S-GIL design (with outer diameter of 12.7 mm for each tube), as shown in Figure 45 and 46. It was expected that the

results for surface flashover will be similar. This due to the fact that the creepage distances for both designs are the same. That came true for the room temperature case, but for cryogenic temperature, the 24 tubes S-GIL design demonstrated higher dielectric strength. Material shrinkage at 77 K could be the reason behind that. Since the tube in the inner layer might not touch the adjacent tube in the outer layer due to shrinkage, the small gap forces the spark to flow in the gas to close the path causing a higher breakdown voltage. This also could be the reason behind the lower sample degradation rate after many measurements that the 24 tubes S-GIL design showed compared to the 6 tubes design.

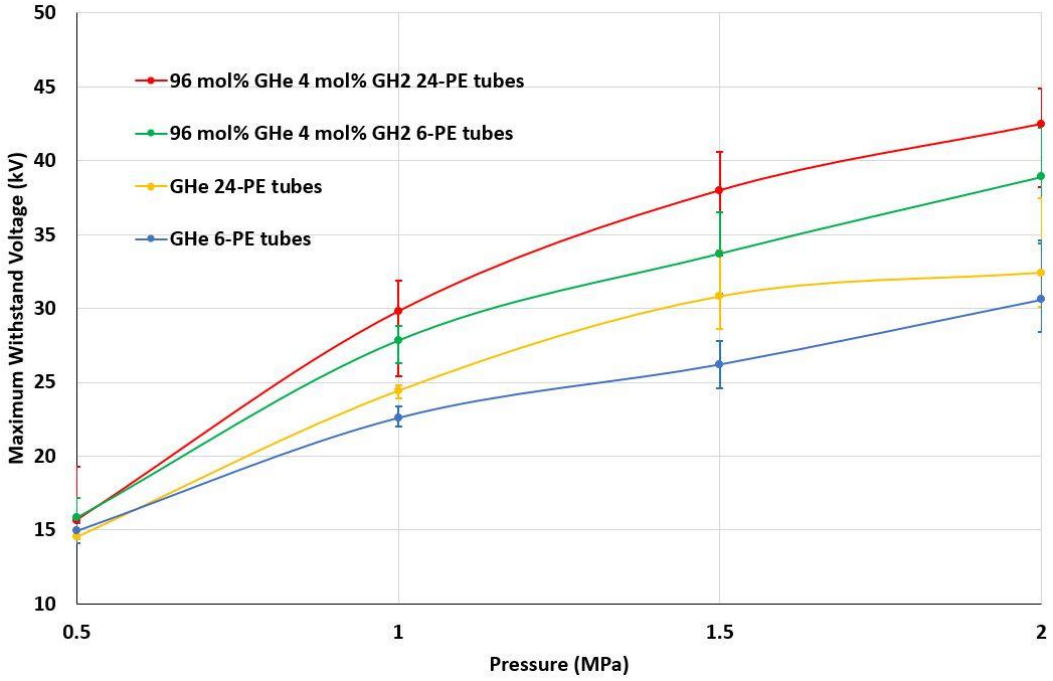

Figure 46: Performance of the 6 PE bundled tubes S-GIL design compared to 24 PE bundled tubes S-GIL design for GHe and 4 mol% at 77 K

Another conclusion can be drawn from Figure 45 and 46. At room temperature, the 80% increase in surface flashover voltage was shown for the 4 mol% H_2 helium gas mixture compared to pure helium. However, this relationship does not hold for the 77 K since the surface flashover voltage involve other factors. These factors resulted from the interface between two different dielectric materials, gas and solid materials, and surface flashover does not depend just on the gas dielectric strength. However, all the results showed that with the increase in gas density, by increasing the pressure, an increase in the surface flashover strength is obtained. However, the

relation between surface flashover strength at room temperature and cryogenic temperature for the same gas density is not clear like intrinsic BD. Thus, and for these reasons, a detailed surface flashover study was needed for better understanding of that phenomenon, presented in Chapter 7.

Finally, in general, at room temperature, both designs showed breakdown voltages of around 14 kV for GHe and 20-25 kV for 4 mol% H_2 helium gas mixture, and at cryogenic temperature of 77 K, 22-35 kV for GHe and 37-44 kV for 4 mol% H_2 helium gas mixture at 2 MPa. Figure 47 below depicts the surface flashover locations and traces for selected samples.

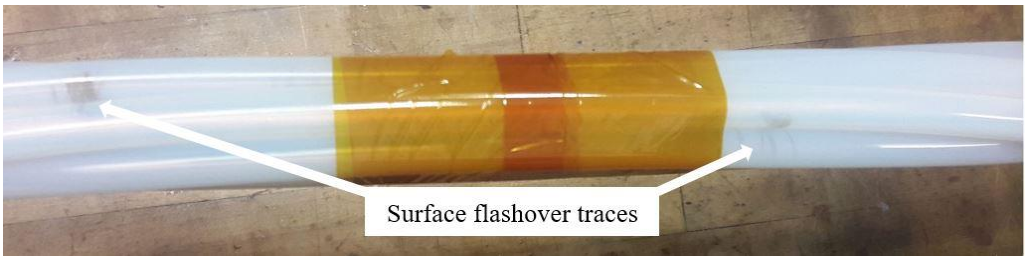

(a)

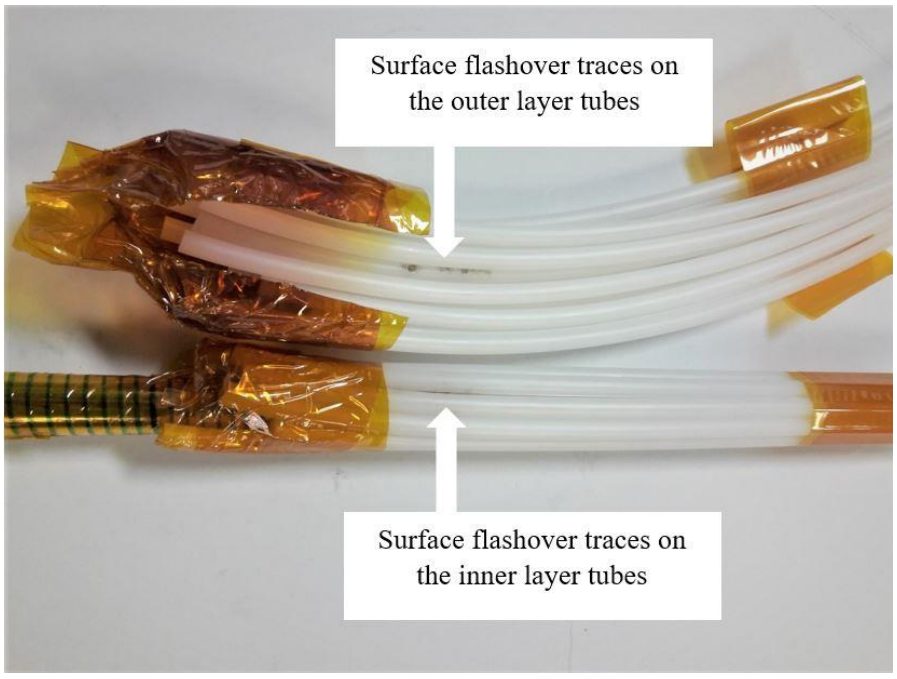

(b)

Figure 47: Traces due to surface flashover on bundled insulating tubes of the S-GIL cable after performing the experiment (a) 6 PE bundled S-GIL (b) 24 PE bundled S-GIL

5.5 Chapter Conclusions

S-GIL designs open the door for employing gases as the cryogens for HTS power cable applications. The removal of the solid insulation offers many advantages including increasing PDIV and taking advantage of gas mixtures with higher dielectric strength compared to pure GHe.

Different spacer designs with commercially available tubes were tested and the results discussed. The results for experimental characterization for the dielectric strength of the different bundled spacer tubes S-GIL designs have been presented. PE material is recommended for spacer tubes when conducting repeated, as it does not degrade as quickly as PTFE. The results revealed the possibility for utilizing bundled tubes gas-cooled S-GIL design in medium voltage power cables, especially for transportation application since they can provide the required high-power density.

It was shown that employing stronger dielectric gas leads to higher dielectric strength for the bundled tubes S-GIL electrical insulation system. Using higher pressures, which results in increased gas density also leads to higher dielectric strength. The electrical insulation system failure for bundled tubes S-GIL designs occurred in the form of surface flashover. However, surface flashover strength depends on additional factors beyond the intrinsic dielectric strength of the gas medium. These results motivated the investigation of the relationship between surface flashover phenomena at room and cryogenic temperatures on a fundamental level for a better understanding for this insulation system voltage level limitation. Chapter 7 discusses the surface flashover investigations.

For design feasibility, it is expected that the tubular insulators are wrapped around the conductor helically for long cables to ensure concentric location of conductor and to avoid separating adjacent spacers due to gravity or at cable bends.

CHAPTER 6

LIQUID NITROGEN COOLED SUPERCONDUCTING POWER CABLE WITH NO SOLID INSULATION

6.1 Introduction

As demonstrated by the experimental characterization results of its electric insulation system in Chapter 5, bundled spacer tubes S-GIL design has the potential to go to higher voltage levels. The two gas species, pure helium, and 4 mol% H_2 and helium mixture, used in the S-GIL showed promising results and the design benefits from higher dielectric strength of the gas medium. The direct relationship between the dielectric strength of the cryogen and the voltage levels achieved by the model S-GIL cables motivated the investigations presented in this chapter. This chapter describes the tests on the S-GIL design with liquid nitrogen (LN_2) as the cryogen; LN_2 has a minimum of 5 times strong dielectric strength at 77 K, if bubble formation is prevented, compared to GHe in a uniform AC field at 1.0 MPa [43], [44]. Besides shedding more light on the possibilities of S-GIL design, the investigations presented in this chapter pave a way for a new design for HTS cable that is cooled with liquid nitrogen and does not use any solid insulation on the cable.

As discussed in Chapter 1, HTS cable technology is a potential solution for power transmission and distribution. As discussed in Chapter 2, HTS cable technology offers efficient long-distance power transmission system for integrating the renewable energy sources that are typically located far from the urban load centers and for also interconnecting different power grids. Liquid nitrogen was considered as the cryogen for the majority of HTS power applications due to its low cost and large heat capacity. LN_2 cooled AC and DC HTS cables have been demonstrated in electrical power grids in a point-to-point configurations for short distances, and a few of them are currently in operation [110]–[112]. Lapped-tape insulation was used with LN_2 as the dielectric medium in all the designs and the HTS cable covered with the insulation sits directly on the cryostat at ground potential. Some LN_2 cooled HTS cables used a more compact design that utilizes one cryogenic envelope for all the poles/phases. Such configurations are used for medium and low voltage applications. Solid insulation was used between the phases and on the whole cable. Examples for these projects are the coaxial DC HTS cable, Saint-Petersburg, Russia (20 kV,

2.5 kA, 2.5 km) [113], [111], and the triaxial 3-phase AC HTS cable, Columbus, Ohio, USA (13.2 kV, 3 kA, 200 m) [112]. A coaxial DC dipole is currently in progress by our research group.

Other HTS power cable projects are considering GHe cooled HTS cables because of GHe allows lower temperature operation and the ability to carry a higher amount of current at lower operating temperature. The Best Paths project in Europe is an example of GHe cooled HTS cables [53].

The design presented here eliminates the solid insulation and uses liquid nitrogen as the sole insulation medium, resembling the S-GIL except for the fact that the cryogen is LN2 instead of GHe.

The liquid nitrogen cooled solid-insulation-free HTS cable design investigated here offers a simpler design for LN_2 cooled HTS cables. LN_2 being a stronger dielectric compared to GHe allows designs that support higher voltages and hence higher power transmission capacity for the given ampacity. Additionally, LN_2 is abundant and less expansive, and it does not demand high pressure operation.

Another factor that affects the total cost of long-distance power grid application is cryogenic heat transfer. The cryogenic systems that are used for HTS power applications suffer from low efficiency (<50% of Carnot, for Turbo-Brayton cryocoolers [69], [70], [72], [73]). Therefore, a cooling station is needed for every 5-10 kilometers [114]. That adds significantly to the total cost of HTS transmission systems. The distance between cooling stations depends on several variables. However, if there is a way to increase the distance between the cooling stations, the total cost goes down significantly. Liquid nitrogen cooled solid-insulation-free HTS design provides direct contact of the cryogen to HTS conductor. This is an important benefit for managing the thermal aspects of the cable, particularly during a fault or a quench. For conventional HTS cable designs, the lapped-tape insulation forms a thermal insulation barrier that causes the formation of hot spots generated due to the cable heat load (e.g. the AC losses) on the HTS conductor. Therefore, the no-insulation design offers a faster and more efficient way of removing the heat in the cable system, and that consequently reflects on increasing the distance required between the cooling stations of the cable system for the same allowable temperature gradient, ΔT. Therefore, liquid nitrogen cooled solid-insulation-free HTS design is a promising solution for terrestrial power grid applications, and it can be the key solution for the envisioned cross-country HTS cable that was proposed in Chapter 2.

Another application that the design concept can provide a promising solution is for transportation that uses liquid hydrogen cooled HTS cables. For instance, NASA N3-X aircraft concept is investigating and developing liquid hydrogen-cooled HTS cables since the aircraft uses stored liquid hydrogen as the coolant and the evaporated gas as fuel [8]. Thus, the aircraft microgrid power cables can be part of the fuel storage system while liquid hydrogen (LH_2) is serving as the dielectric medium. At atmospheric pressure, with the presence of bubbles, LH_2 has a dielectric strength of 9.4 kV/mm at 20 K [115]. LH_2 facilitates cooling of HTS devices to 15-30 K [2]. These temperatures allow HTS conductors to carry up to 8-10 times the ampacity possible at 77 K (extrapolating the curve shown in Figure 6, Chapter 1 [22]). However, for this research work, no liquid hydrogen cooled HTS cable was tested due to safety concerns.

Closed loop, open loop, and hybrid LN_2 cooling systems have been used for the existing HTS power grid cables. All the cables use pressurized and subcooled liquid nitrogen to prevent bubble formation. The dielectric strength of liquid nitrogen has been reported to be 19.6 kV/mm when bubble formation is prevented [44]. However, the dielectric integrity is disrupted with the presence of bubbles, and the dielectric strength is reduced to half if bubbles are present [45]. At atmospheric pressure, liquid nitrogen boils at 77 K, and pressurizing and subcooling suppresses bubble formation and increases the dielectric strength of the LN_2. For example, the boiling point increases by 20 K when pressurized to 0.5 MPa [46]. Based on these facts, an experimental setup for HTS cable characterization under pressurized LN_2 for breakdown voltage has been prepared for 0.1 MPa (1 bar) and 0.2 MPa (2 bar).

6.2 Measurements in Pressurized Liquid Nitrogen

6.2.1 Experimental Setup and Results

For testing the dielectric strength of the solid-insulation-free LN_2 cooled HTS cable in pressurized LN_2, modifications have been made to the top plate and stainless-steel piping system of the pressure vessel that has been used for the experiments on gas-cooled cables. The 3 gas pipes needed for gas inlet/outlet and pressure gauge connection were not suitable for the measurements planned for the pressurized and subcooled cable. Modifications were made to the top plate and six pipe connections were included for: (i) LN_2 in, (ii) LN_2 out, (iii) gas in, (iv) gas out, (v) gas gauge, and (vi) extra outlet that can be used for safety if needed. In addition, a relief valve was connected to the gas in/out pipe to release excessive pressure built up. Furthermore, a needle valve was

inserted in the gas in/out connection to stop the liquid to go up in the gas pipe. A sketch of the experimental set up is shown in Figure 48, and a photograph of the vessel used and stainless-steel piping system is shown in Figure 49.

Regarding cable preparation, a new sample was prepared with 6 PE bundled tubes HTS cable design. 6 PE tubes, with outer diameter of 12.7 mm, were wrapped around the conductor, with outer diameter of 12.7 mm, with the help of Kapton tape to fit into the 39 mm copper tube, which acts as the cable cryostat at ground potential. The tubes surrounding the conductor ensure the position of HTS conductor at the center of the cryostat, as was done for bundled tubes S-GIL

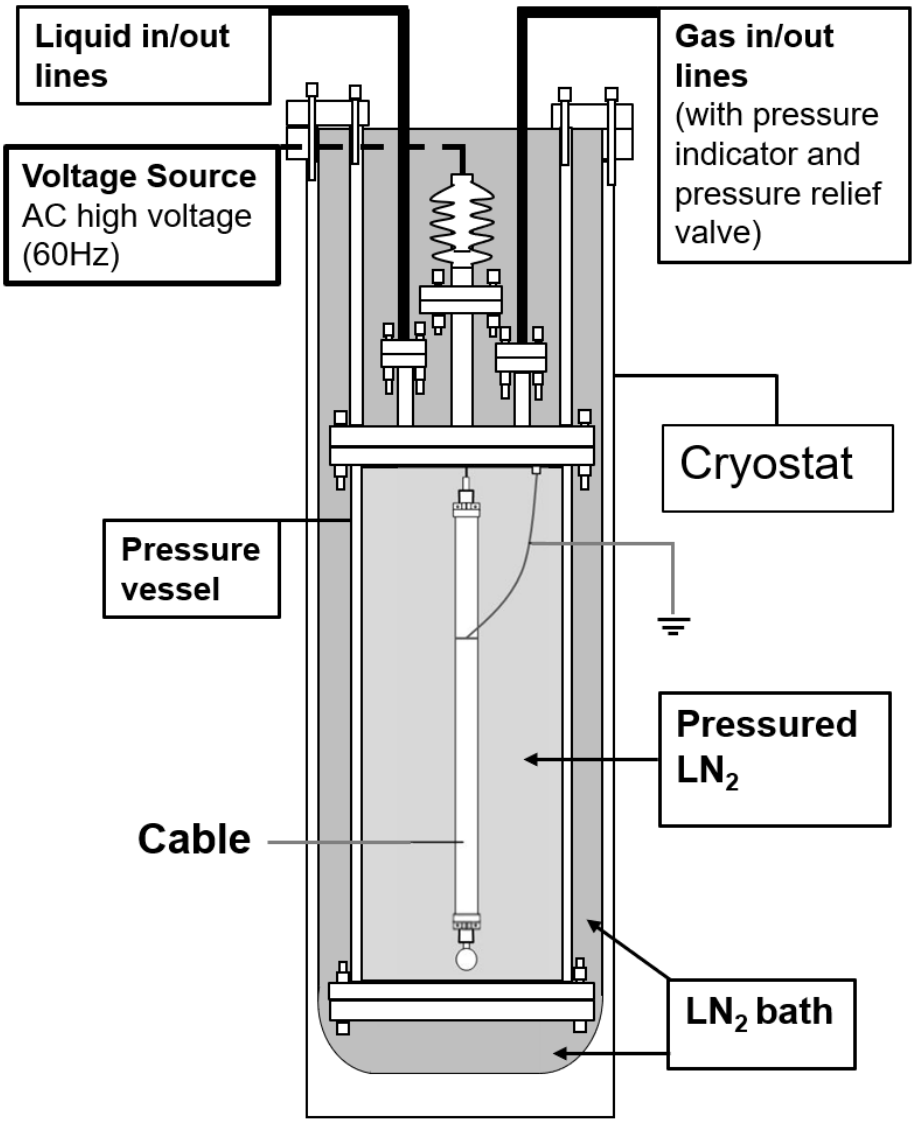

Figure 48: Pressurized liquid nitrogen experimental setup sketch

experiments. The cable was attached to the current lead which makes the high voltage connection through the bushing, and the copper tube was connected to the lower side of the top plate flange to make the ground connection. Afterward, the vessel was sealed tightly. Due to concerns that the air inside the vessel could contain some moisture, which turns into ice when cooled down, and that might cause surface flashover at a lower voltage levels, the vessel was filled with gaseous nitrogen

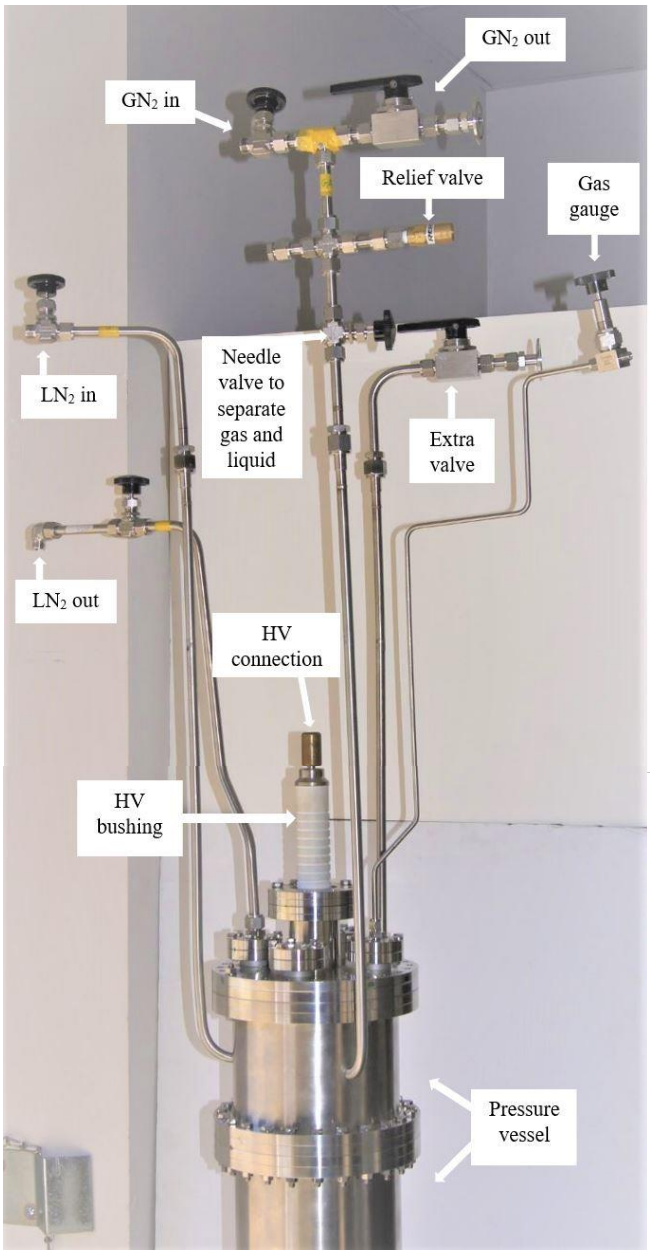

Figure 49: Pressure vessel with all gas/liquid connections

(GN_2) at 2 MPa at room temperature. GN_2 helped to absorb the moisture and to check if there are any leaks. Then, the GN_2 was flushed out and vacuumed, which helped also in removing any impurities.

Before cryogenic temperature high voltage testing, room temperature experiments were performed with GN_2 at 0.5 MPa. The S-GIL design has not been tested with GN_2 before, and the data was needed to have baseline data to compare to LN_2 results. Accordingly, the results for LN_2 can be judged against GN_2 as the insulation medium. Three measurements were taken with GN_2 to minimize sample degradation before the measurements in LN_2. The results on GN_2 insulated cable showed that for the design, the maximum value of 35.9 kV and an average of 32.3 kV. The results are as expected according to the given relative dielectric strengths of GHe and GN_2 since GN_2 is much stronger dielectric than GHe.

In addition to modifying the pressure vessel, a required procedure was needed to be taken into considerations for filling the vessel with LN_2 without any contamination. First, the vessel was left filled with GN_2 at 0.4 MPa, which was calculated according the pressure shrinkage ratio of around 3.7 between room temperature and 77 K to make the vessel at a pressure value close and a little bit higher than the atmospheric pressure at 77 K. Then, the vessel was immersed into the LN_2 bath in the external cryostat. This decreased the pressure of GN_2 in the vessel to 0.111 MPa, which is a little bit higher than atmospheric pressure. The slight positive pressure ensures that the air does not enter the vessel during the LN2 filling process. The hose connected to the LN_2 dewar was also flushed of any air.

After filling the vessel with LN_2, liquid out port was left open for the experiments under atmospheric pressure, but closed for the experiments in pressurized LN_2.

Preventing bubble formation was achieved in the pressurized LN_2 (to 0.2 MPa) experiments by immersing the pressure vessel/experimental chamber in the outer open LN_2 cryostat at 77 K. The LN_2 in the pressure vessel has an elevated boiling point of ~80 K but is kept at 77 K by the LN_2 in the outer cryostat, thus maintaining the LN_2 in the inner vessel in pressurized and subcooled state to prevent bubbles.

The experiment was performed using the Haefely test kit inside the Faraday cage. The ramp rate for the AC voltage (60 Hz) was set approximately at 666 V/s. For the experiments in boiling LN_2 (at 0.1 MPa, 77 K), the 5 measurements performed yielded a maximum of 45.2 kV (rms) and an average of 39.8 kV (rms). In the experiments performed in pressurized and subcooled LN_2

(0.2 MPa, 77 K) the breakdown occurred external to the pressure vessel due to the limited standoff/clearances among the HV connection on the top of the bushing and metal supports. The highest voltage reached breakdown outside the pressure vessel was 55 kV (rms, 60 Hz), suggesting that the cable would have reached higher voltages if the experimental limitations were not encountered.

6.2.2 Analysis

Tests of S-GIL design at room temperature with filling the design with GN_2 as the insulation medium is promising. The higher dielectric strength of GN_2 compared to GHe leads to a better performance of the cable.

The experiments on S-GIL with boiling LN_2 at 77 K, as the insulation medium, revealed that the performance is better than that of the GN2 at room temperature and 0.5 MPa. Again, the results indicate a direct relationship between the dielectric strength of the medium and the performance of the S-GIL. For the S-GIL experiments in pressurized LN_2 , the performance is even better (> 55 kV), but the actual voltage could not be measured due to the limitations of the experimental setup for voltage > 55 kV. However, the results support the conclusion drawn from G N_2 and boiling LN_2 experiments that higher dielectric strength of the insulation medium has a direct impact on the performance of S-GIL.

The experimental set up was disassembled to analyze the problem that caused the limitation to 55 kV. It was found that the cable is clean without any charring or burn marks indicating the absence of surface flashover on the PE tubes. Unlocking the sealed connection of the bushing showed marks of pitted spots on the rod of the high voltage feedthrough suggesting the limitation was the constrained size of the bushing where gaseous nitrogen is collected. Figure 50 shows the pitted marks on the conductor of the high voltage bushing. That explained the results obtained for the two pressure levels as explained below:

For the case of 0.1 MPa, LN_2 vapor was trapped under the top plate and caused the breakdown to occur under the bushing where the dielectric strength is less than the cable dielectric strength. When the pressure was increased for the 0.2 MPa, the vapor/gas dielectric strength increased. The breakdown did not happen at that location nor on the cable, but it happened outside the vessel due to our experimental lab setup voltage level limitation.

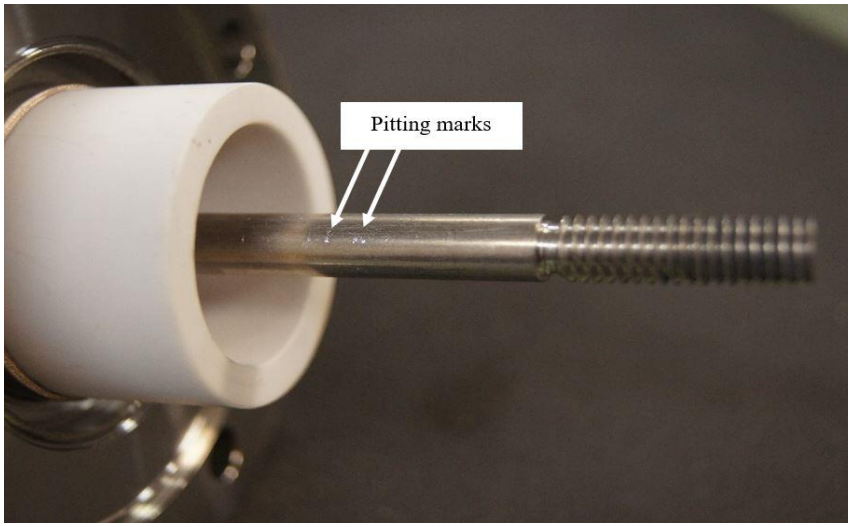

Figure 50: Pitting marks on the current lead part extended under the bushing

6.3 Experiments on S-GIL in Boiling Liquid Nitrogen

6.3.1 Experimental Setup and Results

With the experience in the previous set of experiments in the sealed pressure vessel, another series of experiments were conducted in open LN_2 bath that eliminates some of the experimental challenges encountered. Removing the pipes of top plate of the pressure chamber was expected to eliminate some of the space constraints. Thus, all top plate gas lines were removed.

Two test cable arrangements were prepared, one was the optimized S-GIL design with no spacers with the 39 mm diameter copper tube representing the cable cryostat, and the other was a new 6 PE tubes design sample. The two cable arrangements with a close view for the opening in the bushing flange, which is meant to let the trapped vaper/gas escape, are shown in Figure 51. These experiments still encountered problems with breakdown happening external to the samples/pressure vessel. As will be mentioned in the "future work" section, the experimental set up needs to be changed to reach > 55 kV.

6.4 Chapter Conclusions

LN_2 was used as the cryogen and insulation medium in S-GIL, instead of a gas, to examine the dielectric strength limits for the insulation system of the bundled spacer tubes S-GIL design. The results showed that there exists a direct relationship between the dielectric strength of the

insulation medium and the performance of the HTS cable. S-GIL performance increases with the increase of dielectric strength of the insulation medium which is the cryogen used.

The solid-insulation-free liquid cooled HTS design has the potential to be used for applications that use LN_2 or LH_2. Electric transportation applications will benefit from such cables.

The absence of solid insulation offers better heat transfer, minimal degradation during a breakdown event, and easier manufacturing.

(a) (b) (c)

Figure 51: (a) Optimized cable design experimental arrangement (b) bundled tubes spacers cable design experimental arrangement (c) closer view for the opening in the bushing flange connection

CHAPTER 7

SURFACE FLASHOVER ON SOLID INSULATORS IN GASEOUS MEDIA AT CRYOGENIC TEMPERATURES

7.1 Introduction

The development of high temperature superconducting (HTS) power device technology holds promise to provide high-power density solutions in the generation, transmission, and distribution of electricity [2]. HTS technology offers power densities 3-5 times greater than conventional technology allowing significant space and weight reductions to be achieved [1]. Several cryogens are being investigated for HTS devices. While liquid nitrogen is the preferred cryogen for HTS cables for electric utility applications, gaseous helium is a potential candidate for the applications that require lower operating temperatures to satisfy the high-power density requirements. GHe is preferred when HTS devices have to operate in confined spaces and when operating temperature lower than 65 K is required. Low operating temperatures are also required to take advantage of MgB_2 superconductor which has to be used at temperatures < 20 K [21]. The US Navy has a preference for using GHe as the cryogen since it has a larger operating temperature range (4-80 K) and reduced risk of asphyxiation hazard in the event of a cryogen leak in a confined space when compared to LN_2 [15]. The large operating temperature range for GHe allows connecting multiple devices in a single cryogenic circulation loop to achieve system level efficiency [91].

Typically, HTS devices cannot be subjected to factory acceptance test because the cryogen is part of the insulation system and has a significant impact on the dielectric properties of the insulation system. The ability to characterize the electrical insulation system of HTS devices at room temperature would be beneficial to provide consumer confidence towards this developing technology and if problems are identified in the room temperature testing stage, it is easier to address them. If one can test the insulation systems at room temperature and estimate their behavior at cryogenic temperature, it would reduce the cost, effort, and time to explore novel insulation designs for HTS devices. This would accelerate the development and maturation of GHe cooled HTS device technology.

Our previous research on investigating insulation techniques and materials for GHe-cooled HTS power devices focused on the intrinsic breakdown strength of GHe and how GHe based mixtures containing small mol% of hydrogen and/or nitrogen can lead to significant improvements in the dielectric strength when compared to pure helium gas [100], [116]. As part of the research, we also confirmed that the intrinsic breakdown strength of GHe scales with the mass density which combines the effect of pressure and temperature [93].

The dielectric systems in HTS power devices are made of solid insulation components and support structural components. Often, surface flashover at structural components is the limiting factor of high voltage designs of electrical devices. For instance, for the superconducting gas insulated line (S-GIL) [41], surface flashover is likely to occur on the surface of the insulators that serve as spacers to position the HTS conductor at the center of the cryostat. Hence, the ability to characterize surface flashover phenomenon at room temperature and relate it to cryogenic temperature operation would be valuable. Ability to understand surface flashover characteristics at room temperature is an economical way of exploring various design options and materials selection.

Surface flashover consists of three stages [117]. There is a broad agreement on the first stage (the initiation of the surface flashover) which begins by the emission of the electric or thermal field electrons from the cathode triple junction. The electrons emitted primarily from the triple junction multiply while traveling across and through the insulator surface by secondary electrons emission, and that results into releasing the gas molecules that were absorbed by a thin layer of the insulator surface. The most accepted mechanisms for this stage are the secondary electron emission avalanche (SEEA) or the electron cascade on the insulator's surface [118]–[120]. There is a general agreement on the final stage – discharge – which is the persistence of the SEEA eventually yields partial ionization of the gas that is desorbed from the surface leading to a complete breakdown in the form of a surface flashover.

This chapter discusses the design of surface flashover experiments in the gaseous environment at room temperature and 77 K and at various pressures and the results of the experiments to understand the role of the dielectric strength of the gas medium on surface flashover voltages.

7.2 Experimental Setup

Currently, no standard method to characterize surface flashover has been established. There have been a few reports of surface flashover experiments at cryogenic temperatures [43], [121].

The purpose of the experiments conducted for this dissertation is to understand the effect of the dielectric strength of the gas medium on the surface flashover voltage and to see if the temperature has any effect on the phenomenon. Experiments were conducted at room temperature and at cryogenic temperatures in the same gas medium and solid surface combination. The design that was implemented would minimize the probability of electric field enhancement caused by thermal contraction of the experimental components.

The experimental set up consisted of a planar insulator sample and two electrodes mounted on either side of the solid. The insulator sample is placed on the sample bed, and the electrodes sit tightly above the sample to ensure proper alignment and gap distance between the electrodes. The electrodes were designed to have sharp edges to concentrate the electric field at the triple junction (the meeting point of the conductor, the insulator and the gaseous insulation medium), as shown in Figure 52 (a) while the sample bed assembly is shown in Figure 52 (b).

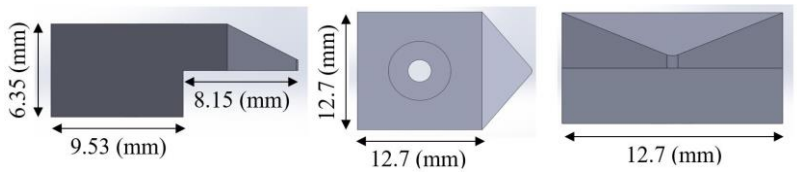

(a)

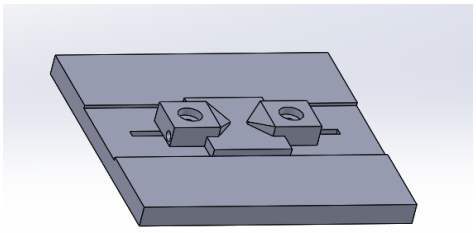

(b)

Figure 52: Schematics of (a) dimensions of electrode (b) sample bed assembly

A 3D finite element analysis using COMSOL was performed to analyze the electric field distribution for the proposed electrode design. Of particular interest was verifying the electric field

enhancement at the triple junctions. For the electric field model, AC/DC interface, electric currents physics and stationary study were selected. An extremely fine mesh resolution was chosen for the whole model except the electrodes since there is no electric field inside them. The insulator specimen was chosen to have an electrical conductivity of 10^{-18} S/m and relative permittivity of 2.1 as generally accepted values. The electrical conductivity and relative permittivity of the gas medium were selected to be 10^{-40} S/m and 1.0, respectively, to reflect GHe. One of the electrodes is at nominal 1 kV as boundary condition while the second electrode was grounded. Electric field distribution at the cross-section through the tips of the electrodes in colors is shown in Figure 53 while electric field distribution in grayscale with equipotential lines is shown in Figure 54.

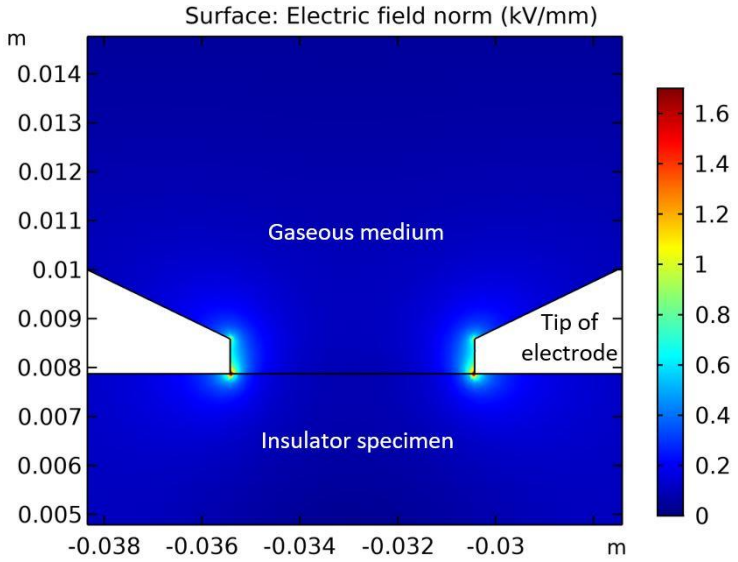

Figure 53: Electric field distribution in colored scale at the cross-section through the tips of electrodes at 1 kV

The results presented in Figure 53 verify that the maximum electric field is at the desired point, the triple junction.

7.2.1 Measurements and Results for Polytetrafluoroethylene in Gaseous Helium

The experiment setup was designed based on the model and was fabricated. The electrodes were manufactured using copper with the dimensions as noted in Figure 52 (a). A G10 platform was machined with a trench so that the solid insulation specimen can be easily aligned between the two electrodes. The samples were made from Polytetrafluoroethylene (PTFE) and cut using a waterjet.

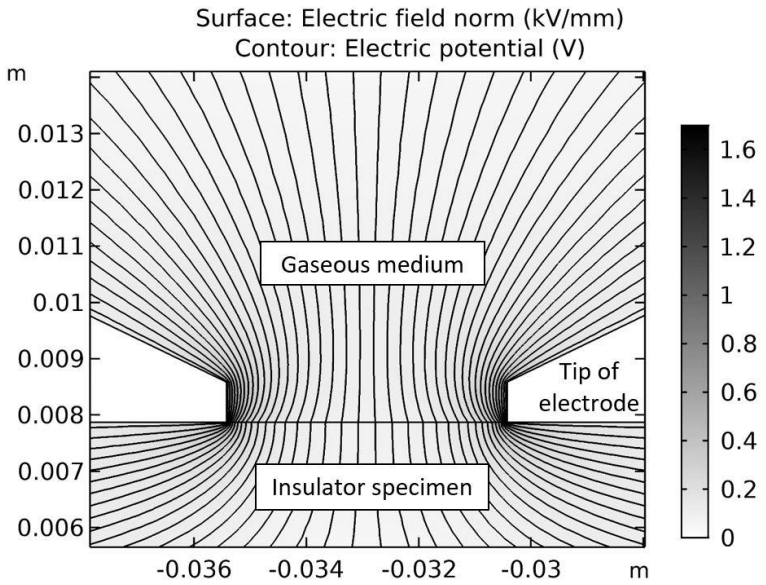

Figure 54: Electric field distribution and equipotential lines at the cross-section through the tips of electrodes at 1 kV

The experimental setup was mounted on the top plate of a pressure vessel, as shown in Figure 55 (a). Figure 55 (b) shows that one electrode was connected to the direct current (DC) high voltage source while the other electrode was connected to the ground. The gap distance between the electrodes was fixed to 4.5 mm.

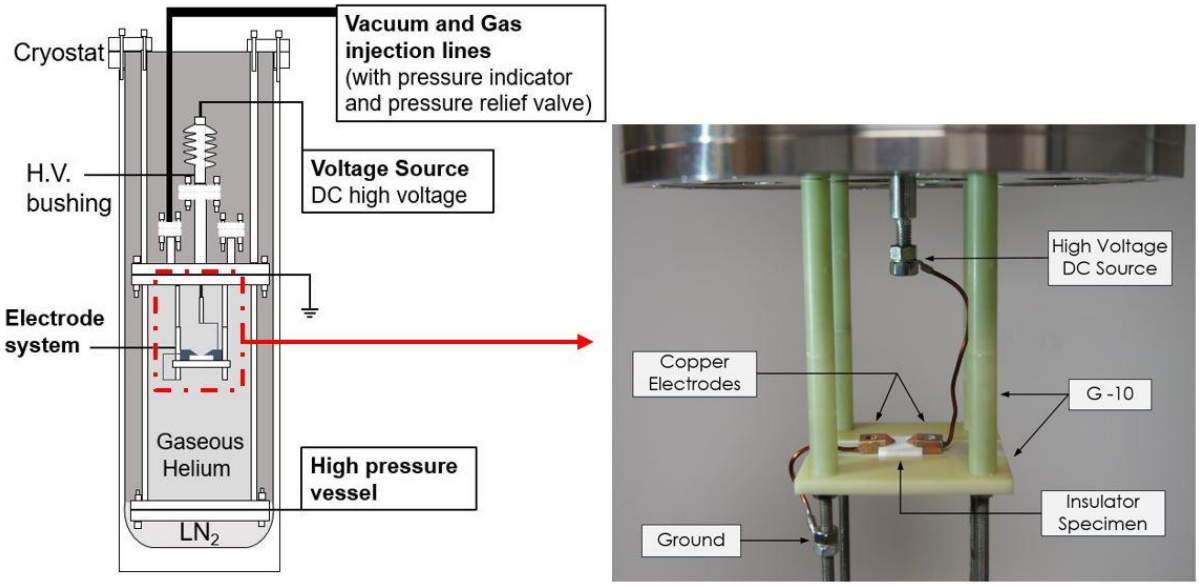

(a) (b)

Figure 55: Cross-sectional sketch (a) and close-up picture (b) of the experimental setup used to measure surface flashover strength in helium gas at cryogenic and room temperature

The pressure vessel was then sealed, and multiple pumping and high-pressure flushing cycles were performed to ensure a high purity GHe environment within the pressure vessel. Research grade gaseous helium (GHe) with a purity of 99.9999% was used to perform the measurements at room temperature and cryogenic temperature (77 K) to investigate the temperature dependency of surface flashover on a PTFE specimen in GHe medium. To ensure a stable and a uniform temperature of 77 K, the pressure vessel was immersed in a cryostat filled with LN_2, as depicted in Figure 55 (a). A uniform temperature was necessary to ensure the equivalent gas density could be accurately calculated. For all the measurements, the voltage from the DC power supply was increased at 100 V/s until surface flashover occurred. The experimental setup showing sample degradation is shown in Figure 56. The current output during the measurements was limited to 3.2 mA to minimize the damage to the sample surface during the multiple measurements. Reducing the output current of the DC power supply reduced the energy released during a surface flashover event which allowed for multiple measurements on a single sample without degradation, as shown in Figure 57.

A set of five surface flashover measurements on a PTFE sample in GHe medium were performed for each pressure of 2.0, 1.5, 1.0, 0.5 and 0.4 MPa and room temperature (289 K). For cryogenic temperature measurements, the ideal gas law was used to calculate the pressure at 77 K to maintain equivalent mass density. Thus, measurements at 77 K were performed at 0.535, 0.4,

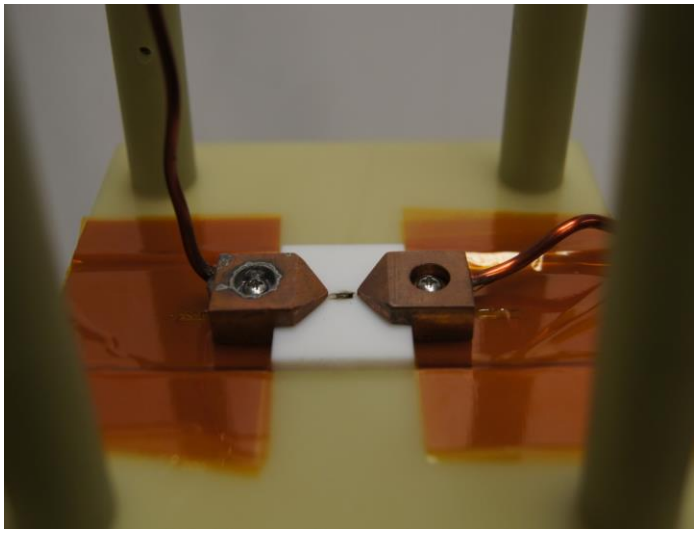

Figure 56: The experimental setup after taking measurements showing degradation on PTFE sample

0.2675, and 0.107 MPa. The results are shown in Figure 58, in which each data point was an average of five measurements.

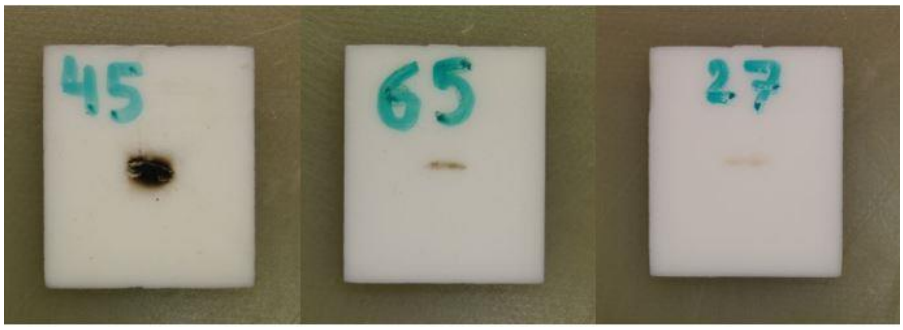

(a) (b) (c)

Figure 57: PTFE specimens with dc supply current rating of (a) 160 mA and 45 measurements (b) 3.2 mA and 65 measurements (c) 3.2 mA and 27 measurements

Figure 58 demonstrates that the results of the measurements at room temperature and cryogenic temperature were almost identical for a given mass density. Additional measurements at the extended pressure range were carried out at 77 K at 1.0, 1.5, and 2.0 MPa. Linear increase of surface flashover strength proportional to the pressure was extended at higher pressure up to

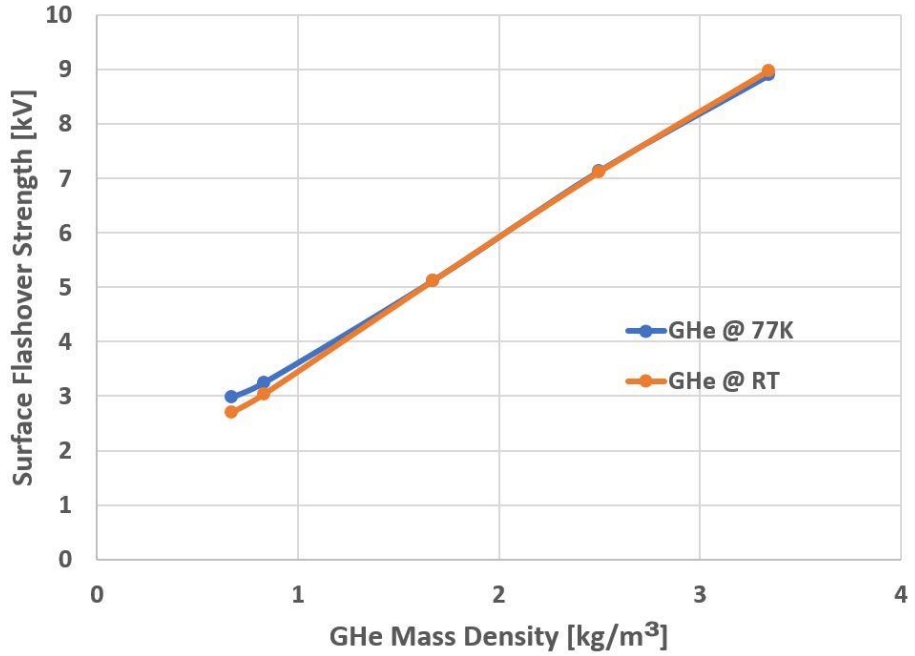

Figure 58: Surface flashover strength for GHe at room temperature and 77 K

2.0 MPa. All data obtained at cryogenic temperatures can be seen in Figure 59. Each data point is the average of five measurements. The error bars in the figure show maximum and minimum flashover voltages obtained at each pressure level.

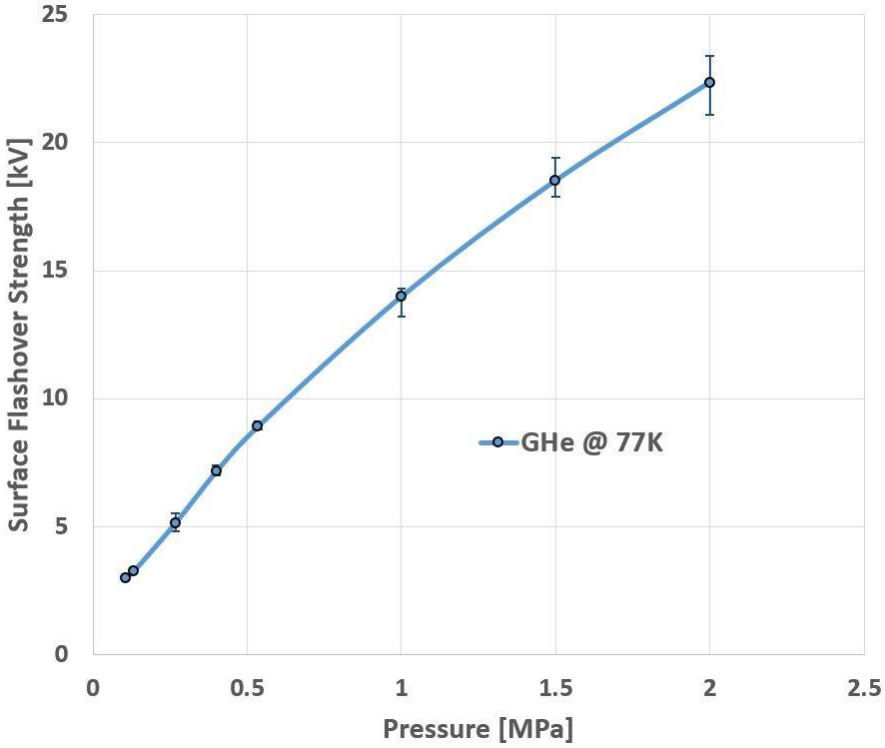

Figure 59: Surface flashover strength for PTFE at 77 K in GHe at various pressures

7.2.2 Discussion

The data shown in Figure 58 demonstrate that for a given electrode arrangement under certain pressure, electric field, solid material, and gap distance, surface flashover strength does not appear to be a function of temperature. The fact that the measurements suggest DC surface flashover is not a direct function of temperature is opposite to what has been reported in previous studies on DC surface flashover. It should be noted that where these studies differ is the gas medium in which the measurements are performed. Typically, surface flashover measurements are performed with a gas with good dielectric properties. Helium gas, however, has poor dielectric strength compared to conventional insulating materials and is considered as a useful cryogen mainly for HTS devices to take advantage of its wide operating temperature range. The relatively low dielectric strength of helium gas would lead to surface flashover occurring at lower voltages

for a given geometry than using a gas with higher dielectric strength. One of the possible explanations of this phenomenon is that the metastable energy levels of helium allow electrons to be in an ionized state where the electric potential is enhanced. Electrons at the ionized state can promote SEEA procedure on the surface and provide a path for the surface flashover easier. The ionization of the helium gas is not a strong function of temperature in the enhanced electric field, therefore, in the weak dielectric gas of helium, the surface flashover can occur without significant dependency on temperature. For the ranges of pressure and temperatures measured in Figure 58, it appears that the lower dielectric strength of helium gas has a greater influence on surface flashover than the operating temperature.

Another factor which needs to be considered is how the voltage was applied to the sample. For these measurements, a constant ramp rate of 100 V/s was used. Applying a constant ramp rate may lead to different surface flashover voltages than if the electrode connected to the DC power supply was first held at a constant DC voltage which would increase the potential of charge accumulation occurring on the sample. These variables highlight the need to determine a systematic experimental setup and procedure to characterize surface flashover for DC voltages.

It should also be emphasized that this is a preliminary conclusion that no temperature dependency exists in surface flashover when gas mass density is maintained and cannot be generalized. More experimental and theoretical validations are required before making the claim. Additionally, surface flashover needs to be understood over a large mass density range, which involves performing experiments at up to approximately 7.6 MPa at room temperature to have a comparable mass density of 2 MPa and 77 K. Other variables which also need to be considered include different gap distances, different gas media with enhanced dielectric strength. Gas mixtures of GHe with small mole fractions of hydrogen or nitrogen would allow us to perform measurements with significantly improved dielectric strength than GHe. Different insulation materials and different electric field profiles are also needed to be studied. The electrodes in this experimental setup created a highly non-uniform electric field and it, therefore, would be necessary to measure surface flashover in equivalent electric fields in which HTS devices are expected to operate. Accordingly, the plan is to continue studying surface flashover at cryogenic temperatures and gaseous media to determine if surface flashover is truly independent of temperature, for helium gas.

7.2.3 Measurements and Results for G10 in Different Gases

PTFE showed fast deterioration, and that was also observed in the S-GIL measurements. Thus, it was decided to employ a different solid material with better lower degradation rate. G10 was selected as the test material. Accordingly, G10 samples were cut by the waterjet to the desired dimensions.

As discussed in the last section, since the weak dielectric strength of GHe might have affected the surface flashover strength, the next step was to examine another gas with higher dielectric strength for better understanding of surface flashover phenomenon. It was decided to test the 4 mol% H_2 helium-based gas mixture.

At room temperature, the considered pressure levels for GHe and 4 mol% H_2 helium-based gas mixture were 2.0, 1.5, 1.0 and 0.5 MPa. These pressure levels also going to be considered for cryogenic temperature measurements. For 77 K experiments, the dielectric strength increase since the density of the gas 3.7X compared to room temperature densities. Nitrogen gas (GN_2) was also selected because it possesses a higher dielectric strength compared to the two above mentioned gases. Using different gases with different dielectric strengths can help to understand the relationship between the surface flashover voltage and the dielectric strength of the gaseous medium.

Comparisons can be applied by knowing how much the 4 mol% H_2 helium-based gas mixture and GN_2 are stronger than GHe at room temperature. For the same particle density, GN_2 has 6.7 times the dielectric strength of GHe. That means under the same conditions of pressure and temperature, GN_2 is stronger than GHe by 6.7 times [122], [123]. Additionally, 4 mol% H_2 helium-based gas mixture with 80% higher dielectric strength than GHe [40], which means the gas mixture is 1.8 times stronger than pure helium. Accordingly, GN_2 is 3.7 times stronger than 4 mol% H_2 helium-based gas mixture. However, for surface flashover strength, it was predicted that the ratios are going to be less than the above estimations due to its different mechanism, compared to intrinsic breakdown.

The sequence of room temperature surface flashover measurements on G10 specimen was to start testing GN_2, then GHe and finally the 4 mol% H_2 helium-based gas mixture. Due to the strong dielectric strength of GN_2, wide range of pressure levels (2.0, 1.0, 0.5, 0.4, 0.3, 0.2 and 0.1 MPa) were tested. For GHe, pressure levels of 2.0, 1.0 and 0.5 MPa were also tested with the same

G10 sample. For GN_2 measurements at 2.0 and 1.0 MPa, the breakdown occurred outside of the pressure vessel.

Due to witnessing high fluctuations in results for GN_2, a set of 8 measurements was taken for each data point. For the sake of consistency, a set of 8 measurements for each data point was also used for GHe although its results did not show fluctuations. The averages with the corresponding error bars are shown in Figure 60.

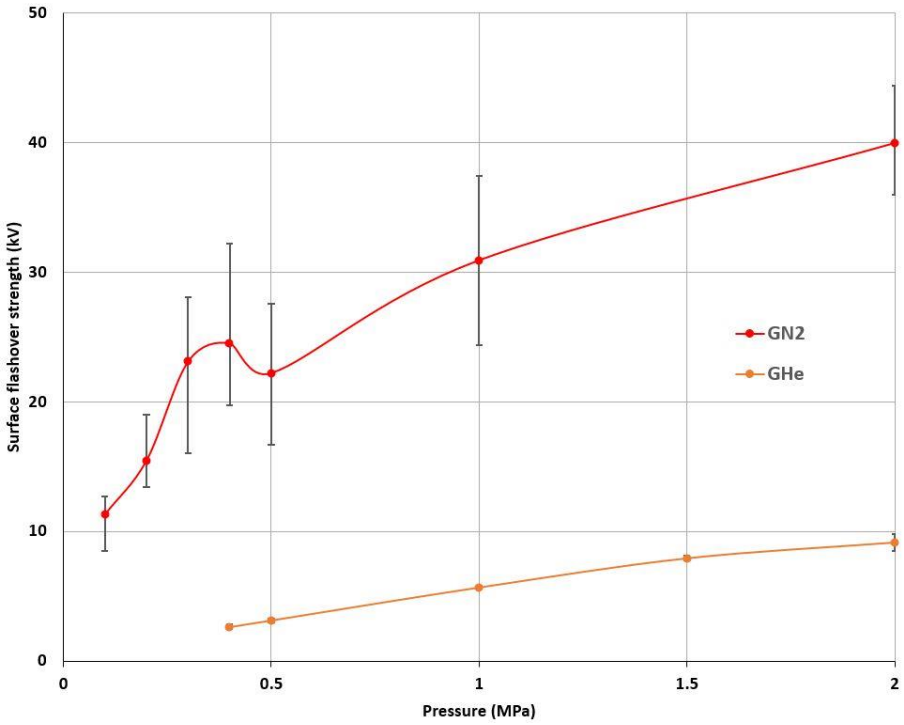

Figure 60: Surface flashover strength for GN_2 and GHe on G10 sample at room temperature

7.2.4 Discussion

As shown in Figure 60, significant fluctuation in the results was noticed at all pressure levels for gaseous nitrogen. In addition, the average value for GN_2 at 0.5 MPa was lower than those for 0.3 and 0.4 MPa. Thus, it was decided to disassemble the setup to examine the sample before proceeding to test the 4 mol% H_2 helium-based gas mixture. From examining the sample, three distinct surface tracks could be seen. It was found that the surface flashover has taken two additional paths besides the shortest straight path connecting the tips of the electrodes, as depicted in Figure 61. The figure shows that the length of the 3 surface tracks varies in distance.

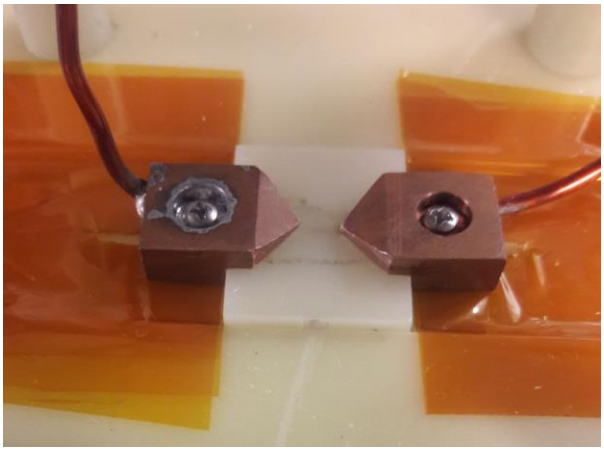

Figure 61: Surface flashover tracks with three different paths on G10 sample

The experiment setup specified a gap distance of 4.5 mm between the two points of the electrodes. Measuring the distance of the 3 surface tracks, the bottom track was approximately 13 mm, which is close to 3 times the intended creepage distance of the experiment setup. The middle surface track was approximately 4.5 mm and coincided with where the two points of the electrodes were set up. The top surface track was approximately 9 mm which is double the intended creepage distance.

These results at first seemed odd until the electrodes and experiment setup were examined in closer detail. From looking at the experimental setup, the electrodes were not making contact with the sample at the intended triple junction as the electrode tip was slightly elevated from the sample surface. From examining the electrodes, it was observed that there was not a perfect 90° angle between the electrodes and the sample as intended due to machining inaccuracies. The imperfect alignment between the insulator/electrode interface effectively changed the location of the triple point of the electrode, gas, and sample. This helps in explaining the three distinct surface tracks which all have various creepage distances. Examining all of the machined electrodes, the same defect existed for all of them.

Based on the experimental setup and machining defect of the electrodes, there were different mechanisms of breakdown according to the dielectric strength of the gas being measured. For helium gas, breakdown mechanisms occurred between the tips of the electrodes through the helium gas. As the tips of the electrodes were still in close proximity to the sample it left tracking on the surface of the sample. Although the breakdown in the gas in a path close to and parallel to the surface insulating material, it is also known as surface flashover [27].

The misalignment of the electrodes and the insulator surface also applies to the results showed in Figure 58. However, the PTFE sample only had one set of surface tracks which occurred between the tips of the electrode. It is believed that the PTFE sample was already contaminated with a surface carbon track from room temperature measurements, which formed a lower resistive path, and the 77 K measurements followed that track. We have seen this occur previously when we have used PTFE as an electrical insulator spacer for the S-GIL. Accordingly, the surface flashover voltages recorded in GHe at 77 K were similar in magnitude to the recorded values at room temperature, as was shown in Figure 58.

For higher dielectric strengths, such as when the nitrogen gas was used, it is believed that the mechanism of surface flashover occurred at where the electrode, and sample actually made contact. This would explain the surface tracks which exceeded the intended gap distance of 4.5 mm. There is a fluctuation in the nitrogen data of approximately 10 kV between the 0.3-0.5 MPa data which could be explained by the tracks being different lengths of 9 mm and 13 mm, respectively.

Having different surface flashover track lengths and different breakdown mechanisms refute the integrity of the results, and the experimental setup did not lend itself to rectify the misalignment issue. Hence, a new experimental design that can eliminate the misalignment problems was needed.

7.3 Improved Surface Flashover Experimental Setup

The improved experimental setup was designed based on the need to have an equal length for surface flashover path. Accordingly, the idea of the circle's center was proposed since the radial distance to the circumference is always equal. Thus, a 12.4 cm diameter copper disc was fabricated by cutting a copper sheet. A 12.7 mm circular hole in the center and four 6.35 mm circular holes separated by 90 degrees by the circumference were cut also by the waterjet. The center hole was made to fit the cylindrical G10 samples, which will be inserted through, and the other four holes were made to fit in the 6.35 mm threaded rods in our cylindrical G10 set that provides the structure for the setup. Cylindrical G10 samples of 12.7 mm diameter and 15 mm length that were already available in the lab were used as solid insulators. A needle electrode that its tip sits on the center of the G10 sample has been fixed and connected to HV source through the HV bushing while the

copper disc was connected to ground by the nuts fixing the set to the threaded rods, as shown in Figure 62 (a).

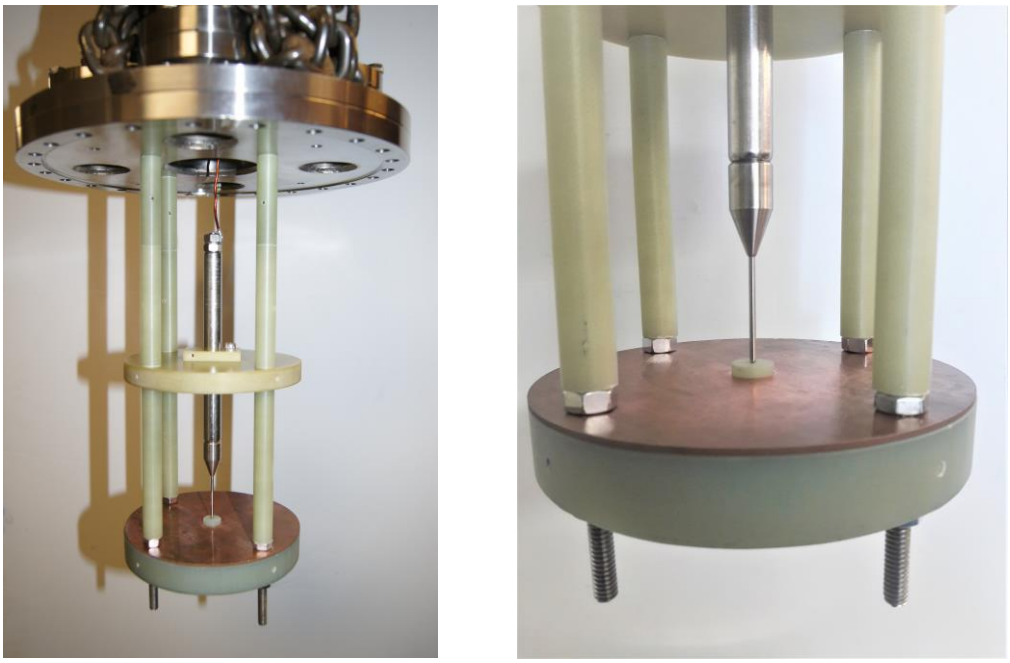

(a) (b)

Figure 62: (a) Improved surface flashover experimental setup (b) closer side view

The upper circular surface of G10 specimen sits at a higher level than the copper disc by 3.4 mm, as shown in Figure 62 (b), so the total surface flashover straight path between the tip of the needle electrode and circumference of the center hole of the copper disc is the sum of 6.35 mm, cylindrical G10 radius, and 3.4 vertical height deference, which equals to 9.75 mm.

The new surface flashover setup provides a non-uniform filed distribution and is a close imitation of the electric field distribution in actual applications, as sharp edges/defects disturb the designed uniformity of electric field of power apparatus causing surface discharges. The previous setup, with the two pointing electrodes, was a primary design, and as discussed earlier, it was designed to force the flashover to occur at the same desired path.

7.3.1 Measurements and Results for G10 in Different Gases

Three different gases (research grade gaseous helium with 99.9999% purity, 4 mol% H_2 helium-based gas mixture and nitrogen gas) were tested with G10 specimens to understand the relationship between the dielectric strength of the gas and the surface flashover voltage. Again,

GN_2 was selected since it possesses higher dielectric strength compared to the other two gases, as discussed in section 7.2.3.

At room temperature, the pressure levels used for GHe and 4 mol% H_2 helium-based gas mixture were 2.0, 1.5, 1.0 and 0.5 MPa. For GN_2 pressure levels of 2.0, 1.5, 1.0 and 0.5 MPa were used. In addition, lower pressure levels of 0.4, 0.3 and 0.2 MPa were also used to have a wide pressure range, and accordingly wide gas mass density range. This was also considered for cryogenic measurements of GHe and 4 mol% H_2 helium-based gas mixture. For these two gases, besides the pressure levels of 2.0, 1.5 and 1.0 MPa, lower pressure levels of 0.54, 0.4, 0.27 and 0.14 MPa were chosen to match the density of the two gases at 2.0, 1.5, 1.0 and 0.5 MPa of pressures at room temperature, respectively.

AC measurements were performed using the Haefely high voltage test kit, but the DC measurements were performed using the Glassman high voltage source since it has a better DC voltage profile. It was noted that after each sample replacement, the number of measurements that could be performed before sample degradation kept decreasing. When disassembled for replacing the specimens, it was observed that the surface flashover kept happening on one single track instead of distributed in many directions. The difference is shown in Figure 63. After investigation, it was found that cleaning of the center hole of the copper disc by sanding is making the hole

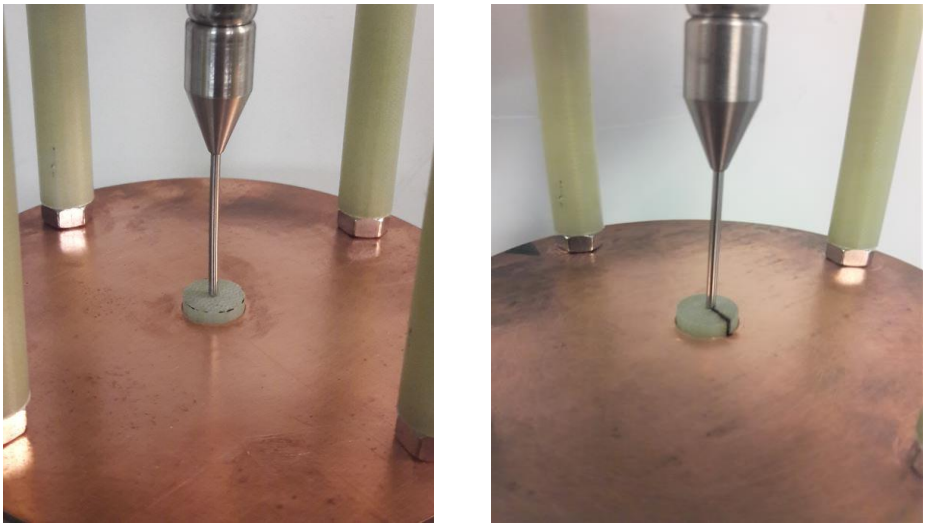

(a) (b)

Figure 63: (a) Distributed surface flashover tracks on G10 specimen (b) concentrated surface flashover tracks on one path on G10 specimen

bigger, causing the G10 sample to sit loosely in the hole. The movement of the G10 sample in the hole was making it touch the copper piece at one single point. Therefore, new copper discs were fabricated, and the sanding step was not performed when replacing G10 samples. Flashover voltages obtained in the DC and AC measurements for room temperature and 77 K are as shown in Figure 64. Each data point is an average of 5 or more measurements, but the number of measurements was limited to only 3 for each data point when fast sample degradation was observed.

7.3.2 Discussion

First, for all the results, it was shown that the DC surface flashover voltages are higher than the corresponding AC rms (60 Hz) surface flashover voltage for the same tested conditions (same gas at the same temperature and pressure).

Second, regarding the dependency of surface flashover voltage on the dielectric strength of gas, the results were compared for three gases with different dielectric strengths. The higher dielectric strength of 4 mol% hydrogen-helium mixture yielded higher surface flashover voltage than pure helium at the same pressure level at room temperature.

For both pure He and 4 mol% hydrogen-helium mixture, the 77 K measurements resulted in higher flashover voltages than the corresponding room temperature values. The dielectric strength of a gas for a given pressure is higher at 77 K that at room temperature due to the increase of gas density to approximately 3.7 times.

Surface flashover voltages in GN_2 are higher than those in helium mixture since GN_2 is 6.7 times stronger dielectric medium than pure helium [122]. Accordingly, for all the results, it was noticed that increasing the dielectric strength of the gaseous medium, either by using a stronger gas or by increasing the pressure or decreasing the temperature, increases the surface flashover voltage.

To present the relationship between the dielectric strength of the gas and the surface flashover voltage clearly, Table 9 summarizes all the data of surface flashover in the three different gas media and two different temperatures. All the values in Table 9 were normalized to GHe values. Accordingly, the increase in DC and AC surface flashover voltages were compared to the increase in the dielectric strength of the gas medium.

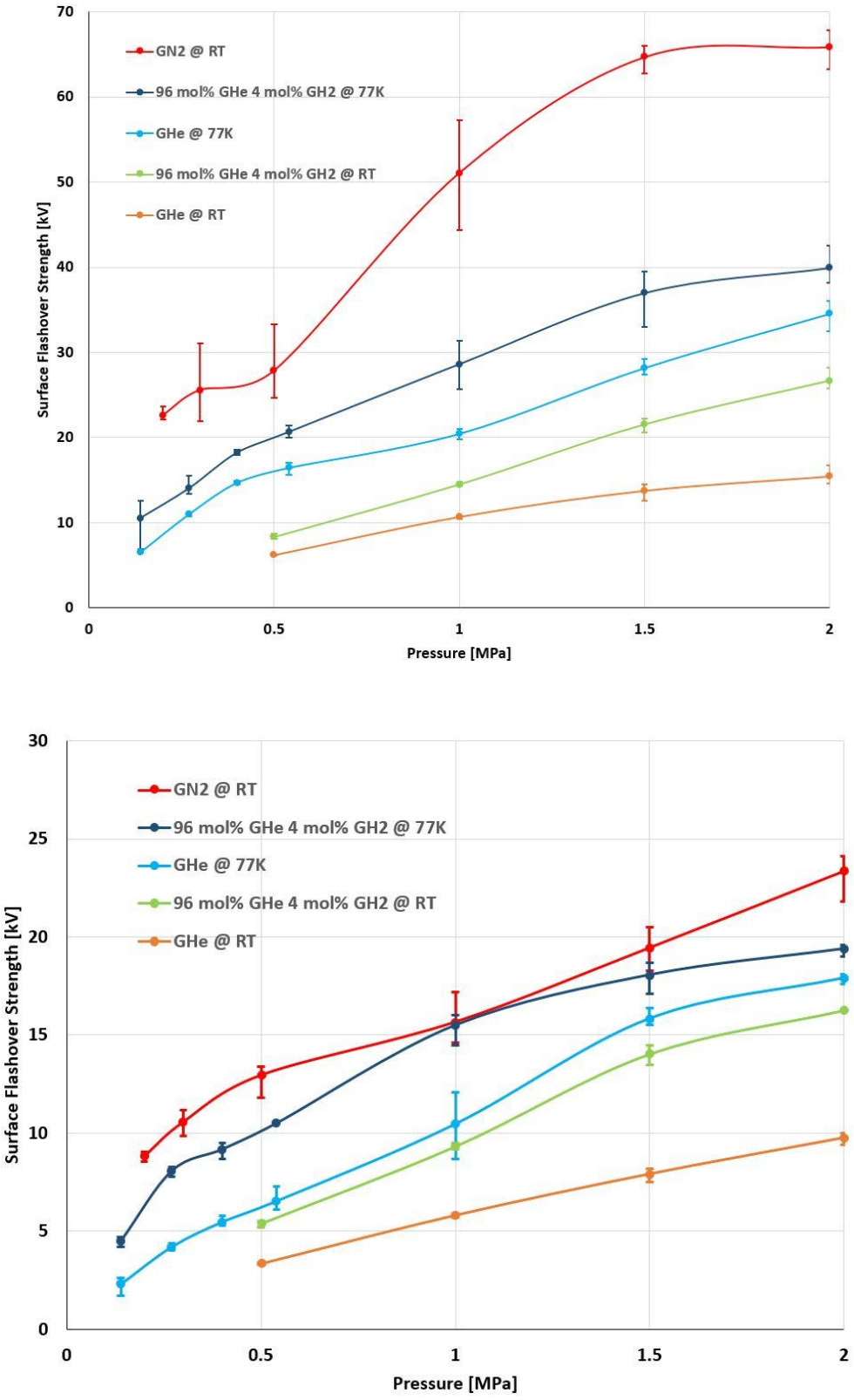

Figure 64: DC (upper) and AC rms (lower) surface flashover measurements with respect to pressure

Table 9: Dielectric strength of various gases, normalized to GHe at room temperature, and the corresponding surface flashover voltages

Gas Medium	Dielectric strength ratio	DC surface flashover voltage ratio	AC surface flashover voltage ratio
GHe at room temperature	1	1	1
4 mol% H2- 96 mol% He mixture at room temperature	1.8	1.7	1.6
GHe at 77 K	3.7	2.2	1.9
4 mol% H2- 96 mol% He mixture at 77 K	6.7	2.7	2.3
GN2 at room temperature	6.7	4.7	3.3

The comparisons in the table allow the conclusion that increasing the dielectric strength of the gaseous medium increases the surface flashover voltage. In other words, the surface flashover voltages correlate positively with the dielectric strength of the gas. However, the relationship is not linear. For example, increasing the dielectric strength 3.7 times does not yield an increase of 3.7 times flashover voltage. Additionally, the table shows that DC surface flashover voltages for all the cases are higher than the corresponding AC surface flashover voltage.

7.4 Chapter Conclusions

The surface flashover is the lower limit of the performance of the insulation system when solid surfaces and electric field gradients are present.

Surface flashover measurements were performed at room temperature and at 77 K on G10 in three different gas media at two different temperatures.

Use of He-H_2 mixtures and/or increasing the pressure and/or lowering the temperature increase the dielectric strength of the gas medium, which helps in raising surface flashover voltages but not linearly. The non-linearity of the relationship between the dielectric strength of the gas medium and the flashover voltage need to be further investigated.

CHAPTER 8

CONCLUSIONS AND FUTURE WORK

8.1 Conclusions

The research presented in the dissertation focused on understanding the dielectric insulation system limitations and some technology solutions for HTS power cables. The study investigated superconducting power cables for power transmission systems as cross-country multi-terminal DC HTS cable. This long-distance DC HTS cable offers a solution for renewable energy integration to the power grid with its high efficiency and high-power transfer capacity. It was concluded that there are still some outstanding technical challenges to realize such large HTS cable systems, but there are potential solutions for the challenges.

The main focus of the research is on gas-cooled HTS devices and their dielectric systems. The systematics of the dielectric strength of gas media were used to present a new representation of Paschen's law that relates the dielectric strength of gases to the mass density and distance. The new representation is much useful and easier to use for assessing the dielectric strength of gas media for applications that use a wide range of temperatures and pressures.

Gas-cooled superconducting power cables are being developed for electric transportation that requires high power density. Superconducting gas insulated line (S-GIL) that was proposed by the researchers in our group as a new cable design. This study advanced the idea by investigating different insulator spacer designs that use bundled tubular spacers. A series of investigations on different tube materials, number of tubes, gas media showed interesting possibilities for the S-GIL design. It was concluded that addressing the electric field enhancements using the geometry of the cable and tube materials is important. Gas-cooled HTS designs that are suitable for 20-30 kV were achieved.

To investigate the electric insulation system limits of the bundled spacer tubes S-GIL design, stronger cryogen than GHe and helium-based mixture was needed. Thus, the S-GIL design was tested with liquid nitrogen as the cryogen. Experiments with pressurized and subcooled cables showed promise. The tested design resulted in a cable that is suitable for ~ 50 kV. The full potential of the design could not be investigated due to the experimental limitations that caused breakdown outside the experimental chamber at around 55 kV.

Surface flashover strength, as the voltage threshold for the gas-cooled superconducting power cable insulation system, has been investigated. Two surface flashover experimental setups were designed and fabricated to perform the surface flashover experiments in different gas media to understand the relationship between the surface flashover voltage and the dielectric strength of the gas media surrounding the solid surface. It was concluded that enhancing the dielectric strength of the gas medium pushes the surface flashover voltages to higher values. The enhancements of dielectric strength could be either by increasing the operating pressure and/or using a stronger dielectric gas media.

8.2 Future Work

The work performed for this dissertation generated several new ideas that would extend the understanding of the dielectric behavior of gas media and their application in HTS power devices. The S-GIL studies showed the need for detailed dielectric strength measurements in non-uniform electric fields. Hence measurements in non-uniform electric fields is a fertile area of research to advance the understanding of gas media.

The solid insulator spacer materials and designs were identified as a weakness in HTS system designs. Hence the development of methods to produce new spacers both in design and materials selection is useful. We have started exploring additive manufacturing for this purpose, but this work was incomplete. Continuing the work on FDM 3-D printing as a tool to produce new composites and versatile designs of spacers would be beneficial.

The idea of solid insulation-free liquid nitrogen cooled HTS cables investigated for this dissertation is promising. The study was incomplete due to the experimental facility limitations. It would be useful to modify the system to allow measurements at >50 kV to continue the exploration of the limits of liquid cooled HTS cables that do not need any solid insulation.

Surface flashover is an underappreciated challenge in electrical power systems for cryogenic applications that are cooled with gas media. Further detailed studies of surface flashover characteristics as a function of temperature and pressure will certainly shed additional light on the topic.

APPENDIX A

PUBLICATIONS

A.1 Publications that Resulted from the Work Reported in this Dissertation

1. **A. Al-Taie**, L. Graber, and S. V. Pamidi, “Technical Challenges and Potential Solutions for Cross-Country Multi-Terminal Superconducting DC Power Cables,” in *IOP Conference Series: Materials Science and Engineering*, 2017, vol. 279, page. 012034.
2. **A. Al-Taie**, P. Cheetham, S. Satyanarayana, C. Park, J. Wei, C. H. Kim, L. Graber and S. Pamidi, "Understanding Surface Flashover Strength in Cryogenic Helium Gas for Superconducting Devices," in *IEEE Transactions on Applied Superconductivity*, vol. 29, no. 5, pp. 1-5, Aug. 2019, Art no. 7701805.
3. **A. Al-Taie**, C. Park, P. Cheetham, C. H. Kim, L. Graber and S. Pamidi, “A New Representation of Paschen’s Law Suitable for Variable Temperature Power Applications,” in *2019 IEEE Electrical Insulation Conference (EIC)*. (in press).
4. **A. Al-Taie**, S. Telikapalli, P. Cheetham, C. H. Kim, S. Pamidi, “Liquid Nitrogen Cooled Superconducting Power Cable with No Solid Insulation,” in *IOP Conference Series: Materials Science and Engineering*. (under submission).
5. **A. Al-Taie**, P. Cheetham, S. Telikapalli, C. Kim, S. Pamidi, C. Park and L. Graber, “Understanding Surface Flashover in Helium Gas Cooled High Temperature Superconducting Devices,” in *IOP Conference Series: Materials Science and Engineering*. (under submission).

A.2 Publications that Resulted from Related Work

1. P. Cheetham, R. Nowell, **A. Al-Taie**, J. McAulev, C. H. Kim, L. Graber and S. Pamidi, "Exploration of Additive Manufacturing for HTS Cable Components for Electric Aircrafts," in *2018 AIAA/IEEE Electric Aircraft Technologies Symposium*, 2018. pp. 1–13.
2. C. Park, L. Graber, P. Cheetham, **A. Al-Taie**, Srikar Telikapalli, and Sastry Pamidi, "Versatile Paschen's Model for the Dielectric Strength Estimation of Binary and Ternary Gas Mixtures," *IEEE Transactions on Dielectrics and Electrical Insulation*. (in press).
3. S. Telikapalli, S. Patel, **A. Al-Taie**, P. Cheetham, C. Park, C. H. Kim, L. Graber, S. Pamidi, "Understanding the Effect of Hydrogen Concentration on the Dielectric Strength of Helium Has for Cryogenic Applications," in *IOP Conference Series: Materials Science and Engineering*. (under submission).

REFERENCES

[1] S. Kalsi, *Applications of high temperature superconductors to electric power equipment*. Wiley, 2011.

[2] C. M. Rey, *Superconductors in the Power Grid: Materials and Applications*. Elsevier, 2015.

[3] EIA, "State Electricity Profiles - Energy Information Administration." 2012.

[4] US Energy Information Administration, "Annual energy outlook 2017 with projections to 2050," *US Energy Inf. Adm.*, p. 64, 2017.

[5] B. M. Z. Jacobson and M. A. Delucchi, "A path to sustainable energy by 2030," *Sci. Am.*, no. 282, pp. 58–65, 2009.

[6] D. McCollum, V. Krey, P. Kolp, Y. Nagai, and K. Riahi, "Transport electrification: A key element for energy system transformation and climate stabilization," *Clim. Change*, vol. 123, no. 3–4, pp. 651–664, Apr. 2014.

[7] S. S. Fetisov *et al.*, "Development and characterization of a 2G HTS roebel cable for aircraft power systems," *IEEE Trans. Appl. Supercond.*, vol. 26, no. 3, pp. 3–6, 2016.

[8] J. Felder, H. Kim, and G. Brown, "Turboelectric Distributed Propulsion Engine Cycle Analysis for Hybrid-Wing-Body Aircraft," *47th AIAA Aerosp. Sci. Meet. Incl. New Horizons Forum Aerosp. Expo.*, no. January, pp. 1–25, 2009.

[9] J. G. Kim, M. A. Salmani, L. Graber, C. H. Kim, and S. V. Pamidi, "Electrical characteristics and transient analysis of HTS DC power cables for shipboard application," *2015 IEEE Electr. Sh. Technol. Symp. ESTS 2015*, vol. 1, pp. 376–381, 2015.

[10] S. S. Kalsi, N. Henderson, D. Gritter, O. Nayak, and C. Gallagher, "Benefits of HTS technology to ship systems," *2005 IEEE Electr. Sh. Technol. Symp.*, vol. 2005, pp. 437–443, 2005.

[11] "BINE Informationsdienst: News: Superconductor begins test operation." [Online]. Available: http://www.bine.info/en/newsoverview/news/supraleiter-geht-in-den-testbetrieb/. [Accessed: 18-Jun-2019].

[12] M. Stemmle, E. Marzahn, B. West, F. Schmidt, and K. Schippl, "Superconducting HVDC power cables for voltage source converter systems," in *44th International Conference on Large High Voltage Electric Systems 2012*, 2012.

[13] S. Eckroad, "EPRI Project Manager Program on Technology Innovation: a Superconducting DC Cable," 2009.

[14] and D. W. B. Fitzpatrick, T. Fikse, M. Robinson, “High Temperature Superconductor (HTS) Degaussing System Assessment,” Philadelphia, PA., 2004.

[15] J. T. Kephart, B. K. Fitzpatrick, P. Ferrara, M. Pyryt, J. Pienkos, and E. Michael Golda, “High temperature superconducting degaussing from feasibility study to fleet adoption,” *IEEE Trans. Appl. Supercond.*, vol. 21, no. 3 PART 2, pp. 2229–2232, 2011.

[16] K. Davies, P. Norman, C. Jones, S. Galloway, and M. Husband, “A review of Turboelectric Distributed Propulsion technologies for N+3 aircraft electrical systems,” *Proc. Univ. Power Eng. Conf.*, pp. 1–5, 2013.

[17] J. E. Schirber and C. A. Swenson, “Superconductivity of Mercury,” *Phys. Rev. Lett.*, vol. 2, no. 7, pp. 296–297, 1959.

[18] P. M. Grant, “Superconducting lines for the transmission of large amounts of electrical power over great distances: Garwin-Matisoo revisited forty years later,” *IEEE Trans. Appl. Supercond.*, vol. 17, no. 2, pp. 1641–1647, 2007.

[19] M. Tinkham, *Introduction to superconductivity*. Dover Publications, 2004.

[20] T. G. Berlincourt, “Type II superconductivity: Quest for understani ng,” *IEEE Trans. Magn.*, vol. 23, no. 2, pp. 403–412, 1987.

[21] S. Suzuki and K. Fukuda, *Magnesium Diboride (MgB2) Superconductor Research*. Nova Science Publishers, 2009.

[22] P. Cheetham, “Investigation of Alternative Cryogenic Dielectric Materials and Designs for High Temperature Superconducting Devices,” *ProQuest Diss. Theses*, p. 176, 2017.

[23] E. Kuffel, W. S. Zaengl, and J. Kuffel, *High Voltage Engineering Fundamentals*. Butterworth-Heinemann/Newnes, 2016.

[24] G. Lehner, *Electromagnetic field theory for engineers and physicists*. Springer, 2008.

[25] J. D. Kraus and K. R. Carver, *Electromagnetics*. McGraw-Hill, 1984.

[26] W. H. (William H. Hayt and J. A. Buck, *Engineering electromagnetics*. McGraw-Hill, 2012.

[27] A. Küchler, *High Voltage Engineering*. Berlin, Heidelberg: Springer Berlin Heidelberg, 2018.

[28] M. S. Naidu and V. Kamaraju, *High voltage engineering*. McGraw-Hill, 1996.

[29] W. A. Thue, *Electrical power cable engineering*. CRC Press, 2012.

[30] S. Kasap, *Principles of electronic materials and devices*. McGraw-Hill, 2006.

[31] J. Wada, G. Ueta, S. Okabe, and M. Hikita, “Dielectric properties of gas mixtures with

per-fluorocarbon gas and gas with low liquefaction temperature," *IEEE Trans. Dielectr. Electr. Insul.*, vol. 23, no. 2, pp. 838–847, 2016.

[32] H. K. Kim and F. G. Shi, "Thickness dependent dielectric strength of a low-permittivity dielectric film," *IEEE Trans. Dielectr. Electr. Insul.*, vol. 8, no. 2, pp. 248–252, Apr. 2001.

[33] C. Neusel and G. A. Schneider, "Dependence of the breakdown strength on thickness and permittivity," in *Proceedings of IEEE International Conference on Solid Dielectrics, ICSD*, 2013, pp. 31–35.

[34] F. Ombello, P. Caracino, M. Nassi, and C. Montanari, "Insulating Materials Evaluation for Cold Dielectric," no. February, pp. 958–963, 2002.

[35] M. Kosaki, "Research and development of electrical insulation of superconducting cables by extruded polymers," *IEEE Electr. Insul. Mag.*, vol. 12, no. 5, pp. 17–24, 1996.

[36] L. H. Truong and P. L. Lewin, "Degradation behaviour of solid insulation under cryogenic conditions," *Proc. IEEE Int. Conf. Solid Dielectr. ICSD*, pp. 640–643, 2013.

[37] M. Kosaki, M. Nagao, Y. Mizuno, N. Shimizu, and K. Horii, "Development of extruded polymer insulated superconducting cable," *Cryogenics (Guildf).*, vol. 32, no. 10, pp. 885–894, Jan. 1992.

[38] P. G. Cheetham, W. Kim, C. H. Kim, S. V. Pamidi, L. Graber, and H. Rodrigo, "Use of partial discharge inception voltage measurements to design a gaseous helium cooled high temperature superconducting power cable," *IEEE Trans. Dielectr. Electr. Insul.*, vol. 24, no. 1, pp. 191–199, 2017.

[39] M. Hazeyama, T. Kobayashi, N. Hayakawa, S. Honjo, T. Masuda, and H. Okubo, "Partial discharge inception characteristics under butt gap condition in liquid nitrogen/PPLP® composite insulation system for high temperature superconducting cable," *IEEE Trans. Dielectr. Electr. Insul.*, vol. 9, no. 6, pp. 939–944, Dec. 2002.

[40] P. Cheetham, W. Kim, C. H. Kim, L. Graber, H. Rodrigo, and S. Pamidi, "Enhancement of Dielectric Strength of Cryogenic Gaseous Helium by Addition of Small Mol% Hydrogen," *IEEE Trans. Appl. Supercond.*, vol. 27, no. 4, 2017.

[41] P. Cheetham, J. Viquez, L. Graber, C. H. Kim, H. Rodrigo, and S. Pamidi, "Novel design concept and demonstration of a superconducting gas-insulated transmission line," *IEEE Trans. Appl. Supercond.*, vol. 27, no. 4, pp. 1–5, 2017.

[42] H. Koch, *Gas-insulated transmission lines (GIL)*. Chichester, UK: John Wiley & Sons, Ltd, 2011.

[43] H. Rodrigo, Dongsoon Kwag, L. Graber, B. Trociewitz, and S. Pamidi, "AC Flashover Voltages Along Epoxy Surfaces in Gaseous Helium Compared to Liquid Nitrogen and Transformer Oil," *IEEE Trans. Appl. Supercond.*, vol. 24, no. 3, pp. 1–6, Jun. 2014.

[44] W.-J. Shin, J.-S. Hwang, J.-K. Seong, J.-G. Lee, and B.-W. Lee, “Breakdown characteristics of liquid nitrogen for transmission-class superconducting electric equipment,” in *2012 IEEE International Conference on Condition Monitoring and Diagnosis*, 2012, pp. 766–769.

[45] I. Sauers, R. James, A. Ellis, E. Tuncer, G. Polizos, and M. Pace, “Effect of Bubbles on Liquid Nitrogen Breakdown in Plane-Plane Electrode Geometry From 100–250 kPa,” *IEEE Trans. Appl. Supercond.*, vol. 21, no. 3, pp. 1892–1895, Jun. 2011.

[46] H.-M. Chang, Y. S. Choi, S. W. Van Sciver, and K. D. Choi, “Cryogenic cooling system of HTS transformers by natural convection of subcooled liquid nitrogen,” *Cryogenics (Guildf).*, vol. 43, no. 10–11, pp. 589–596, Oct. 2003.

[47] A. Kalair, N. Abas, and N. Khan, “Comparative study of HVAC and HVDC transmission systems,” *Renew. Sustain. Energy Rev.*, vol. 59, pp. 1653–1675, 2016.

[48] W. Sae-Kok, A. Yokoyama, S. C. Verma, and S. Ogawa, “Excitation control system design of rotary type frequency converter for performance improvement of power system dynamics,” *IEEE Trans. Energy Convers.*, vol. 21, no. 1, pp. 210–220, 2006.

[49] D. Tiku, “DC Power Transmission: Mercury-Arc to Thyristor HVdc Valves [History],” *IEEE Power Energy Mag.*, vol. 12, no. 2, pp. 76–96, Mar. 2014.

[50] J. C. Whitaker, *AC power systems handbook*. CRC/Taylor & Francis, 2007.

[51] M. H. Okba, M. H. Saied, M. Z. Mostafa, and T. M. Abdel- Moneim, “High voltage direct current transmission - A review, part I,” in *2012 IEEE Energytech*, 2012, pp. 1–7.

[52] P. (Prabha) Kundur, N. J. Balu, and M. G. Lauby, *Power system stability and control*. McGraw-Hill, 1994.

[53] “Best Paths - Home.” [Online]. Available: http://www.bestpaths-project.eu/. [Accessed: 07-Dec-2018].

[54] “Best Paths - Demonstration - DEMO 5.” [Online]. Available: http://www.bestpaths-project.eu/en/demonstration/demo-5. [Accessed: 07-Dec-2018].

[55] P. Chowdhuri and H. L. Laquer, “Some Electrical Characteristics of a DC Superconducting Cable,” *IEEE Trans. Power Appar. Syst.*, vol. PAS-97, no. 2, pp. 399–408, Mar. 1978.

[56] Jae-Ho Kim and S. Pamidi, “Electrical Characteristics of 2G HTS Tapes Under DC Current With AC Ripple,” *IEEE Trans. Appl. Supercond.*, vol. 22, no. 3, pp. 5801104–5801104, Jun. 2012.

[57] Y. Ivanov *et al.*, “Current imbalance and AC losses of long distance DC HTS cable,” in *2015 IEEE International Conference on Applied Superconductivity and Electromagnetic Devices (ASEMD)*, 2015, pp. 578–579.

[58] J.-G. Kim, S.-K. Kim, M. Park, and I.-K. Yu, “Hardware-in-the-Loop Simulation for Superconducting DC Power Transmission System,” *IEEE Trans. Appl. Supercond.*, vol. 25, no. 3, pp. 1–4, Jun. 2015.

[59] Y. Wang *et al.*, “A Novel Approach for Design of DC HTS Cable,” *IEEE Trans. Appl. Supercond.*, vol. 21, no. 3, pp. 1042–1045, Jun. 2011.

[60] J. Qin and M. Saeedifard, “DC-line current ripple reduction of a parallel hybrid modular multilevel HVDC converter,” in *2014 IEEE PES General Meeting | Conference & Exposition*, 2014, pp. 1–5.

[61] R. L. Garwin and J. Matisoo, “Superconducting Lines for the Transmission of Large Amounts of Electrical Power over Great Distances,” *Proc. IEEE*, vol. 55, no. 4, pp. 538–548, 1967.

[62] “Testing of superconducting cable systems,” Paris, France, 2013.

[63] Shaotao Dai *et al.*, “Testing and Demonstration of a 10-kA HTS DC Power Cable,” *IEEE Trans. Appl. Supercond.*, vol. 24, no. 2, pp. 99–102, Apr. 2014.

[64] Dong Zhang *et al.*, “Testing Results for the Cable Core of a 360 m/10 kA HTS DC Power Cable Used in the Electrolytic Aluminum Industry,” *IEEE Trans. Appl. Supercond.*, vol. 23, no. 3, pp. 5400504–5400504, Jun. 2013.

[65] M. Hamabe, H. Watanabe, Jian Sun, N. Yamamoto, T. Kawahara, and S. Yamaguchi, “Status of a 200-Meter DC Superconducting Power Transmission Cable After Cooling Cycles,” *IEEE Trans. Appl. Supercond.*, vol. 23, no. 3, pp. 5400204–5400204, Jun. 2013.

[66] H. Yumura *et al.*, “Update of YOKOHAMA HTS Cable Project,” *IEEE Trans. Appl. Supercond.*, vol. 23, no. 3, pp. 5402306–5402306, Jun. 2013.

[67] J. H. Lim *et al.*, “Cryogenic System for 80-kV DC HTS Cable in the KEPCO Power Grid,” *IEEE Trans. Appl. Supercond.*, vol. 25, no. 3, pp. 1–4, Jun. 2015.

[68] B. Yang, J. Kang, S. Lee, C. Choi, and Y. Moon, “Qualification Test of a 80 kV 500 MW HTS DC Cable for Applying into Real Grid,” *IEEE Trans. Appl. Supercond.*, vol. 25, no. 3, 2015.

[69] “TNSC develops cooling neon-based turbo refrigerator | News | gasworld.” [Online]. Available: https://www.gasworld.com/tnsc-develops-cooling-neon-based-turbo-refrigerator/2010784.article. [Accessed: 07-Dec-2018].

[70] “Turbo-Brayton cryogenic systems | Air Liquide Advanced Technologies.” [Online]. Available: https://advancedtech.airliquide.com/turbo-brayton-cryogenic-systems. [Accessed: 07-Dec-2018].

[71] “Gifford-McMahon Cryorefrigerators - Cryomech.” [Online]. Available: http://www.cryomech.com/cryorefrigerators/gifford/. [Accessed: 07-Dec-2018].

[72] H. Hirai *et al.*, “Neon turbo-Brayton cycle refrigerator for HTS power machines,” in *AIP Conference Proceedings*, 2012, vol. 1434, no. 1, pp. 1672–1679.

[73] H. Hirai, M. Hirokawa, S. Yoshida, T. Sano, and S. Ozaki, “Development of a turbine-compressor for 10 kW class neon turbo-Brayton refrigerator,” in *AIP Conference Proceedings*, 2014, vol. 1573, no. 1, pp. 1236–1241.

[74] J. Lee *et al.*, “Investigation on Cryogenic Refrigerator and Cooling Schemes for Long Distance HTS Cable,” *IEEE Trans. Appl. Supercond.*, vol. 25, no. 3, pp. 1–4, Jun. 2015.

[75] J. A. Demko and W. V. Hassenzahl, “Thermal Management of Long-Length HTS Cable Systems,” *IEEE Trans. Appl. Supercond.*, vol. 21, no. 3, pp. 957–960, Jun. 2011.

[76] M. M. Rahman, M. F. Rabbi, M. K. Islam, and F. M. M. Rahman, “HVDC over HVAC power transmission system: Fault current analysis and effect comparison,” *1st Int. Conf. Electr. Eng. Inf. Commun. Technol. ICEEICT 2014*, 2014.

[77] M. Karthikeyan, Y. M. Yeap, and A. Ukil, “Simulation and analysis of faults in high voltage DC (HVDC) power transmission,” in *IECON 2014 - 40th Annual Conference of the IEEE Industrial Electronics Society*, 2014, pp. 1786–1791.

[78] B. Hafner, J. , Jacobson, “Proactive hybrid HVDC breakers - A key innovation for reliable HVDC grids,” *Proc. CIGRE Bol. Symp.*, pp. 1–8, 2011.

[79] E. N. Abildgaard and M. Molinas, “Modelling and control of the modular multilevel converter (MMC),” *Energy Procedia*, vol. 20, no. Mmc, pp. 227–236, 2012.

[80] H. Knaak, “Modular multilevel converters and HVDC/FACTS: A success story,” in *proceedings of the 2011-14th European Conference on Power Electronics and Applications.*, 2011.

[81] A. Lesnicar and R. Marquardt, “An innovative modular multilevel converter topology suitable for a wide power range,” in *2003 IEEE Bologna Power Tech Conference Proceedings,* vol. 3, pp. 272–277.

[82] A. Morandi, “HTS dc transmission and distribution: Concepts, applications and benefits,” IOP Publishing, 2015.

[83] W. J. Kim *et al.*, “Comparative Study of Cryogenic Dielectric and Mechanical Properties of Insulation Materials for Helium Gas Cooled HTS Power Devices,” *IEEE Trans. Appl. Supercond.*, vol. 27, no. 4, 2017.

[84] O. Chevtchenko *et al.*, “Low friction cryostat for HTS power cable of Dutch project,” *Phys. Procedia*, vol. 36, pp. 1309–1312, 2012.

[85] W. Hassenzahl, “Novel Approaches and Alternative Cryogens for Cooling a Superconducting Cable,” Palo Alto, 2012.

[86] J. Millan and P. Godignon, “Wide Band Gap power semiconductor devices,” *Proc. 2013 Spanish Conf. Electron Devices, CDE 2013*, pp. 293–296, 2013.

[87] S. Pamidi, C. H. Kim, and L. Graber, “High-temperature superconducting (HTS) power cables cooled by helium gas,” in *Superconductors in the Power Grid: Materials and Applications*, 2015, pp. 225–260.

[88] N. Hayakawa, “Introduction of CIGRE WG D1.64 and topics on insulation issues on superconducting cables and fault current limiters,” *Proc. IEEE Int. Conf. Prop. Appl. Dielectr. Mater.*, vol. 2018-May, no. September 2017, pp. 156–159, 2018.

[89] T. Wang, H. Ueda, K. Agatsuma, and A. Ishiyama, “Evaluation of positional stability in active magnetic levitation using spherical HTS bulk for inertial nuclear fusion,” *IEEE Trans. Appl. Supercond.*, vol. 21, no. 3 PART 2, pp. 1579–1583, 2011.

[90] B. K. Fitzpatrick, J. T. Kephartl, and E. Michael Golda, “Characterization of gaseous helium flow cryogen in a flexible cryostat for naval applications of high temperature superconductors,” *IEEE Trans. Appl. Supercond.*, vol. 17, no. 2, pp. 1752–1755, 2007.

[91] S. Satyanarayana, S. Indrakanti, J. Kim, C. Kim, and S. Pamidi, “Coupled Cryogenic Thermal and Electrical Models for Transient Analysis of Superconducting Power Devices with Integrated Cryogenic Systems,” *IOP Conf. Ser. Mater. Sci. Eng.*, vol. 278, no. 1, 2017.

[92] C. Park, S. Pamidi, and L. Graber, “The critical electric field of gas mixtures over the extended range of cryogenic operating conditions,” *J. Appl. Phys.*, vol. 122, no. 15, p. 153301, Oct. 2017.

[93] C. Park, J. Wei, P. Cheetham, C. H. Kim, S. Pamidi, and L. Graber, “The influence of temperature on the dielectric strength of gaseous cryogens,” *Proc. IEEE Int. Conf. Prop. Appl. Dielectr. Mater.*, vol. 2018-May, pp. 164–167, 2018.

[94] A. E. D. Heylen, “Sparking formulae for very high-voltage Paschen characteristics of gases,” *IEEE Electr. Insul. Mag.*, vol. 22, no. 3, pp. 25–33, 2006.

[95] Y. P. Raĭzer, “Gas discharge physics,” p. 449, 1997.

[96] N. Hill and M. Kurrat, “Breakdown field strength of gaseous nitrogen at 3 bar under AC stress,” *2018 12th Int. Conf. Prop. Appl. Dielectr. Mater.*, pp. 164–167, 2018.

[97] M. A. Green, “Cooling and cooling-down MgB2 and HTS magnets using a hydrogen thermal siphon loop and coolers operating from 15 K to 28 K,” *IEEE Trans. Appl. Supercond.*, vol. 24, no. 3, pp. 2–5, 2014.

[98] M. Miki *et al.*, “Influence of AC magnetic field on a rotating machine with Gd-bulk HTS field-pole magnets,” *IEEE Trans. Appl. Supercond.*, vol. 21, no. 3 PART 2, pp. 1185–1189, 2011.

[99] R. Sato, B. Felder, M. Miki, K. Tsuzuki, H. Hayakawa, and M. Izumi, “Helium-neon gas mixture thermosyphon cooling and stability for large scale HTS synchronous motors,” *IEEE Trans. Appl. Supercond.*, vol. 23, no. 3, p. 5200704, 2013.

[100] C. Park, L. Graber, and S. Pamidi, “The dielectric properties of gaseous cryogen mixtures of He, H2, Ne, and N2 in a temperature range of 50–80 K at pressures up to 2.0 MPa,” *J. Appl. Phys.*, vol. 121, no. 8, p. 083304, Feb. 2017.

[101] C. Park, S. Pamidi, and L. Graber, “Boltzmann Analysis of Cryogenic He–H2 Gas Mixtures as Dielectric Media for High-Temperature Superconducting Power Devices,” *IEEE Trans. Appl. Supercond.*, vol. 27, no. 4, pp. 1–6, Jun. 2017.

[102] C. Park, L. Graber, P. Cheetham, J. G. Viquez, C. H. Kim, and S. Pamidi, “A versatile modeling technique for predicting dielectric strength improvements in gas mixtures for superconducting applications,” *IEEE Trans. Dielectr. Electr. Insul.*, vol. 24, no. 5, pp. 2755–2764, 2017.

[103] M. Hara, J. Suehiro, H. Matsumoto, and T. Kaneko, “Breakdown Characteristics of Cryogenic Gaseous Nitrogen and Estimation of its Electrical Insulation Properties,” *IEEE Trans. Electr. Insul.*, vol. 24, no. 4, pp. 609–617, 1989.

[104] H. Toyota, S. Zama, Y. Akamine, S. Matsuoka, and K. Hidaka, “Gaseous electrical discharge characteristics in air and nitrogen at cryogenic temperature,” *IEEE Trans. Dielectr. Electr. Insul.*, vol. 9, no. 6, pp. 891–898, 2002.

[105] H. Goshima, T. Suzuki, and N. Hayakawa, “Dielectric breakdown characteristics of cryogenic nitrogen gas above liquid nitrogen,” *IEEE Trans. Dielectr. Electr. Insul.*, vol. 1, no. 3, pp. 538–543, 1994.

[106] L. Graber, W. J. Kim, P. Cheetham, C. H. Kim, H. Rodrigo, and S. V. Pamidi, “Dielectric properties of cryogenic gas mixtures containing helium, neon, and hydrogen,” in *IOP Conference Series: Materials Science and Engineering*, 2015, vol. 102, no. 1.

[107] P. Cheetham, J. Wagner, T. Stamm, C. H. Kim, L. Graber, and S. Pamidi, “Electric field analysis of insulating spacers for a superconducting gas-insulated transmission line,” *Proc. IEEE Int. Conf. Prop. Appl. Dielectr. Mater.*, vol. 2018-May, pp. 185–189, 2018.

[108] P. Cheetham, C. H. Kim, L. Graber, and S. Pamidi, “Practical considerations for the design of a superconducting gas-insulated transmission line for shipboard applications,” in *2017 IEEE Electric Ship Technologies Symposium, ESTS 2017*, 2017, pp. 292–298.

[109] P. Cheetham *et al.*, “Exploration of Additive Manufacturing for HTS Cable Components for Electric Aircrafts,” in *2018 AIAA/IEEE Electric Aircraft Technologies Symposium*, 2018, pp. 1–13.

[110] J. F. Maguire *et al.*, “Operational experience of the world’s first transmission level voltage HTS power cable,” in *AIP Conference Proceedings*, 2010, vol. 1218, pp. 437–444.

[111] V. E. Sytnikov *et al.*, “Status of HTS Cable Link Project for St. Petersburg Grid,” *IEEE Trans. Appl. Supercond.*, vol. 25, no. 3, pp. 1–4, Jun. 2015.

[112] Energy.gov, 2019. [Online]. Available: https://www.energy.gov/sites/prod/files/oeprod/DocumentsandMedia/columbus_03.05.08.pdf. [Accessed: 21- Jul- 2019].

[113] S. Kopylov *et al.*, “HTS DC transmission line for megalopolis grid development,” *J. Phys. Conf. Ser.*, vol. 507, no. PART 3, pp. 1–5, 2014.

[114] A. Al-Taie, L. Graber, and S. V. Pamidi, “Technical Challenges and Potential Solutions for Cross-Country Multi-Terminal Superconducting DC Power Cables,” in *IOP Conference Series: Materials Science and Engineering*, 2017, vol. 279, no. 1.

[115] M. Jefferies and K. Mathes, “Dielectric Loss and Voltage Breakdown in Liquid Nitrogen and Hydrogen,” *IEEE Trans. Electr. Insul.*, vol. EI-5, no. 3, pp. 83–91, Sep. 1970.

[116] P. Cheetham, C. Park, C. H. Kim, L. Graber, and S. V. Pamidi, “Dielectric properties of cryogenic gas mixtures for superconducting power applications,” *IOP Conf. Ser. Mater. Sci. Eng.*, vol. 278, no. 1, 2017.

[117] H. C. Miller, “Surface Flashover of Insulators,” *IEEE Trans. Electr. Insul.*, vol. 24, no. 5, pp. 765–786, 1989.

[118] R. Hawley, “Solid insulators in vacuum: A review (Invited paper),” *Vacuum*, vol. 18, no. 7, pp. 383–390, Jul. 1968.

[119] J. D. Cross, “The mechanism of flashover across solid insulators in vacuum,” in *VII Int. Symp. Disch. Elect. Insul. Vac*, 1976, pp. 24–37.

[120] R. V. Latham, *High voltage vacuum insulation : basic concepts and technological practice*. Academic Press, 1995.

[121] H. Rodrigo, W. Baumgartinger, G. H. Heller, D. G. Crook, and S. L. Ranner, “Surface flashover of cylindrical G10 under ac and dc voltages at room and cryogenic temperatures,” *IEEE Trans. Appl. Supercond.*, vol. 21, no. 3 PART 2, pp. 1409–1412, 2011.

[122] A. K. Vijh, “Electric Strength and Molecular Properties of Gaseous Dielectrics,” *IEEE Trans. Electr. Insul.*, vol. EI-12, no. 4, pp. 313–315, Aug. 1977.

[123] A. K. Vijh, “Intermolecular bonding and the electric strengths of dielectric gases,” *J. Mater. Sci.*, vol. 11, no. 7, pp. 1374–1375, 1976.

BIOGRAPHICAL SKETCH

Aws Al-Taie received his B.Sc in electrical engineering (ranked first) and M.Sc in power engineering degrees from University of Technology-Iraq (UoT) in 2005 and 2008, respectively. He is a faculty member in UoT, and he was awarded a fully funded Ph.D scholarship from the Iraqi Ministry of Higher Education and Scientific Research. He is currently pursuing his Ph.D study at Florida State University (FSU) and conducting research in the Center for Advanced Power Systems (CAPS). His research involves high voltage and electrical insulation studies for gas cooled high temperature superconducting power devices.